UNIVERSITÀ DI PARMA

Università degli Studi di Parma

Dottorato di ricerca in Fisica

XXXI ciclo

Semi-analytic methods for the Large- Scale Structure of the Universe: improved Time Renormalization Group and the BAO Extractor operator

---

Author:
Eugenio Noda

Supervisor:
Massimo Pietroni

Chair of Doctorate Board:
Cristiano Viappiani

Anni 2015/2018

Acknowledgements

I would like to thank my supervisor Massimo Pietroni for the guidance and support he has given me throughout my PhD years. His ability to always pinpoint the critical concepts behind the physical problem at hand and the ability to transmit them with clarity have been a source of great inspiration to me. His pragmatic attitude and his hard work, together with a measure of good humour, have made our association valuable to me.

I would also like to thank Marco Peloso for the work we have done together and the useful discussions. His attention to the details has saved me more than once. Likewise, I thank Takahiro Nishimichi for sharing his expertise with me and for guiding me during my stay in Tokyo.

I am indebted to INFN and the University of Parma for the opportunity to carry out my PhD and to attend the many workshops and conferences to which I took part.

Finally, I thank my parents for their undying faith in me and Marta for her unfailing support.

Contents

Chapter 1

Introduction

The last decades have seen the rise of Cosmology as a precision science. European Space Agency (ESA)'s Planck satellite, which finished taking data in 2013, has mapped the angular temperature anisotropies and polarization of Cosmic Microwave Background (CMB) with high accuracy, providing a precise snapshot of the Universe at the epoch of recombination, which in turn translated in a sub-percent accuracy on the determination of most of the ΛCDM cosmological parameters [1]. In the meantime, galaxy surveys like the Sloan Digital Sky Survey (SDSS) have created a catalogue of the late universe by measuring the clustering of millions of galaxies in our nearby universe, with future surveys planning to measure ever wider and deeper portions of the sky. ESA's Euclid space telescope, which will be launched around 2021, is going to expand this catalogue by probing a more remote past, reaching higher redshifts ($z > 2$ using galaxies and even $z > 8$ with quasars) with the goal of constraining the expansion history of the Universe [2].

So far all the data we have collected is in good agreement with a 6-parameter model, namely a flat ΛCDM model, in which the current content of the Universe is constituted by 68% of Dark Energy (DE) in the form of a cosmological constant Λ, by 26% of a pressure-less Cold Dark Matter component and with regular matter (referred to as "baryonic" matter in Cosmology) only contributing with 5% (see for example Planck's results, Ref. [3]).

The fact that both early and late Universe data can be fit with 6 parameters is remarkable. However many questions remain unanswered. Despite the strong evidence for DM and the determination of its abundance, its nature still eludes us. A plethora of candidates have been proposed but, as to

date, none of them has been validated by experiments [4]. Our knowledge of Dark Energy is even more feeble. The existence of Dark Energy, or some modification to General Relativity (Modified Gravity), is required to explain the accelerated expansion of the Universe at the present epoch. Even though a cosmological constant Λ fits the data well, it turns out to be difficult to encase it in our current understanding of physics at microscopic scales, namely Quantum Field Theory. For instance, without assuming an unnatural fine-tuning, an estimate of the cosmological constant in the Standard Model of Particle Physics gives a value that is about 120 orders of magnitude bigger than the one we measure.

A way to classify the various DE models is via the equation of state parameter $w = p_{DE}/\rho_{DE}$, that gives the (possibly) time-dependent relation between the DE pressure p_{DE} and energy density ρ_{DE}. w determines the evolution of the DE density in time, through $\rho \propto a^{-3(w+1)}$, where a is the scale factor.

$w = -1$ corresponds to the cosmological constant and a great effort is being made to find experimental evidence of a deviation from that value, by measuring the expansion history of the Universe. A common parameterisation of the equation of state is given by the linear relation [5, 6] :

$$w(a) = w_0 + w_a(1 - a). \tag{1.1}$$

This parameterisation does not encapsulate all the possible DE models, hence in some cases it could be better to consider the DE density $\rho(a)$, which also has the advantage to be more directly related to observable quantities. A more recent approach to the classification of the many DE models is that of the Effective Field Theory of Dark Energy [7, 8, 9, 10], where one writes down the most general action consistent with the symmetries of the system. Depending on the coefficients of each term, one retrieves the low energy limit of most of the DE models that have been proposed.

In order to make this measurement we need reference objects that would enable us to determine distances in the Universe. These reference objects may be *standard candles*, that is, luminous objects for which we know the absolute magnitude, or *standard rulers*, observables for which the absolute transverse (with respect to the line of sight) dimension is known. One example of standard candles is Type-Ia supernovae, which were the probes that were used when the accelerated expansion was first discovered [11, 12, 13, 14, 15]. A standard ruler, which will be one of the main focuses of this work, can

be found in the clustering of galaxies at large scales: the *Baryon Acoustic Oscillations* (BAO) [16, 17, 18, 19].

The clustering of galaxies presents a peak in its 2-point correlation function at a comoving position of ~ 110 Mpc/h, which corresponds to the sound horizon at recombination (in fact, an analogous peak is found in the correlation function of the CMB temperature anisotropies). This peak translates to an oscillatory feature in the Fourier Transform of the correlation function. At first approximation, the comoving position of the BAO remains the same throughout the evolution of the Universe, making them an important tool to constrain the expansion history of the Universe. However, in order to fully exploit their potential as standard rulers it is important that the corrections induced by nonlinear dynamics and systematic effects are properly taken into account.

Current data combining CMB data and galaxy clustering give a constraint on the equation of state parameter of DE of $w = -1.01 \pm 0.06$, fully compatible with ΛCDM [20]. Future surveys plan to reduce the error on this quantity, with the goal of reaching the percent level of accuracy. It is therefore crucial that our theoretical prediction be as accurate as the forthcoming experimental data.

Although the evolution equations for the space-time dependent density of the Universe are known, their solution proves to be an nontrivial task. Two main complementary approaches are employed, which are numerical N-Body simulations and analytical methods, which include perturbation theory and its extensions, which are necessary to describe the physical effects not captured by perturbative means. N-Body simulations have the advantage of solving the full equations of motion and therefore they capture well the nonlinear dynamics at small scales. However they are rather time consuming, which makes it difficult for these methods to explore parameter spaces or alternative cosmological models. Analytical methods, on the other hand have a greater flexibility in exploring different models, provide insights on the underlying physics and also have typically very reduced computational times. Their drawback is that the range of scales to which they are applicable is strongly limited by non-perturbative corrections that become important at small scales and recent times.

In this work we are going to concentrate on a semi-analytic approach and present a proposal to improve the perturbative paradigm to create an accurate prediction for the clustering of galaxies, with a particular stress on determining the BAO scale.

This thesis is structured as follows: in Chapter 2 we are going to review Standard Perturbation Theory, describe its limitations and summarise two methods to improve it, namely by introducing corrections for the contributions coming from the IR and UV sectors. In Chapter 3 we are going to implement these corrections on an technique called Time Renormalization Group and introduce a new way to extract the oscillating part of a Power Spectrum, the Extractor operator. In Chapter 4 we will test the performance of the extractor operator against N-Body simulations and, in particular, its robustness in the presence of Redshift Space Distortions and halo bias. In Chapter 5 we will apply the Extractor operator to a set of galaxy survey experimental data, the BOSS DR12 dataset, and compare the performance of our procedure for determining the BAO to the standard analysis carried out by the BOSS collaboration. Finally we will summarise our results in Chapter 6.

Chapter 2

Perturbation Theory and its challenges

2.1 Standard Perturbation Theory

The starting point is the collisionless Boltzmann equation, or Vlasov equation, governing the evolution of the phase space density of dark matter $f(\mathbf{x}, \mathbf{p}, \tau)$:

$$\left(\frac{\partial}{\partial\tau} + \frac{p^i}{am}\frac{\partial}{\partial x^i} - am\nabla_x^i\phi(\mathbf{x},\tau)\frac{\partial}{\partial p^i}\right) f(\mathbf{x},\mathbf{p},\tau) = 0, \tag{2.1}$$

which is accompanied by the Poisson equation for the gravitational potential ϕ,

$$\nabla^2\phi(\mathbf{x},\tau) = \frac{3}{2}\mathcal{H}(\tau)^2\Omega_m(\tau)\delta(\mathbf{x},\tau), \tag{2.2}$$

where the density perturbation $\delta(\mathbf{x},\tau)$ is given by

$$\delta(\mathbf{x},\tau) = \frac{n(\mathbf{k},\tau)}{\bar{n}} - 1. \tag{2.3}$$

$n(\mathbf{x},\tau)$ is the number density, which we will define shortly and $\mathcal{H}$ is the conformal Hubble rate. In writing Eq. 2.1 we have assumed GR in the sub-horizon limit.

This equation is in general very difficult to solve even numerically, so an approximation prescription must be made in order to use it.

Let us consider the first three moments of the distribution function f:

$$
\begin{aligned}
n(\mathbf{x},\tau) &= \int d^3p f(\mathbf{x},\mathbf{p},\tau),\\
v^i(\mathbf{x},\tau) &= \frac{1}{n(\mathbf{x},\tau)}\int d^3p \frac{p^i}{am} f(\mathbf{x},\mathbf{p},\tau),\\
\sigma^{ij}(\mathbf{x},\tau) &= \frac{1}{n(\mathbf{x},\tau)}\int d^3p \frac{p^i}{am}\frac{p^j}{am} f(\mathbf{x},\mathbf{p},\tau) - v^i(\mathbf{x},\tau)v^j(\mathbf{x},\tau).
\end{aligned}
\tag{2.4}
$$

These first moments are the matter density, velocity and velocity dispersion fields respectively. Taking moments of the Vlasov equation we obtain an infinite hierarchy of coupled equations:

$$
\begin{aligned}
&\frac{\partial\delta(\mathbf{x},\tau)}{\partial\tau} + \frac{\partial}{\partial x^i}\left(1+\delta(\mathbf{x},\tau)\right)v^i(\mathbf{x},\tau) = 0,\\
&\frac{\partial v^i(\mathbf{x},\tau)}{\partial\tau} + \mathcal{H}(\tau)v^i(\mathbf{x},\tau) + v^k(\mathbf{x},\tau)\frac{\partial}{\partial x^k}v^i(\mathbf{x},\tau) =\\
&\qquad -\frac{\partial}{\partial x^i}\phi(\mathbf{x},\tau) - \frac{1}{n(\mathbf{x},\tau)}\frac{\partial}{\partial x^j}\left(n(\mathbf{x},\tau)\sigma^{ij}(\mathbf{x},\tau)\right),\\
&\qquad \dots
\end{aligned}
\tag{2.5}
$$

Each of these equation constitutes an equation of motion for the n-th moment, which depends on the $n+1$-th moment. A prescription must be made to truncate the hierarchy of equations. For instance, the equations of motion for the overdensity $\delta(\mathbf{x},\tau)$ and velocity fields $\mathbf{v}(\mathbf{x},\tau)$ become a closed set once we give an ansatz for the velocity dispersion $\sigma^{ij}(\mathbf{x},\tau)$. The simplest assumption is to set $\sigma^{ij}(\mathbf{x},\tau)\equiv 0$ which goes by the name of *single-stream approximation* (SSA). Since the velocity dispersion quantifies the spread of the velocities of the particles at position $\mathbf{x}$ around the mean velocity $\mathbf{v}(\mathbf{x},\tau)$, setting it to 0 means that the fluid is characterised by one single flow (or "stream") and that at every position there is only one value for the particle velocity which is equal to $\mathbf{v}$. This approximation is known to work at high redshift and large scales, while it breaks down after the particle trajectories cross each other ("shell crossing") and velocities start to virialize. In Section 2.3 we discuss some approaches to go beyond the SSA and add the effect of multi-streaming to the picture.

2.1.1 Single-stream approximation in the Eulerian framework

Even neglecting the contribution of the velocity dispersion, Eqs. 2.5 cannot be solved exactly (except for particular cases) so we look for a perturbative solution. If we want to go beyond linear approximation the first step is to write the equations in Fourier Space:

$$\frac{\partial\delta(\mathbf{k},\tau)}{\partial\tau} + \theta(\mathbf{k},\tau) = \\ -\int d^3\mathbf{k}_1\; d^3\mathbf{k}_2\; \delta_D(\mathbf{k}-\mathbf{k}_1-\mathbf{k}_2)\alpha(\mathbf{k}_1,\mathbf{k}_2)\theta(\mathbf{k}_1,\tau)\delta(\mathbf{k}_2,\tau), \tag{2.6}$$

$$\frac{\partial\theta(\mathbf{k},\tau)}{\partial\tau} + \mathcal{H}(\tau)\theta(\mathbf{k},\tau) + \frac{3}{2}\Omega_m\mathcal{H}^2(\tau)\delta(\mathbf{k},\tau) = \\ -\int d^3\mathbf{k}_1\; d^3\mathbf{k}_2\delta_D(\mathbf{k}-\mathbf{k}_1-\mathbf{k}_2)\beta(\mathbf{k}_1,\mathbf{k}_2)\theta(\mathbf{k}_1,\tau)\theta(\mathbf{k}_2,\tau). \tag{2.7}$$

In this equation $\theta(\mathbf{k},\tau) = i\mathbf{k}\cdot\mathbf{v}(\mathbf{k},\tau)$ is the divergence of the velocity field. The velocity field in general has both a divergence and a vorticity component:

$$v^i(\mathbf{k}) = -i\frac{k^i}{k^2}\theta(\mathbf{k}) + i\epsilon_{ijk}\frac{k^j}{k^2}v_*(\mathbf{k}), \tag{2.8}$$

however, since the vorticity component of the velocity is sourced by the velocity dispersion σ^{ij}, as long as the latter is zero the former can be neglected (given that the initial vorticity is small). This reduces the number of degrees of freedom for which we need to solve to just 2. This approximation also breaks down after shell crossing. The Poisson equation, Eq.2.2, has been used to substitute $\nabla\phi$ in the velocity equation and we defined two functions α and β:

$$\alpha(\mathbf{k}_1,\mathbf{k}_2) \equiv \frac{\mathbf{k}_1\cdot(\mathbf{k}_1+\mathbf{k}_2)}{k_1^2}, \quad \beta(\mathbf{k}_1,\mathbf{k}_2) \equiv \frac{(\mathbf{k}_1+\mathbf{k}_2)^2(\mathbf{k}_1\cdot\mathbf{k}_2)}{2k_1^2k_2^2}. \tag{2.9}$$

These two functions encode the non-linearity of the equations. We retrieve the linear solutions by setting the R.H.S of Eqs. 2.6 to zero. In this case we can combine the two equations in a single equation for δ:

$$\ddot{\delta}(\mathbf{x},\tau) + \mathcal{H}\dot{\delta} - \frac{3}{2}\Omega_m\mathcal{H}^2(\tau)\delta(\mathbf{x},\tau). \tag{2.10}$$

This equation admits a solution of the form:

$$\delta(\mathbf{x},\tau) = D(\tau)\delta(\mathbf{x},0). \tag{2.11}$$

$D(\tau)$ is called *linear growth factor. In this solution the density fluctuations change their amplitude in time, but not their spatial distribution. In an Einstein-De Sitter Universe, in which* $\Omega_m = 1$ *and* $\Omega_\Lambda = 0$*, we have that* $D(\tau) \sim a$*, which means that, with good approximation, in a matter-dominated universe* $D(\tau)$ *grows with the scale factor.* We now turn to the nonlinear case, but before solving these equations we can rewrite them in a more compact fashion. First of all we move from conformal time τ to a new time coordinate η defined by

$$\eta = \ln \frac{D(\tau)}{D(\tau_{in})}, \tag{2.12}$$

We then define a "doublet" field $\varphi_a(\mathbf{k},\eta)$ as

$$\varphi(\mathbf{k},\eta) = e^{-\eta} \begin{pmatrix} \delta(\mathbf{k},\eta) \\ -\theta(\mathbf{k},\eta)/\mathcal{H}f \end{pmatrix}, \tag{2.13}$$

where f is the growth function

$$f \equiv \frac{\mathrm{d}\ln D}{\mathrm{d}\ln a} \tag{2.14}$$

and a $2\times 2\times 2$ matrix function $\gamma_{abc}(\mathbf{p},\mathbf{q})$ whose only nonzero components are:

$$\gamma_{121}(\mathbf{p},\mathbf{q}) = \alpha(\mathbf{p},\mathbf{q})/2, \quad \gamma_{112}(\mathbf{q},\mathbf{p}) = \gamma_{121}(\mathbf{p},\mathbf{q}), \quad \gamma_{222}(\mathbf{p},\mathbf{q}) = \beta(\mathbf{p},\mathbf{q}). \tag{2.15}$$

The equation becomes:

$$(\delta^K_{ab}\partial_\eta + \Omega_{ab})\varphi_b(\mathbf{k},\eta) = I_{\mathbf{k};\mathbf{p},\mathbf{q}} e^{\eta}\gamma_{abc}(\mathbf{p},\mathbf{q})\varphi_b(\mathbf{p},\eta)\varphi_c(\mathbf{q},\eta). \tag{2.16}$$

We have introduced the notation:

$$I_{\mathbf{k};\mathbf{q}_1,\cdots\mathbf{q}_n} \equiv \int \frac{d^3q_1}{(2\pi)^3}\cdots\frac{d^3q_n}{(2\pi)^3}(2\pi)^3\delta_D(\mathbf{k}-\sum_{i=1}^{n}\mathbf{q}_i) \tag{2.17}$$

and the matrix

$$\Omega = \begin{pmatrix} 1 & -1 \\ -\frac{3}{2}\frac{\Omega_m}{f^2} & \frac{3}{2}\frac{\Omega_m}{f^2} \end{pmatrix}. \tag{2.18}$$

In this formalism, we can write the general linear solution as:

$$\varphi_a(\mathbf{k},\eta) = g_{ab}(\eta,\eta_{in})\varphi_b(\mathbf{k},\eta_{in}), \tag{2.19}$$

where the function $g_{ab}(\eta,\eta_{in})$ is called linear *propagator* (see Appendix A).

The quantity we are interested in is the two-point matter correlation function in Fourier Space, or matter *power spectrum* (PS):

$$\langle\varphi_a(\mathbf{k},\eta)\varphi_b(\mathbf{k}',\eta)\rangle \equiv (2\pi)^3\delta_D(\mathbf{k}+\mathbf{k}')P_{ab}(\mathbf{k},\eta). \tag{2.20}$$

The approach of Standard Perturbation Theory (SPT) is to expand the fields $\varphi_a(\mathbf{k},\eta)$ in powers of initial perturbations $\varphi_{a'}(\mathbf{k}',\eta_{in})$ taken at high redshift in which these fields are small and linear perturbation theory is supposed to hold at all scales of interest. The n-th order term of the expansion will be of the form:

$$\varphi_a^n(\mathbf{k},\eta) = I_{\mathbf{k},\mathbf{q}_1,\ldots,\mathbf{q}_n}G_{a,b_1,\ldots b_n}(\mathbf{q}_1,\ldots,\mathbf{q}_n)\varphi_{b_1}(\mathbf{q}_1,\eta_{in})\cdots\varphi_{b_n}(\mathbf{q}_n,\eta_{in}). \tag{2.21}$$

The Kernels $G_{a,b_1,\ldots b_n}(\mathbf{q}_1,\ldots,\mathbf{q}_n)$ can be determined either using a recursive relation or using a diagrammatic approach [21]. If we substitute this expansion in the expression for the PS, the expectation values becomes an expansion in the initial n-point correlation functions $\langle\varphi_{a_1}(\mathbf{q}_1,\eta_{in})\ldots\varphi_{a_n}(\mathbf{q}_n,\eta_{in})\rangle$. If we assume that the initial conditions are *Gaussian*, then we can apply Wick's theorem, which ensures that expectation values of an odd number of fields (having each zero mean) vanish, while those of an even number of fields reduce to a sum of products of initial PS's:

$$\begin{aligned}\langle\varphi(\mathbf{k}_1)\ldots\varphi(\mathbf{k}_{2p+1})\rangle &= 0,\\ \langle\varphi(\mathbf{k}_1)\ldots\varphi(\mathbf{k}_{2p})\rangle &= \sum_{\text{all contractions}}\prod_{\text{pairs, (i,j)}}\langle\varphi(\mathbf{k}_i)\varphi(\mathbf{k}_j)\rangle.\end{aligned} \tag{2.22}$$

So, for example, the first non-linear contribution to the PS will contain 4 initial fields φ, that is, 2 initial PS. This approximation is called *1-loop*, because of the topology of its diagrammatic representation (See Appendix A) and because it involves integration over one momentum. The next-to-leading contribution will accordingly contain 3 initial PS and will be called *2-loop* and so on.

SPT is known to perform fairly well at large scales and early redshift while it breaks down at small redshift ($z \lesssim 2$) and smaller scale ($k \gtrsim 0.1$ h/Mpc).

The problem is not solved by going to higher orders. Ref.[22] performed the calculation up to 3-loop order and showed that at redshift smaller than ≈ 1.75 the agreement of the 3-loop correction with N-body simulations is even worse than the 2-loop, showing that the series is converging at most asymptotically. This is to be expected since the mode coupling function $e^{\eta}\gamma_{abc}(\mathbf{k},\mathbf{p},\mathbf{q})$ grows with the time η (alternatively, one can see SPT as an expansion around the linear solution, which also grows in time, exiting the perturbative regime once the densities become large). Furthermore at low redshift SSA no longer holds. In the following sections we will review some proposals to improve upon the results of SPT.

2.1.2 Response function

A key feature of nonlinear dynamics is that different modes are coupled to each other. Since the interaction term in the equations of motion, Eq. 2.16 is integrated over all momenta, in principle each scale k has an effect on all the others. However we do not expect them to contribute all in the same way, so when calculating the PS at a scale k we would like to know which range of scales are going to affect its evolution the most. A quantitative formulation of this question can be found in the *linear response function* (LRF):

$$K_{ab}(k,q;\eta,\eta') \equiv q^3 \int d\Omega_{\mathbf{q}} \frac{\delta P_{ab}[P^0](\mathbf{k};\eta,\eta')}{\delta P^0(\mathbf{q})}. \tag{2.23}$$

This function tells us how sensitive the final nonlinear PS, calculated at a given scale $\mathbf{k}$, is to a slight variation in the initial (linear) PS $P^0(\mathbf{q})$. Ref. [23] calculated the LRF using N-body simulations and compared the result to the perturbative approaches. They showed that the dynamics in the PS displays a "screening effect" through which, as we get closer to the present redshift, intermediate scales become increasingly insensitive to the small UV scales. This effect is completely missed by SPT which predicts a LRF which is flat or even growing with $\mathbf{k}$. This is related to the breakdown of SSA after shell-crossing and is another proof that an alternative method must be used in order to treat the very small scales. The Coarse Graining approach in the following sections will provide one such example.

2.2 IR-resummation and Galilean Invariance

We know (e.g. from N-body simulations) that nonlinear dynamics have the effect of broadening the BAO peak in the real-space DM correlation function [24, 25]. This translates in a damping in the oscillating features of the PS. The main physical effect responsible for this is the long range *bulk motions* of matter, coherent on scales up to ≈ 100 Mpc/h with a rms displacement of ≈ 6 Mpc/h.

In order to tackle this problem we can employ two complementary approaches: we can model the damping or act on the data and reconstruct the peak by "reversing" the effect of the bulk motions. As we will see in Chapter 5, they can be employed simultaneously. In this section we focus on the modelling approach (the "Reconstruction" technique is discussed in Section 5.1). The nonlinear damping effect is missed by SPT, however it can be recovered with a resummation of a subset of diagrams [26, 27]. When loop momenta are "soft", i.e. much smaller than the momentum flowing in and out of the loop, the leading contribution of the mode coupling assumes a simple form that can be resummed at all orders. The remaining contributions are truncated at a finite order. This procedure goes by the name of *Renormalized Perturbation Theory* (RPT) and it can be shown that it is equivalent to substituting, in the SPT expression for the PS, the original propagator with a damped one.

$$g_{ab}(\mathbf{k},\eta) \longrightarrow G_{ab}(\mathbf{k},\eta) \equiv g_{ab}(\mathbf{k},\eta) e^{-\frac{k^2\sigma_v^2}{2}(e^\eta - e^{\eta_{in}})^2}, \tag{2.24}$$

where

$$\sigma_v^2 \equiv \frac{1}{3}\int d^3p \frac{P_0(p)}{p^2} \tag{2.25}$$

is the linear velocity dispersion. The damping factor in the new propagator encodes the fact that memory of the initial condition is partly erased by the nonlinear evolution. However the simple implementation we just mentioned violates a fundamental symmetry that is *Galilean Invariance* (GI) [28, 26]. In the context of cosmology a Galilean Transformation is a mapping of the proper coordinates $(\mathbf{r}, t)$:

$$\begin{aligned} \mathbf{r}' &= \mathbf{r} - \mathbf{u}t \\ \mathbf{V}'(\mathbf{r}') &= \mathbf{V}(\mathbf{r}) - \mathbf{u}, \end{aligned} \tag{2.26}$$

where $\mathbf{V} \equiv \mathbf{dr}/\mathbf{dt}$ and $\mathbf{u}$ is a uniform but possibly time-dependent velocity. The Equivalence Principle requires equal-time correlators to be invariant under this transformation. This symmetry can in fact be exploited. Individual loop diagrams in SPT contain IR divergences in the integral over loop momenta, but the sum of all the loop diagrams at any given order is found to be finite. This order by order cancellation of divergences is protected by GI [29]. Any finite order in RPT does not respect GI, since it includes infinite SPT orders, via the resummed propagator, Eq. 2.24, whose IR contributions are only partially cancelled. One consequence of this is that it does not reproduce the correct decoupling of intermediate scales from large ones. It can be shown [30] that GI implies that the effect of a IR mode q on a mode k in the LRF, with $q \ll k$, decouples ad q^3/k^3. On the other hand, in RPT, the decoupling is only as q/k. Several GI resummation schemes have been proposed, like those of [31, 32, 33]. We can make sure our proposal is consistent with GI by making use of a set of *consistency relations* [34, 35]. Similarly to how, in particle theory, gauge symmetry is enforced by Ward Identities, GI symmetry imposes constraints on the relation between correlators. This identities can be used to construct a GI formulation or to check if a particular scheme respects GI. In Section 3.4 we will use these consistency relations to derive a GI resummation of these IR effects.

Finally we stress that modelling the IR contribution is particularly important when evaluating the PS in the BAO region, since the long-range bulk motions are mainly responsible for the damping of the BAO peaks [24].

2.3 UV effects and effective theories

As mentioned in the preceding sections SPT breaks down at small scales and low redshift. This is expected since gravity pulls matter together making the denser regions grow even denser with time. This alone would bring the system out of the perturbative regime. On top of this as structure starts to form and virialize, higher moments of the Vlasov equation, which are neglected in SPT, become important. Thus SSA is not valid anymore and velocity dispersion becomes important and has to be taken into account. Calculations of the linear response function, Eq. 2.23, from N-body simulations compared to perturbative approaches show that the mildly nonlinear scales are weakly sensitive to variations in the very small scales. This screening mechanism is missed by SPT. On one hand N-body simulations are able to capture this

small scale dynamics, since they solve for the exact equations. On the other hand, doing so requires a high resolution which, paired to the large volumes and number of realisations required to measure the BAO feature, makes this approach very time consuming. These considerations suggested the use of an *effective* approach. Several proposals have been presented in this sense, such as the Effective Field Theory of Large Scale Structure (EFToLSS) and similar [36, 37, 38] or Coarse Grained Perturbation Theory (CGPT) [39, 40]. The common idea behind these approaches is to integrate out the small scale modes (performing a smoothing of the Vlasov equations) and replace them with effective terms in the equations of motions. Since these new source terms are not accessible via perturbative means some other input is needed in order to determine them. The approach of EFToLSS is to expand the sources in powers of the perturbative large scale fields and determine the coefficients of the expansion by fitting the full PS. CGPT tries to measure these sources directly from simulations, usually in the form of correlators with the full nonlinear fields. We will briefly show how the source terms emerge from the smoothing procedure, following the notation of [40].

We start from the Vlasov equation, Eq. 2.1 and define a smoothing (or coarse graining) function $W(\mathbf{x}/R)$, which decays as $x \ll R$. If we consider a field $g(\mathbf{x})$, it is filtered by taking the convolution:

$$\bar{g}(\mathbf{x}) \equiv \int d^3y \; W(\mathbf{y}/R) g(\mathbf{x}-\mathbf{y}). \tag{2.27}$$

If we filter Vlasov's equation and derive the new continuity and Euler equations in terms of filtered quantities we obtain:

$$\begin{aligned} &\frac{\partial}{\partial\tau}\bar{\delta}(\mathbf{x},\tau) + \frac{\partial}{\partial x^i}\left[\left(1+\bar{\delta}(\mathbf{k},\tau)\right)\bar{v}^i(\mathbf{x},\tau)\right] = 0 \\ &\frac{\partial}{\partial\tau}\bar{v}^i(\mathbf{x},\tau) + \mathcal{H}(\tau)\bar{v}^i(\mathbf{x},\tau) + \bar{v}^k\frac{\partial}{\partial x^k}\bar{v}^i(\mathbf{x},\tau) = -\nabla^i_x\bar{\phi}(\mathbf{x},\tau) - J^i_1 + J^i_\sigma. \end{aligned} \tag{2.28}$$

The continuity equation is unchanged, while in the Euler equation we have an additional source terms J^i that contains all the modes that have been

integrated out.

$$
\begin{aligned}
&J_1^i(\mathbf{x},\tau) = \\
&\quad \frac{1}{1+\bar{\delta}(\mathbf{x},\tau)} \int d^3y\; W\left(\frac{\mathbf{x}-\mathbf{y}}{R}\right)(1+\delta(\mathbf{y},\tau))\nabla^i\phi(\mathbf{y},\tau) - \nabla^i\bar{\phi}(\mathbf{x},\tau) \\
&J_\sigma^i(\mathbf{x},\tau) = \\
&\quad \frac{1}{1+\bar{\delta}(\mathbf{x},\tau)} \frac{\partial}{\partial x^j}\left[(1+\bar{\delta}(\mathbf{x},\tau)\bar{\sigma}^{ij}(\mathbf{x},\tau\right].
\end{aligned}
\tag{2.29}
$$

The compact notation will have the form:

$$
(\delta_{ab}\partial_\eta + \Omega_{ab})\bar{\varphi}_b(\mathbf{k},\eta) = I_{\mathbf{k},\mathbf{q}_1,\mathbf{q}_2} e^\eta \gamma_{abc}(\mathbf{q}_1,\mathbf{q}_2)\bar{\varphi}_b(\mathbf{q}_1,\eta)\bar{\varphi}_c(\mathbf{q}_2,\eta) - h_a(\mathbf{k},\eta),
\tag{2.30}
$$

where the UV contribution is contained in

$$
h_a(\mathbf{k},\eta) = -i\frac{k^i}{\mathcal{H}^2 f^2}\left[J_1^i(\mathbf{k},\eta) + J_\sigma^i(\mathbf{k},\eta)\right] e^{-\eta}\delta^K_{a2}.
\tag{2.31}
$$

In the above expressions, the contribution from the microscopic vorticity is contained in the source terms h_a. The vorticity generated by the filtering procedure will be treated perturbatively (see next chapter).

The approach is semi-analytic, in the sense that we will still perform a perturbative calculation of the PS at some finite order. However we are going to *subtract* from this PS the contribution from the coupling to the small scales, namely the source terms $h_a(\mathbf{k},\eta)$, evaluated in SPT and substitute them with the corresponding terms measured from N-body simulations, which give the correct mode-coupling to the UV scales. This subtraction is made at a finite perturbative order, therefore it is not perfect. As a consequence, a residual dependence on the coarse-graining scale R remains. R is only a parameter of the procedure, so this dependence is unphysical and unwanted. The reliability of the method is restricted to the range of scales in which the results do not change with R. In Ref. [40] it was shown that at higher redshift (z $\sim$ 1) the subtraction at 1-loop was able to reproduce the nonlinear PS on the whole BAO range, while at $z = 0$ it displayed a dependence on R even in the BAO region. In order to extend the range of validity to the whole BAO region a 2-loop calculation is required. The calculation of the terms at 2-loop involves the computation of tens of terms, but it has to be done only once, and after it is done the evaluation of the PS takes virtually no computational

effort, especially because the UV terms depend very weakly on the specific cosmological parameters and can be easily interpolated between cosmologies, without the need to run new simulations. For this reason these techniques offer a promising procedure to generate the nonlinear PS.

Chapter 3

Improved Time-Renormalization Group and the BAO Extractor operator

3.1 Introduction

In the preceding chapters we have made a quick review of SPT and its shortcomings. We then explained some of the strategies proposed to overcome them. In this chapter we are going to put these idea together and apply them to the Time-Renormalization Group (TRG) approach, originally presented in [41] to produce a UV- and IR-safe tool for generating the nonlinear PS. The aim of this chapter is to introduce the TRG equation with the corrections in the UV and IR sectors and the Extractor operator as a novel way to extract and study BAO information from a nonlinear PS. This work has been published on the Journal of Cosmology and Astrophysics (JCAP 1708 (2017) no.08, 007). [1]

[1] SISSA Medialab Srl. Reproduced with permission. All rights reserved

3.2 Evolution equation for the PS

Neglecting vorticity, the first two moments of the coarse-grained Vlasov equations [39, 40] give the continuity and Euler equations, which, in Fourier space, can be cast in compact form as

$$(\delta_{ab}\partial_\eta + \Omega_{ab})\varphi_b^R(\mathbf{k},\eta) = I_{\mathbf{k},\mathbf{q}_1,\mathbf{q}_2} e^\eta \gamma_{abc}(\mathbf{q}_1,\mathbf{q}_2)\varphi_b^R(\mathbf{q}_1,\eta)\varphi_c^R(\mathbf{q}_2,\eta) - h_a^R(\mathbf{k},\eta)\,, \tag{3.1}$$

where $\eta = \log D(\tau)$ and $I_{k;p_1,\cdots,p_n} \equiv \int \frac{d^3p_1}{(2\pi)^3}\cdots\frac{d^3p_n}{(2\pi)^3}(2\pi)^3\delta_D(\mathbf{k}-\sum_{i=1}^n \mathbf{p}_i)$.

We have introduced the fields

$$\varphi_1^R(\mathbf{k},\eta) \equiv \mathrm{e}^{-\eta}\bar{\delta}_R(\mathbf{k},\eta) \quad , \qquad \varphi_2^R(\mathbf{k},\eta) \equiv \mathrm{e}^{-\eta}\frac{-\bar{\theta}^R(\mathbf{k},\eta)}{\mathcal{H}f}\,, \tag{3.2}$$

where we have also used the linear growth function $f(\eta) \equiv \frac{1}{\mathcal{H}}\frac{d\eta}{d\tau}$. Repeated indices are summed over $b, c = 1, 2$. The overbars indicate fields obtained by Fourier transforming $[\delta]_R(\mathbf{x},\eta)$ and the divergence of $[(1+\delta)v^i]_R(\mathbf{x},\eta)/[1+\delta]_R(\mathbf{x},\eta)$, respectively, where $[\cdots]_R$ indicates filtering up to some scale R (see sect. 3.3 and refs. [39, 40] for details).

The left hand side of this relation is the linearized part of the equation for the two dynamical modes, and it is characterized by the matrix

$$\mathbf{\Omega} = \begin{pmatrix} 1 & -1 \\ -\frac{3}{2}\frac{\Omega_m}{f^2} & \frac{3}{2}\frac{\Omega_m}{f^2} \end{pmatrix}. \tag{3.3}$$

The first term on the right hand side of eq. (3.1) encodes the mode-coupling between the fields. The only nonvanishing components of the vertex functions are

$$\gamma_{121}(\mathbf{p},\mathbf{q}) = \frac{(\mathbf{p}+\mathbf{q})\cdot\mathbf{p}}{2p^2} \quad \gamma_{112}(\mathbf{q},\mathbf{p}) = \gamma_{121}(\mathbf{p},\mathbf{q}) \quad \gamma_{222} = \frac{(\mathbf{p}+\mathbf{q})^2\,\mathbf{p}\cdot\mathbf{q}}{2p^2q^2} \tag{3.4}$$

The mode-coupling term can also be written as

$$\begin{aligned} e^\eta\gamma_{abc}(\mathbf{q}_1,\mathbf{q}_2)\varphi_b^R(\mathbf{q}_1,\eta)\varphi_c^R(\mathbf{q}_2,\eta) &= e^\eta\delta_{a2}\,\tilde{\gamma}(\mathbf{q}_1,\mathbf{q}_2)\varphi_2^R(\mathbf{q}_1,\eta)\varphi_2^R(\mathbf{q}_2,\eta) \\ &\quad -ik^j\frac{\bar{v}_R^j(\mathbf{q}_1)}{\mathcal{H}f}\varphi_a^R(\mathbf{q}_2,\eta)\,, \end{aligned} \tag{3.5}$$

with

$$\tilde{\gamma}(\mathbf{q}_1, \mathbf{q}_2) = \frac{(\mathbf{q}_1 \cdot \mathbf{q}_2)^2}{q_1^2 q_2^2} - 1 \,. \tag{3.6}$$

When $q_1 \ll k \simeq q_2$ the second term at the RHS of (3.5) singles out the leading contributions to the mode-coupling induced by long (and time-dependent) velocity modes, whose form is dictated by the Galilean invariance of the system [28, 35, 42]. Expressing the velocity through its divergence, it gives the (formally) IR divergent term

$$e^{\eta} \frac{\mathbf{k} \cdot \mathbf{q}_1}{q_1^2} \varphi_2^R(\mathbf{q}_1, \eta) \varphi_a^R(\mathbf{q}_2, \eta) \,, \tag{3.7}$$

where we have used the definition (3.2). In sect. 3.4 we will discuss the resummation of these effects at all orders. On the other hand, the residual vertex function, eq. (3.6), amounts to $\cos(\theta_{12})^2 - 1$, where θ_{12} is the angle between $\mathbf{q}_1$ and $\mathbf{q}_2$, and therefore it is never divergent, and moreover vanishes for $\mathbf{k} = \mathbf{q}_1 + \mathbf{q}_2 \to 0$.

The last term on the right hand side of eq. (3.1) is the contribution from the short modes that have been integrated out in the coarse-graining procedure [39, 40],

$$h_a^R(\mathbf{k}, \eta) \equiv -i \, \frac{k^i J_R^i(\mathbf{k}, \eta)}{\mathcal{H}^2 f^2} e^{-\eta} \delta_{a2} \,, \tag{3.8}$$

where the UV source $J_R^i(\mathbf{k}, \eta)$ is the Fourier transformed of

$$J_R^i(\mathbf{x}, \eta) = J_{1,R}^i(\mathbf{x}, \eta) + J_{\sigma,R}^i(\mathbf{x}, \eta) \,, \tag{3.9}$$

which depends on the gravitational potential ϕ and the velocity dispersion σ_R^{ik},

$$\begin{aligned} J_{1,R}^i(\mathbf{x}, \eta) &= \frac{1}{[1+\delta]_R(\mathbf{x}, \eta)} [(1+\delta)\nabla^i \phi]_R(\mathbf{x}, \eta) - \nabla^i [\phi]_R(\mathbf{x}, \eta) \,, \\ J_{\sigma,R}^i(\mathbf{x}, \eta) &= \frac{1}{[1+\delta]_R(\mathbf{x}, \eta)} \frac{\partial}{\partial x^k} \left[[1+\delta]_R(\mathbf{x}, \eta) \sigma_R^{ik}(\mathbf{x}, \eta) \right] \,. \end{aligned} \tag{3.10}$$

Applying the equation of motion (3.1) to the (equal-time) PS,

$$P_{ab}^R(k) = \langle \varphi_a^R(\mathbf{k}) \varphi_b^R(-\mathbf{k}) \rangle' \,, \tag{3.11}$$

– where the prime indicates that we have divided by $(2\pi)^3$ times the overall momentum delta function – gives

$$\partial_\eta P^R_{ab}(k) = \Bigg[- \Omega_{ac} P^R_{cb}(k) + e^\eta I_{\mathbf{k};\mathbf{p}_1,\mathbf{p}_2} \gamma_{acd}(\mathbf{p}_1,\mathbf{p}_2) B^R_{bcd}(k,p_1,p_2) \\ - \langle h^R_a(\mathbf{k}) \varphi^R_b(-\mathbf{k}) \rangle' + (a \leftrightarrow b) \Bigg], \tag{3.12}$$

where we have omitted the η-dependence, and where the bispectrum is given by

$$B^R_{abc}(q_1,q_2,q_3) = \langle \varphi^R_a(\mathbf{q}_1) \varphi^R_b(\mathbf{q}_2) \varphi^R_c(\mathbf{q}_3) \rangle' \,. \tag{3.13}$$

Before proceeding, we emphasize that the only approximation in the equation above is in the way we deal with the vorticity of the coarse-grained velocity field. This has two components: a microscopic one, related to UV scales smaller than R, and one induced by the coarse-graining procedure itself. While the first one is completely included in the source terms h^R_a, we deal with the second one at a perturbative level. While in this section we have set the second vorticity component to zero from the beginning, one can show, using the methods of [40], that including it perturbatively would give exactly the same equations as those considered in the next sections. The effect of vorticity on the PS was investigated in [43], where it was found to be negligible at all scales and redshifts of interest.

No other approximation has been imposed so far. In particular, we are not assuming the single stream approximation, as it is usually done in SPT and other semi-analytic methods. Eq. (3.1), and its PS counterpart, eq. (3.12), contain all the relevant physics: the effect of the UV scales on the intermediate ones, through the source h^R_a, the mode-coupling between the intermediate scales, through the vertex functions, and the IR displacements in the terms containing the vertex (3.7) for $q_1 \ll k$. In the following, we will discuss how to deal with all these effects.

3.3 UV effects

The source term h^R_a is responsible for all deviations from the single stream approximation and all the nonlinear effects occurring at small scales. It is therefore cleaner to consider the subtracted PS,

$$\Delta P^R_{ab}(k) \equiv P^R_{ab}(k) - P^{R,ss}_{ab}(k) \,, \tag{3.14}$$

where $P^{R,ss}_{ab}(k)$ is the PS computed in the single stream approximation. It solves an equation analogous to (3.12), in which all the quantities, including the $\langle h^R_a \varphi^R_b \rangle'$ correlator are obtained in the single stream approximation, in practice, by considering SPT or other approximation schemes at some finite order. This correlator vanishes in the $R \to 0$ limit while its value at nonvanishing R takes into account all nonlinear effects due to modes $q \gtrsim 1/R$ in the single stream approximation, to be subtracted from the fully nonperturbative correlator measured in N-body simulations. Working at finite R is essential in practice, in order to extract the source terms from the simulation, but the final results should be independent on the value chosen for R. We discuss this point below.

The evolution equation for the subtracted PS therefore reads

$$\partial_\eta \Delta P^R_{ab}(k) = \Bigg[- \Omega_{ac} \Delta P^R_{cb}(k) + e^\eta I_{\mathbf{k};\mathbf{p}_1,\mathbf{p}_2} \gamma_{acd}(k,p_1,p_2) \Delta B^R_{bcd}(k,p_1,p_2) \\ - \Delta \langle h^R_a(\mathbf{k}) \varphi^R_b(-\mathbf{k}) \rangle' + (a \leftrightarrow b) \Bigg], \tag{3.15}$$

where $\Delta \langle h^R_a(\mathbf{k}) \varphi^R_b(-\mathbf{k}) \rangle' \equiv \langle h^R_a(\mathbf{k}) \varphi^R_b(-\mathbf{k}) \rangle' - \langle h^{R,ss}_a(\mathbf{k}) \varphi^{R,ss}_b(-\mathbf{k}) \rangle'$. The subtracted bispectrum, $\Delta B^R_{abc}(k,p_1,p_2) \equiv B^R_{abc}(k,p_1,p_2) - B^{R,ss}_{abc}(k,p_1,p_2)$, in turn, solves the equation

$$\begin{aligned} &\partial_\eta \Delta B^R_{abc}(k,q,p) = \\ &\Bigg[- \Omega_{ad} \Delta B^R_{dbc}(k,q,p) - \Delta \langle h^R_a(\mathbf{k}) \varphi^R_b(\mathbf{q}) \varphi^R_c(\mathbf{p}) \rangle' \\ &+ 2 e^\eta \gamma_{aef}(k,q,p) \left(\Delta P^R_{eb}(q) P^{R,ss}_{fc}(p) + P^{R,ss}_{eb}(q) \Delta P^{R,ss}_{fc}(p) + \Delta P^R_{eb}(q) \Delta P^R_{fc}(p) \right) \\ &+ e^\eta I_{\mathbf{k};\mathbf{p}_1,\mathbf{p}_2} \gamma_{ade}(k,p_1,p_2) \Delta T^R_{debc}(\mathbf{p}_1,\mathbf{p}_2,\mathbf{q},\mathbf{p}) \\ &+ \text{cyclic permutations of } (a,\mathbf{k}),\ (b,\mathbf{q}),\ (c,\mathbf{p}) \Bigg], \end{aligned} \tag{3.16}$$

where $\Delta \langle h^R_a \varphi^R_b \varphi^R_c \rangle' \equiv \langle h^R_a \varphi^R_b \varphi^R_c \rangle' - \langle h^{R,ss}_a \varphi^{R,ss}_b \varphi^{R,ss}_c \rangle'$ and we have defined the deviation from the single stream approximation of the trispectrum, $\Delta T^R_{debc} \equiv T^R_{debc} - T^{R,ss}_{debc}$, which, in turn, solves an evolution equation which can be straightforwardly derived.

The system of coupled evolution equations solved by the subtracted correlation functions must be truncated at some order. However, unlike the original TRG proposal [41], where the evolution equations for the unsubtracted functions were considered, there is a clear hierarchy in these equations which leads to a natural criterium for the truncation. Indeed, we first notice that the sources of these equations are given by the $\Delta\langle h_a^R \varphi_{b_1}^R \varphi_{b_2}^R \cdots \varphi_{b_n}^R\rangle'$ correlators, since, if they all vanish, the single stream approximation is exact. Moreover, the role of these differences between correlators is to replace the "wrong" behavior of the UV modes in the single stream approximation with the "correct" ones, encoded in the correlators measured, for instance in N-body simulations. However, while the two-point correlator $\langle h_a^{R,ss} \varphi_{b_1}^{R,ss}\rangle'$ starts contributing to the UV loops for $P_{ab}^{R,ss}(k)$ at 1-loop order, $\langle h_a^{R,ss} \varphi_{b_1}^{R,ss} \varphi_{b_2}^{R,ss}\rangle'$ does it only from 2-loop, since it corrects the single-stream bispectrum at 1-loop order, and so on. In summary, if we want to correct the UV-loops behaviour of the $l-$loop order PS, then we need consider only the correlators up to $\Delta\langle h_a^R \varphi_{b_1}^R \varphi_{b_2}^R \cdots \varphi_{b_l}^R\rangle'$, and, correspondingly, only the first l equations of the system.

At the lowest order, we will therefore have

$$P_{ab}^R(k) \simeq P_{ab}^{R,1-loop}(k) + \Delta P_{ab}^{R,1-loop}(k)\,, \tag{3.17}$$

where $P_{ab}^{R,1-loop}(k)$ is the PS computed at 1-loop SPT with the linear PS filtered at the scale R, while $\Delta P_{ab}^{R,-1loop}(k)$ is obtained from eq. (3.15) with $\Delta B_{bcd}^R(k, p_1, p_2) = 0$ and $\Delta\langle h_a^R(\mathbf{k})\varphi_b^R(-\mathbf{k})\rangle'$ subtracted at 1-loop.

In order to go to next order, one has to take into account the 2-loop PS and include eq. (3.16), with $\Delta T^R = 0$ and the three point correlator $\langle h_a^R \varphi_{b_1}^R \varphi_{b_2}^R\rangle'$ subtracted at 1-loop order.

As we anticipated above, the total PS, eq. (3.17), should not depend on the coarse graining scale R apart from an overall dependence on the filter function. For instance, the density-density PS should depend on R only through a $W[kR]^2$ factor, where $W[kR]$ is the filter function in Fourier space. The same holds for the PS computed in the single stream approximation at a finite loop order (see [40] for a 1-loop check). Therefore, one has to check that no spurious R-dependence is induced by the difference between the source correlator measured in simulations and that computed in SPT. Indeed, each of them, taken separately, has a strong R-dependence, as shown in the left

panel of fig. 3.1, where we use the parameterization

$$\langle h_a^R(\mathbf{k})\varphi_b^R(-\mathbf{k})\rangle' = \alpha^R(\eta)\frac{k^2}{k_m^2}P_{1b}^R(k;\eta)\,\delta_{a2}\,, \tag{3.18}$$

and we plot the quantities $\alpha^R(\eta)$, $\alpha^{R,ss}(\eta)$, and the difference between the two (for $b = 1$). The simulations we use were presented already in [40], see Appendix B for details. They are based on the TreePM code GADGET-II [44]. They follow the evolution, until z = 0, of $n_{part} = 512^3$ CDM particles within a periodic box of $L_{box} = 512h^{-1}$Mpc comoving. The initial conditions were generated at z = 99 by displacing the positions of the CDM particles, that were initially set in a regular cubic grid, using the Zel'dovich approximation. We assumed the "REF" cosmological parameters of [40], namely, $\Omega_m = 0.271$, $\Omega_b = 0.045$, $\Omega_\Lambda = 0.729$, $h = 0.703$, $n_s = 0.966$, and $A_s = 2.42 \times 10^{-9}$.

As we see, for the scales of interest, the R-dependence of the correlator measured in N-body simulations is mostly cancelled by the perturbative one already at 1-loop, so that a function that is approximately R-independent,

$$\Delta\alpha(\eta) = \alpha^R(\eta) - \alpha^{R,ss}(\eta)\,, \tag{3.19}$$

can be defined. The residual R-dependence, is given by two contributions: nonlinear effects from scales $q \gtrsim 1/R$ not captured by the 1-loop subtraction, and non-perturbative (that is, beyond single-stream) effects from scales $q \lesssim 1/R$. The magnitude of these effects decreases with the external momentum k, and, as we see from this plot, they are clearly subdominant for k in the BAO range of scales. The complementary information to the left panel of Fig. 3.1 is given in the right panel of the figure, where the scale-dependence of the ratio between the correlator and the PS is given, and the k^2 dependence clearly emerges.

Notice that the $\Delta\alpha(\eta)$ function bears some analogies with the sound speed coefficient in the EFToLSS [37], however, with some key differences, that we now outline. First of all, the stress tensor in [37], whose divergence gives basically our source terms, eq. (3.10), is expanded in terms of the linear filtered fields, and therefore the coefficients of this expansion are obtained from the cross-correlator of the sources with the linear fields. Here, on the other hand, the relevant cross-correlators involve the sources and the nonlinear fields φ_a^R, and therefore include effects, like short scale displacements and source-source correlators ($\langle h_a^R h_b^R\rangle'$, where the second h_b^R is contained in the

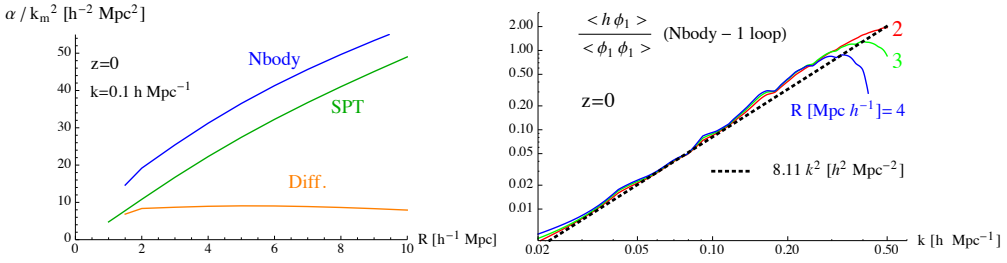

Figure 3.1: Dependence on the CG cutoff scale R of the coefficient $\frac{\alpha^R}{k_m^2}$ (blue curve), $\frac{\alpha^{R,ss}}{k_m^2}$ (green curve), and of their difference $\frac{\Delta\alpha}{k_m^2}$ (orange curve). The coefficients are obtained from $b = 1$ in eq. (3.18), for $k = 0.1h/\text{Mpc}$ and at $z = 0$. As discussed in the text, the difference exhibits a much smaller dependence on the cut-off scale. Right panel: Scale dependence of $\frac{k^2\,\Delta\alpha(z_0)}{k_m^2}$ for three different values of the cut-off scale R. The dotted curve is the theoretical prediction k^2 times a $z-$dependent coefficient, obtained as explained in B.

nonlinear evolution of the φ_b^R field) which are not included at 1-loop order in EFToLSS. Moreover, we will directly measure these sources, and the coefficient $\Delta\alpha(\eta)$, from N-body simulation and then include the result into our evolution equations for the PS. While this procedure can be followed also in the EFToLSS, more often, in practical applications, one first derives an expression for the PS containing the "sound speed" and other counterterms as parameters to be fitted from the PS measured in simulations. In doing so, the physical meaning of these counterterms is less transparent, and the amount of "overfitting", in order to get the PS right, is difficult to estimate.

In summary, we can choose R in the plateau region, or equivalently, take the formal $R \to 0$ limit, and consider the evolution equation

$$\partial_\eta \Delta P_{ab}(k;\eta) = \Big[- \Omega_{ac}\, \Delta P_{cb}(k;\eta) \\ -\Delta\alpha(\eta)\frac{k^2}{k_m^2}\left[P_{1b}^{1-loop}(k;\eta) + \Delta P_{1b}(k;\eta)\right]\, \delta_{a2} + (a \leftrightarrow b)\Big]\,. \tag{3.20}$$

In fig. 3.2 we show the ratios between eq. (3.17) (orange line) and the PS computed with the Coyote interpolator of N-body simulations [45]. The

agreement clearly improves over the 1-loop SPT result (blue line) showing that the UV correction represented by the h_a^R sources plays a decisive role, already at the lowest order considered here, namely, correcting the UV of the 1-loop PS. At $k = 0.1\,h\,\mathrm{Mpc}^{-1}$, the source correlator modifies the PS by $\simeq -0.6\%$ at $z = 1$, by $\simeq -1.1\%$ at $z = 0.5$, and by $\simeq -1.8\%$ at $z = 0$. The agreement in the PS shape degrades at low redshifts, where higher loop orders should be taken into account along the lines discussed below eq. (3.16). However, in the following, we focus our attention on the residual BAO oscillations exhibited by the orange lines, which indicate that only improving the UV effects does not account for the BAO damping well enough. In the next section we will discuss how to deal with this issue.

3.4 IR resummation and BAO wiggles

The damping of the BAO wiggles in the PS, and of the corresponding peak in the correlation function is mainly caused by random long range displacements [25]. It is well known that such effects are badly reproduced in SPT at any finite order, while they are much better taken into account by the Zel'dovich approximation, which provides a resummation at all SPT orders (see for instance, [46]). In our approach, the effect of these long range displacements on an intermediate scale k are encoded in the last term at the RHS of eq. (3.5) when the momentum of the velocity field is $q_1 \ll k$. We will now discuss how they can be naturally resummed.

Indeed, if one applies again the equation of motion, eq. (3.1), to the correlator $\langle\varphi_a(\mathbf{k},\eta)\varphi_b(-\mathbf{k},\eta)\rangle'$, to get the evolution equation for the PS, then, the last term at the RHS of eq. (3.5) gives

$$e^{\eta}\int\frac{d^3q}{(2\pi)^3}\,\frac{\mathbf{k}\cdot\mathbf{q}}{q^2}\Big[\langle\varphi_2(\mathbf{q})\varphi_a(\mathbf{k}-\mathbf{q})\varphi_b(-\mathbf{k})\rangle' + \langle\varphi_a(\mathbf{k})\varphi_b(-\mathbf{k}+\mathbf{q})\varphi_2(-\mathbf{q})\rangle'\Big]\,. \tag{3.21}$$

The consistency relations first derived in [35, 34] for the bispectrum give

$$\langle\varphi_2(\mathbf{q})\varphi_a(\mathbf{k}-\mathbf{q})\varphi_b(-\mathbf{k})\rangle' \simeq - e^{\eta}\frac{\mathbf{k}\cdot\mathbf{q}}{q^2}P^0(q)\,(P_{ab}(k) - P_{ab}(|\mathbf{k}-\mathbf{q}|)) + O\left(\left(\frac{q}{k}\right)^0\right), \tag{3.22}$$

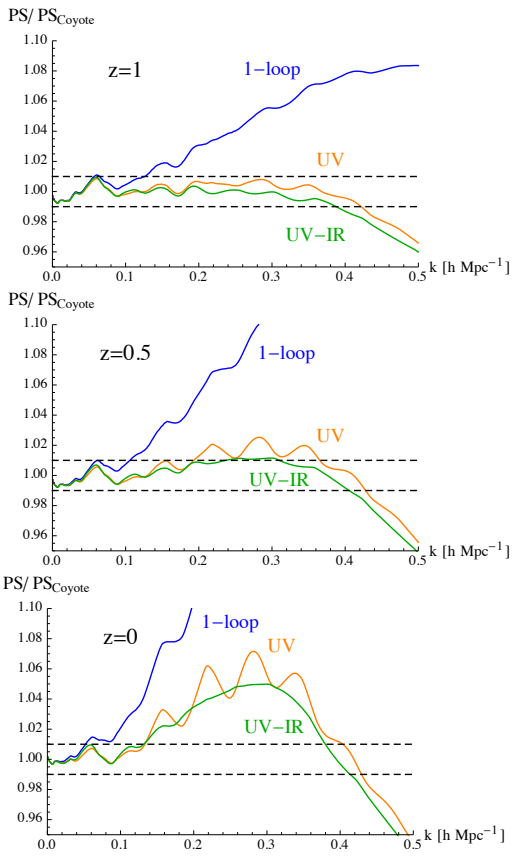

Figure 3.2: PS from different computational schemes divided by the Coyote PS. The blue curve is the 1-loop SPT result. The orange curve is obtained from the UV-improved ETRG system (3.20). The green curve is the UV- and IR-improved result (3.33). The different panels correspond to different redshifts. The UV-improved curve performs substantially better than the SPT result, however it is still does not properly reproduces the BAO oscillations, which are instead well reproduced by the UV- and IR-improved result. The horizontal dashed lines show the band for which our results differ less than $\pm 1\%$ from the Coyote PS.

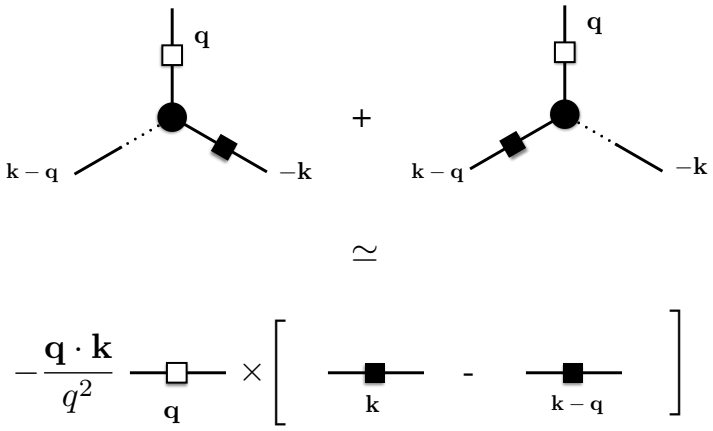

Figure 3.3: The consistency relations allow the bispectra appearing in eq. (3.21) to be rewritten as the product of a linear PS, $P^0(q)$, and a difference of nonlinear PS.

in the $q \ll k$ configuration. The consistency relation is depicted diagrammatically in fig. 3.3. The second term in (3.21) gives the same contribution.

Notice that, while $P^0(q)$ in eq. (3.22) is taken to be the linear PS, the other two are fully nonlinear. Moreover, the RHS vanishes at the leading order in q/k, that is, if one sets the argument of the second PS inside parentheses to k. This is in agreement with the form of the consistency relations derived in [35], which vanish if, as in this case, all the fields are taken at equal times. However, as we now show, the different arguments of the two PS is crucial when they have an oscillatory component.

Inserting (3.22) in (3.21) gives

$$
\begin{aligned}
&-2e^{2\eta}\int^{\Lambda(k)}\frac{d^3q}{(2\pi)^3}\left(\frac{\mathbf{k}\cdot\mathbf{q}}{q^2}\right)^2 P^0(q)\left(P_{ab}(k)-P_{ab}(|\mathbf{k}-\mathbf{q}|)\right)\\
&\simeq -2e^{2\eta}\frac{k^2}{(2\pi)^2}\int^{\Lambda(k)}dq\,P^0(q)\int_{-1}^{1}dx\,x^2\left(P_{ab}(k)-P_{ab}(k-qx)\right)\\
&=-2e^{2\eta}\frac{k^2}{(2\pi)^2}\int^{\Lambda(k)}dq\,P^0(q)\bar{P}^1_{ab}(k;q)\,F^1(q\,r_{bao})
\end{aligned}
\tag{3.23}
$$

where we have inserted a UV cutoff $\Lambda(k)\lesssim k$, in order to enforce the validity range of the consistency relation (3.22). We have defined

$$
\bar{P}^n_{ab}(k;q)\equiv\frac{\int_{-1}^{1}dx\,x^{2n}\left(1-\frac{P_{ab}(k-qx)}{P_{ab}(k)}\right)}{F^n(q\,r_{bao})}P_{ab}(k),
\tag{3.24}
$$

for $q\lesssim k$, with

$$
F^n(q\,r_{bao})\equiv\int_{-1}^{1}dx\,x^{2n}\left(1-\cos(q\,r_{bao}\,x)\right),
\tag{3.25}
$$

so that, $F^1(q\,r_{bao})=2\left(1-j_0(q\,r_{bao})+2j_2(q\,r_{bao})\right)/3$, where the $j_n(x)$ are the spherical Bessel functions.

If the nonlinear PS has an oscillatory component,

$$
P_{ab}(k)=P^{nw}_{ab}(k)(1+A_{ab}(k)\sin(k\,r_{bao}))\equiv P^{nw}_{ab}(k)+P^{w}_{ab}(k)\,,
\tag{3.26}
$$

with $A_{ab}(k)$ a smooth modulating function which damps the oscillations beyond the Silk scale, then eq. (3.24) returns the oscillatory component itself plus a smooth contribution,

$$
\bar{P}^n_{ab}(k;q)=P^w_{ab}(k)+O\left(P^{nw\prime\prime}_{ab}(k)/r^2_{bao}\right)\,,
\tag{3.27}
$$

and other terms proportional to derivatives of $A_{ab}(k)$, which are suppressed since the oscillatory part is proportional to Ω_b/Ω_m. Therefore, eq. (3.23) gives

$$
-2e^{2\eta}k^2\,\Xi(r_{bao})P^w_{ab}(k)+O\left(P^{nw\prime\prime}_{ab}\right)\,,
\tag{3.28}
$$

with

$$
\Xi(r_{bao})\equiv\frac{1}{6\pi^2}\int^{\Lambda(k)}dq\,P^0(q)\left(1-j_0(q\,r_{bao})+2j_2(q\,r_{bao})\right).
\tag{3.29}
$$

The exact value of the cut-off $\Lambda(k)$ (slightly) affects the amplitude of the evolved BAO's but not their scale, as one can see by comparing the three red lines (dashed, solid, and dotted) in Fig. 3.7, in which we plot the results for the oscillating part of the PS obtained by multiplying the integrand in (3.29) by $\exp(-q/(c\,k)^2)$ with $c = 1/2, 1, \infty$, respectively, and integrating in q from 0 to ∞. It should be noted that the integrand of eq. (3.23), as far as the oscillatory part is concerned, is naturally cut-off at the Silk scale. Therefore, even removing the UV cutoff altogether (setting $c = \infty$), scales $q \gtrsim k_{Silk} \simeq 0.12\,\mathrm{h/Mpc}$ do not contribute to the resummation.

If we now consider the equation for the PS derived in the previous section, and we add to it the IR resummation term, eq. (3.28), we have completed our goal: we have an evolution equation in which IR, intermediate, and UV scales are taken into account.

We note that the last line of eq. (3.23) has been obtained by multiplying and dividing the previous line by the function $F^1\left(q\,r_{bao}\right)$ specified in eq. (3.25). For PS of the form (3.26), the final line of of eq. (3.23) simplifies further into (3.27), where the scale r_{bao}, which is the comoving sound horizon at recombination, appears. For a given cosmology, we can compute the r_{bao} using eq. (6) of [47]. However, notice that the BAO extraction procedure defined in the next section is quite insensitive to the input r_{bao} value, see discussion after eq. (3.36).

We can consider also the same equation for a "smooth" cosmology, in which the initial PS has no BAO feature. They will not be generated by the evolution equation itself. If we subtract this equation from the one for the real cosmology, we get an evolution equation for the oscillatory component of the PS, in which the $O\left(P_{ab}^{nw\,\prime\prime}/r_{bao}^2\right)$ terms in (3.28) cancel out, which, splitting the oscillatory part as

$$P_{ab}^{w}(k;\eta) = P_{ab}^{w,ss}(k;\eta) + \Delta P_{ab}^{w}(k;\eta)\,, \tag{3.30}$$

gives the two equations

$$\partial_\eta P^{w,ss}_{ab}(k;\eta) = \Big[- \Omega_{ac}\, P^{w,ss}_{cb}(k;\eta) - \Omega_{bc}\, P^{w,ss}_{ac}(k;\eta) - 2e^{2\eta}k^2\, \Xi(r_{bao}) P^{w,ss}_{ab}(k) \Big] ,$$

$$\partial_\eta \Delta P^{w}_{ab}(k;\eta) = \Bigg[- \Omega_{ac}\, \Delta P^{w}_{cb}(k;\eta) - \alpha(\eta)\frac{k^2}{k_m^2} \Big[P^{1-loop,w}_{1b}(k;\eta) + \Delta P^{w}_{1b}(k;\eta) \Big]\, \delta_{a2} + (a \leftrightarrow b) \Bigg] , \tag{3.31}$$

with initial conditions $P^{w,ss}_{ab}(k;\eta_{in}) = P^{1-loop,w}_{ab}(k;\eta_{in})$, $\Delta P^{w}_{ab}(k;\eta_{in}) = 0$. If η_{in} is taken early enough, we can approximate $P^{1-loop,w}_{ab}(k;\eta_{in}) \simeq P^{0,w}(k) u_a u_b$ (where $\mathbf{u} = (1,1)$ and corresponds to taking the initial conditions in the growing mode), and the first equation has the analytical solution

$$P^{w,ss}_{ab}(k;\eta) = P^{0,w}(k) u_a u_b\, \exp[-e^{2\eta}k^2\, \Xi(r_{bao})] . \tag{3.32}$$

The total PS is obtained by adding the smooth component,

$$P_{ab}(k;\eta) = P^{nw}_{ab}(k;\eta) + P^{w}_{ab}(k;\eta) , \tag{3.33}$$

with

$$P^{nw}_{ab}(k;\eta) = P^{nw,1-loop}_{ab}(k;\eta) + \Delta P^{nw}_{ab}(k;\eta) , \tag{3.34}$$

where $\Delta P^{nw}_{ab}(k;\eta)$ solves an equation analogous to eq. (3.20),

$$\partial_\eta \Delta P^{nw}_{ab}(k;\eta) = \Bigg[- \Omega_{ac}\, \Delta P^{nw}_{cb}(k;\eta) - \alpha(\eta)\frac{k^2}{k_m^2} \Big[P^{1-loop,nw}_{1b}(k;\eta) + \Delta P^{nw}_{1b}(k;\eta) \Big]\, \delta_{a2} + (a \leftrightarrow b) \Bigg] . \tag{3.35}$$

3.5 Extracting the BAO

The solution for the total PS in which the effect of the IR displacement on the oscillating component has been taken into account by eqs. (3.31) are

given by the green lines in fig. 3.2 (for which we took $\Lambda = \infty$ in eq. (3.29)). The residual BAO oscillations are greatly reduced with respect to the results obtained in sect. 3.3, while the performance on the overall PS shape (the "broadband") is basically the same. This fact suggests that the evolutions of the two components of the PS, namely the smooth broadband shape and the oscillatory one, are governed by different physical effects: the mode-coupling with intermediate and UV scales for the former and long range displacements for the latter, with just a moderate amount of interference between them. To explore this possibility, we first look for a procedure to extract the oscillatory PS from a given PS, linear or nonlinear. Of course, this procedure has some degree of arbitrariness, as any small smooth function vanishing outside the BAO range of scales can be assigned either to the oscillatory or to the smooth part. However, the evolution equation itself suggests an optimal way to define such a procedure, as it extracts the oscillatory component which evolves (mostly) independently from the smooth one. Indeed, as we have seen, eq. (3.23) led us to define the wiggly component as in eq. (3.27), using eq. (3.24) (for $n = 1$). Therefore we will consider the operation,

$$\begin{aligned}\frac{\bar{P}^n(k;q)}{P(k)} &= \frac{\int_{-1}^{1} dx\, x^{2n} \left(1 - \frac{P(k-qx)}{P(k)}\right)}{\int_{-1}^{1} dx\, x^{2n} \left(1 - \cos(q\, r_s\, x)\right)} \\ &= \frac{\int_{-\Delta}^{\Delta} d\alpha\, \alpha^{2n} \left(1 - \frac{P(k-\frac{2\pi}{r_s}\alpha)}{P(k)}\right)}{\int_{-\Delta}^{\Delta} d\alpha\, \alpha^{2n} \left(1 - \cos(2\pi\alpha)\right)} \equiv R[P](k;\Delta,n), \end{aligned} \tag{3.36}$$

where r_s the wavelength associated to the comoving sound horizon of the assumed underlying cosmology. The parameter Δ, that we will call "range", determines the width of the momentum interval, centered on k and expressed in units of the BAO scale, over which we take the integral. The parameter n, on the other hand, is set to 1 in the evolution equation, and has no effect when the operation $R[P]$ is applied on theoretical PS's, but it might be useful on real data, when different bins are measured with different errors. Moreover, notice that the quantity r_s does not affect the scale of the oscillations extracted from the PS via eq. (3.36), as it is shown explicitly in Fig. 3.4. In other terms, the $R[P](k;\Delta,n)$ procedure extracts the scale of the true oscillations contained in $P(k)$, that is the r_{bao} of eq. (3.26), while the r_s parameter in eq. (3.36), which could also differ from the former, only affects the amplitude of the oscillations.

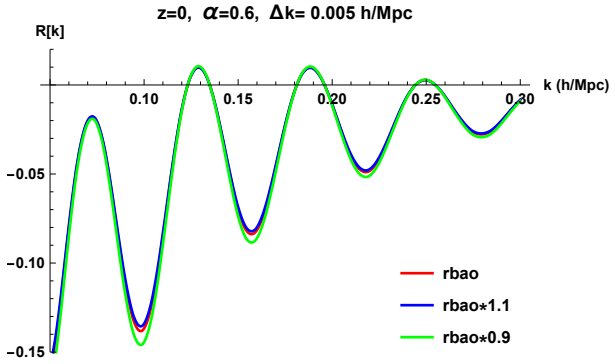

Figure 3.4: The BAO extractor $R[P](k;\Delta)$ applied to the linear PS using the value for r_{bao} in (3.36) corresponding to the one for the given cosmology (red), and to a value amplified (blue) and suppressed (green) by 10 % with respect to it. Changing r_{bao} slightly affects the amplitude of the oscillations but not the scale.

As indicated in (3.27), the ratio $R(k;\Delta,n)$ is "contaminated" by smooth terms coming from the non-oscillatory component of the PS, of order $\sim P''/(Pr_{bao}^2) \sim 1/(kr_{bao})^2$. This is clearly seen in fig. 3.5, where we show the action of the operation $R[P^0]$ on the linear PS (black dashed lines), and on a smooth interpolation of it, in which BAO oscillations are absent $R[P^{0,nw}]$ (red dotted lines)[2]. The difference between the two (black solid lines) oscillates around the x-axis. In the following plots, we will always subtract the same $R[P^{0,nw}]$ from all the different $R[P]$, in order to visualize oscillatory behaviors along the horizontal axis and, at the same time, keep the extraction procedure as simple as possible.

From the expression above, we can define a family of estimators for the ratio above. Assuming the data are binned, we can write

$$\hat{R}[P](k_m;\Delta,n) \equiv \frac{\sum_{l=-L(\Delta)}^{L(\Delta)} (k_{m+l}-k_m)^{2n}\left(1-\frac{P_{m+l}}{P_m}\right)}{\sum_{l=-L(\Delta)}^{L(\Delta)} (k_{m+l}-k_m)^{2n}\left(1-\cos\left(r_s\left(k_{m+l}-k_m\right)\right)\right)}\,, \tag{3.37}$$

where the value of the maximum $|l|$ in the sum, $L(\Delta)$, is chosen such that

$$|k_{m+l}-k_m| \leq \frac{2\pi\Delta}{r_s} \quad \text{for} \quad |l| \leq L(\Delta)\,. \tag{3.38}$$

[2]We thank Tobias Baldauf for sharing with us a code to extract the smooth PS.

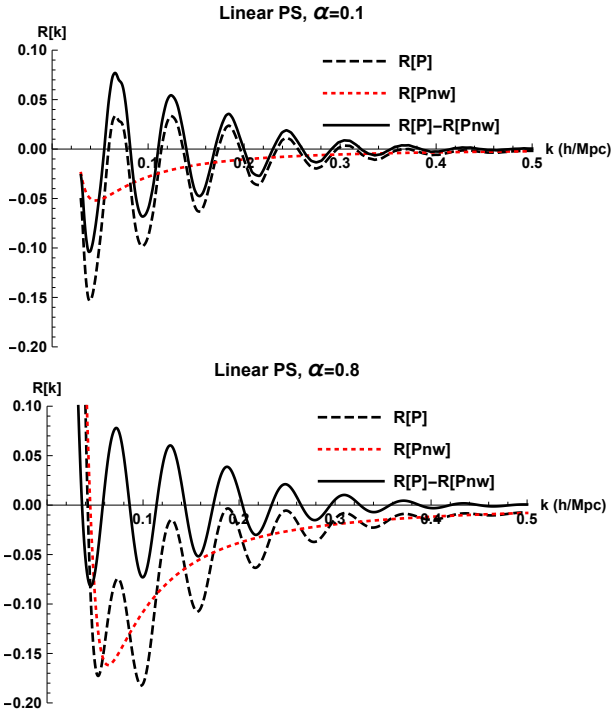

Figure 3.5: The BAO extractor $R[P](k;\Delta)$ applied to the linear PS (black-dashed line), to the smooth linear PS (red-dotted line), and their differences (black-solid line), for two different values of the range parameter Δ.

Assuming that the errors on the PS at different bins are uncorrelated, the error on $\hat{R}[P](k_m;\Delta,n)$ is given by

$$\Delta\hat{R}[P](k_m;\Delta,n) = \frac{\sqrt{\sum_{l\neq 0,l=-L(\Delta)}^{L(\Delta)}\left(k_{m+l}-k_m\right)^{4n}\left(\frac{P_{m+l}}{P_m}\right)^2\left[\left(\frac{\Delta P_m}{P_m}\right)^2+\left(\frac{\Delta P_{m+l}}{P_{m+l}}\right)^2\right]}}{\sum_{l=-L(\Delta)}^{L(\Delta)}\left(k_{m+l}-k_m\right)^{2n}\left(1-\cos\left(r_s\left(k_{m+l}-k_m\right)\right)\right)}\,. \tag{3.39}$$

The effect of correlation between the bins will be considered in the next chapter (see also Appendix F).

In fig. 3.6 we show the comparison between our results and the N-body simulations of ref. [48], which are optimised for the PS on the BAO scales. The UV cutoff in eq. (3.29) has been implemented by multiplying the integrand by the gaussian exponential $\exp(-(q/k)^2)$. To show the behavior of the discrete $R[P]$ (3.37), we have binned the N-body data in Δk intervals, and we have assumed a relative error $\Delta P_m/P_m = 0.01$ for the PS in each bin (the N-body curves shown in the figure are obtained from an interpolation of the binned data obtained from (3.37) and (4.7)).

In fig. 3.7 we show the sensitivity of our results to this choice, by removing the UV cutoff entirely (that is, by taking the gaussian exponential to 1). In the same plot, we show also the effect of neglecting the UV contribution, that is, of setting $\Delta P^w_{ab}(k) = \Delta P^{nw}_{ab}(k) = 0$ in eqs. (3.30), (3.34). This corresponds to using the 1-loop SPT results for the broadband part of the PS, which, as shown in fig. 3.2, reproduces the broadband part quite badly. Nevertheless, the effect on the oscillating part is given by the difference between the red and the black lines, which is barely recognisable on this plot scale.

3.6 Conclusions

The results of this chapter somehow pair with those of ref. [46] on the damping of the BAO peak in the correlation function. In that case, it was shown that the Zel'dovich approximation (and slights improvements of it) can account for the widening of the BAO peak which, rather than being a disturbance to be marginalised over, is a well controlled physical phenomenon

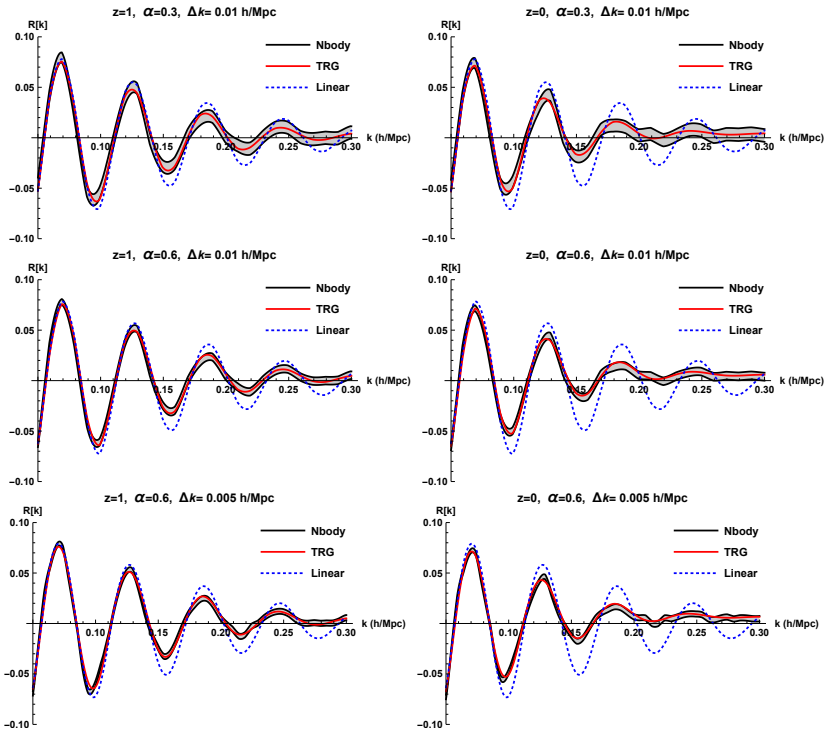

Figure 3.6: The extractor $R[P](k;\Delta)$ applied to the PS computed from N-body simulations (grey area) and to the TRG result described in the text at redshift $z = 1$ (left column) and at $z = 0$ (right column). Different values of the range parameter Δ and of the binning Δk are shown. The grey area corresponds to assuming an error $\frac{\Delta P_m}{P_m} = 1\%$ in each bin. The parameter n in (3.36) and (3.37) has been set to $n = 0$ We also show, in blue-dashed lines, the effect of the extractor applied to the linear PS. For visualisation purposes, the same quantity $R[P^{0,nw}](k)$, where $P^{0,nw}$ is the smooth component of the linear PS, has been subtracted from all the different $R[P](k)$.

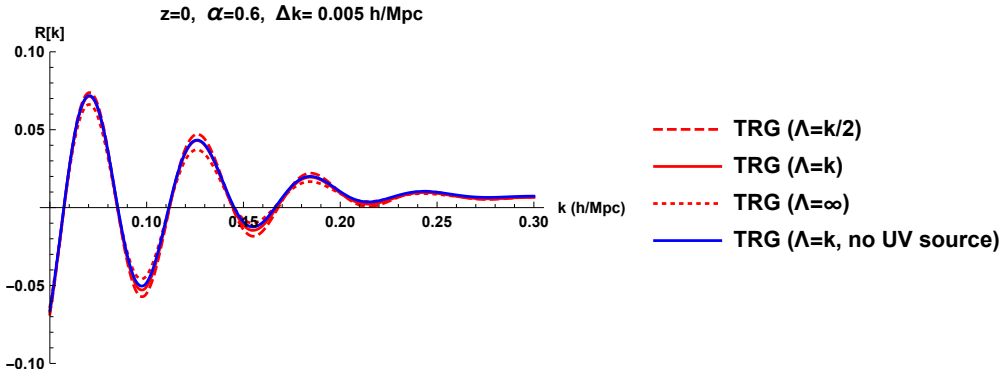

Figure 3.7: The effect of the UV "sound speed" contribution can be quantified by comparing the red and blue solid lines, which, respectively, have been obtained with and without UV sources and with the same IR contributions. The cut-off $\Lambda(k)$ in eq. (3.29) is implemented by multiplying the integrand by $\exp(-q^2/(c\,k)^2)$ and by integrating in q from 0 to ∞. The red lines have been obtained with the same UV contribution and using different values for the c constant in the IR resummation. The solid line has been obtained with $c = 1$. The dashed and dotted lines have been obtained with, respectively, $c = 1/2$ and $c = \infty$. These results show that the BAO reconstruction method presented in this work is very robust against changes in the UV.

which can be used to extract cosmological information. Thanks to our procedure to extract the oscillating part of the PS, one can discuss the same issue in Fourier space and show that the damping of the oscillatory component of the PS depends, in practice, only on the Ξ function defined in eq. (3.29), and therefore carries information on the linear PS and the linear growth factor. These IR effects are orthogonal to the well known limitations of SPT in the UV, which are quantitatively taken into account by effective "sound speed", and other counterterms, which we have shown to be basically irrelevant on the BAO evolution. As a result, the BAO oscillations are robustly reproduced at all scales and at all redshifts by means of the semi-analytical computation presented here, which requires only the 1-dimensional momentum integral defining the Ξ function.

When extracting BAO from data one usually fits the total PS with a model containing a certain number of nuisance parameters (see, for instance, [49]). The BAO extractor introduced in (3.36), (3.37), contains no free parameters (Δ, n and r_s define an extraction procedure, they are not parameters to be fitted to compare theory and simulations or data. The parameter r_s controls the range over which the integral in the extractor is performed. The procedure is weakly sensitive to the specific choice of r_s, so even if it does not match the scale r_{bao} of the oscillations in the data exactly, the position of the peaks in the extracted PS will not be affected (see Fig. 3.5). Moreover, since the ratio R depends on ratios of PS measured at nearby scales, it should be insensitive to most of the systematics (including bias): this will be explored in the following chapter, where also the extension to redshift space will be investigated. The procedure can be equally applied to the reconstructed PS, obtained after the long range displacements have been undone [24, 50, 51, 52]: therefore it is not an alternative to reconstruction, but rather, it provides a parameter independent procedure to extract BAO information from reconstructed data.

As for the broadband part of the PS, we showed that a 1-loop SPT computation supplemented with just one UV counterterm gives results in agreement with N-body simulations up to $k_{max} \sim 0.4$ h/Mpc for $z \geq 0.5$, rapidly degrading at lower redshifts. We have discussed how to systematically improve our approximation, by including higher order SPT corrections and more correlators between the UV sources and the density and velocity fields. The use of time-evolution equations considered here is particularly fit to deal with models beyond ΛCDM in which the broadband part of the PS carries a distinctive signature, like cosmologies with massive neutrinos or based on

modified GR, as the scale-dependence of the growth factor can be directly implemented in the linear evolution matrix in eq. (3.3).

Chapter 4

Robustness of the Extracted PS against RSD and halo bias: Test with N-body simulations

The aim of this chapter is to further test the performance and robustness of the Extractor operator. We have already seen that the Extracted PS is mostly insensitive to the details of nonlinear dynamics at small scales. We then move to test it against the other two great challenges for an accurate PS model: Redshift Space Distortions and halo bias. We'll begin by redefine the Extractor operator and its error for an application to binned PS data where the different bins may be correlated to each other. This will prove to be especially useful when we will apply the pipeline described in this chapter to the experimental data.

This work has been published on the Journal of Cosmology and Astrophysics (JCAP 1801 (2018) no.01, 035). [1]

4.1 BAO extractor: definition

For any given power spectrum $P(k)$ we define

$$R[P](k;\Delta,\,n) \equiv \frac{\int_{-\Delta}^{\Delta} dx\, x^{2n}\left(1-\frac{P(k-x\,k_s)}{P(k)}\right)}{\int_{-\Delta}^{\Delta} dx\, x^{2n}\left(1-\cos(2\pi x)\right)}\,, \tag{4.1}$$

[1] SISSA Medialab Srl. Reproduced with permission. All rights reserved

where the BAO wavenumber is given by $k_s \equiv 2\pi/r_s$, with r_s the comoving sound horizon, computed using, for the assumed cosmological model, eq. (6) of [47]. In this expression we integrate around each value of the comoving momentum k in an interval given by twice the "range" parameter Δ times the BAO wavenumber.

The operation (3.36) is similar to the *moving average method*, common in other fields to discern smooth back-ground and rapid oscillations, and has the effect of "extracting" the oscillating part of the PS from the smooth one. In [53] we showed how the oscillating PS projected out in this way to a large extent evolves independently under nonlinear effects.

We also verified that the operation $R\,[P]$, once applied to theoretical power spectra, is very weakly dependent on the parameter n. This parameter might be relevant in analyzing real data, in the case in which the experimental error varies significantly within each interval $[k - k_{bao}\,\Delta, k + k_{bao}\,\Delta]$, where the meaning of k_{bao} is illustrated below. In the analyses performed in this work we fix $n = 0$ and will indicate $R[P](k; \Delta, n = 0)$ with $R[P](k; \Delta)$.

LSS power spectra comprise of a smooth broadband ("no-wiggle") component, plus a smaller ("wiggly") component due to the BAO oscillations,

$$P\,(k) = P^{nw}\,(k) + P^{w}\,(k) \simeq P^{nw}(k)\,[1 + A(k)\sin(k\,r_{bao})]\ , \tag{4.2}$$

where $A\,(k)$ is a smooth modulating function which damps the oscillations beyond the Silk scale. While r_s is the BAO scale of the assumed (reference) cosmological model, which is needed to define the extractor (eq. (3.36)) and the various theoretical formula, as for example, eq. (4.12), r_{bao} is the true scale of the BAO oscillations in data. Different computational techniques reproduce the $P^{nw}\,(k)$ with different accuracy, and for instance a percent accuracy at $k \gtrsim \mathrm{O}\,(0.1\,\mathrm{h/Mpc})$ requires going beyond standard perturbation theory, and accounting for UV effects through methods such as Coarse Grained Perturbation Theory [39, 40] or the Effective Field Theory of LSS [36, 37].

Inserting (4.2) in (3.36) for $k_s\,\Delta \ll k$ gives [53]

$$R[P](k; \Delta) = I\left(\frac{r_{bao}}{r_s}; \Delta\right)\frac{P^{w}(k)}{P(k)}\ + O\left(1/\left(k\,r_s\right)^2\right)\ , \tag{4.3}$$

where the scale independent quantity $I(\beta; \Delta, n)$ is given by

$$I\,(\beta; \Delta) \equiv \frac{\int_{-\Delta}^{\Delta} dx\ (1 - \cos\,(2\pi\,\beta\,x))}{\int_{-\Delta}^{\Delta} dx\ (1 - \cos(2\pi x))}\,, \tag{4.4}$$

and $I\left(1;\Delta\right)=1$. Notice that the quantity k_s (and therefore r_s) enters only to set the appropriate units of the interval over which the integral in (3.36) has to be taken. It does not affect the scale of the oscillations of $R[P]$ such as those in Fig. 4.1, which is given by the r_{bao} contained in $P^w(k)$ (see eq. (4.2)). Choosing $r_s \neq r_{bao}$ only affects – typically very mildly– the amplitude of the oscillations (see Fig. 4 of [53]).

As shown in this chapter and in the previous one, the scale of the oscillation that emerges from $R\left[P\right]$, is very weakly sensitive to the details of the smooth $P^{nw}\left(k\right)$ component. This allows to extract the BAO scale from the data, and to compare it with theory, in a way which is very insensitive to the UV physics. Details on how this comparison is performed are given below, see eq. (4.9).

The expression (3.36) is suitable for an input continuous power spectrum as given by theory. Assume we have instead binned data with momentum / PS value / error on the PS given by $\{k_n,\, P_n,\, \Delta P_n\}$. From the data we can construct the estimator

$$\hat{R}[P](k_m;\Delta) \equiv \frac{\sum_{l=-L_m(\Delta)}^{L_m(\Delta)} \left(1-\frac{P_{m+l}}{P_m}\right)}{\sum_{l=-L_m(\Delta)}^{L_m(\Delta)} \left[1-\cos\left(r_s\left(k_{m+l}-k_m\right)\right)\right]}\,, \tag{4.5}$$

where the value of the maximum $|l|$ in the sum, $L_m\left(\Delta\right)$, is chosen such that

$$|k_{m+l}-k_m| \leq k_s\,\Delta \quad \text{for} \;\; |l| \leq L_m\left(\Delta\right)\,. \tag{4.6}$$

Under the assumption of uncorrelated errors for the PS across different bins, the covariance matrix of the estimator is given by

$$\begin{aligned} C_{n,m}(\Delta) &\equiv \langle \hat{R}[P](k_n;\Delta)\hat{R}[P](k_m;\Delta)\rangle - \langle \hat{R}[P](k_n;\Delta)\rangle\langle \hat{R}[P](k_m;\Delta)\rangle \\ &= D_m^{-1}D_n^{-1} \sum_{l=-L_m(\Delta)}^{L_m(\Delta)} \sum_{l'=-L_n(\Delta)}^{L_n(\Delta)} \frac{P_{m+l}P_{n+l'}}{P_mP_n}\left(\frac{\mathrm{cov}^P_{m,n}}{P_mP_n}+\frac{\mathrm{cov}^P_{m+l,n+l'}}{P_{m+l}P_{n+l'}}\right. \\ &\qquad \left. -\frac{\mathrm{cov}^P_{m+l,n}}{P_{m+l}P_n}-\frac{\mathrm{cov}^P_{m,n+l'}}{P_mP_{n+l'}}\right), \end{aligned} \tag{4.7}$$

where

$$D_n \equiv \sum_{i=-L_n(\Delta)}^{L_n(\Delta)} \left(1-\cos\left(r_s\left(k_{n+i}-k_n\right)\right)\right)\,, \tag{4.8}$$

and cov^P_{mn} is the covariance matrix for the PS.

In the rest of this chapter, when considering different PS's P_a, we will plot the subtracted quantities $\hat{R}[P_a] - \hat{R}[P^{0,nw}]$, where $\hat{R}[P^{0,nw}]$ obtained by applying the procedure (3.37) to the smooth linear PS $P^{0,nw}$, defined as explained in C. This subtraction largely removes the smooth $O(1/(kr_s^2))$ contribution to eq. (4.3). However, in our numerical analyses, we always consider the unsubtracted $\hat{R}[P_a]$'s. Moreover, in the following, we will indicate the estimator $\hat{R}[P_a](k_m;\Delta)$ simply as $R[P_a](k;\Delta)$.

We plot in Fig. 4.1 the result of the extraction procedure applied to different approximations of the DM PS in the BAO range of scales, namely, linear theory, 1-loop SPT, improvements to 1-loop SPT discussed in the next two sections, and N-body simulations. This plot will be further discussed in subs. 4.3.1.

Besides damping the oscillations with respect to linear theory, nonlinearities also modify the BAO scale, an effect which can crucially hinder the possibility of using BAO's as a cosmic ruler [54] (although, as we mentioned before, this effect can be reduced by reconstruction techniques). In order to quantify this effect we define a likelihood function as

$$\chi^2_a(\alpha) = \sum_{n,m=n_{min}}^{n_{max}} \delta R[P_a](k_n;\alpha,\Delta) C^{-1}_{n,m}(\Delta) \delta R[P_a](k_m;\alpha,\Delta)\,, \tag{4.9}$$

where

$$\delta R[P_a](k_n;\alpha,\Delta) \equiv R[P_a](k_n/\alpha;\Delta) - R[P_{data}](k_n;\Delta)\,, \tag{4.10}$$

P_a the model PS as obtained in a given approximation, while P_{data} is the measured one, and $C^{-1}_{n,m}(\Delta)$ is the inverse of the matrix given in eq. (4.7), computed using the experimental errors on the data PS. The sum is taken over the momenta k_n in which there are BAO oscillations (see Fig. 4.1), typically in the range

$$0.025\ \ \mathrm{h\,Mpc^{-1}} \lesssim k_n \lesssim 0.3\ \ \mathrm{h\,Mpc^{-1}}\,, \tag{4.11}$$

where the upper end is limited by the goodness of the $\chi^2_a(\alpha)$ value, and therefore varies for the different models/approximations. For those models providing a good fit up to higher momenta, the $\chi^2_a(\alpha)$ curve is narrower and therefore gives tighter constraints on the extracted BAO scale.

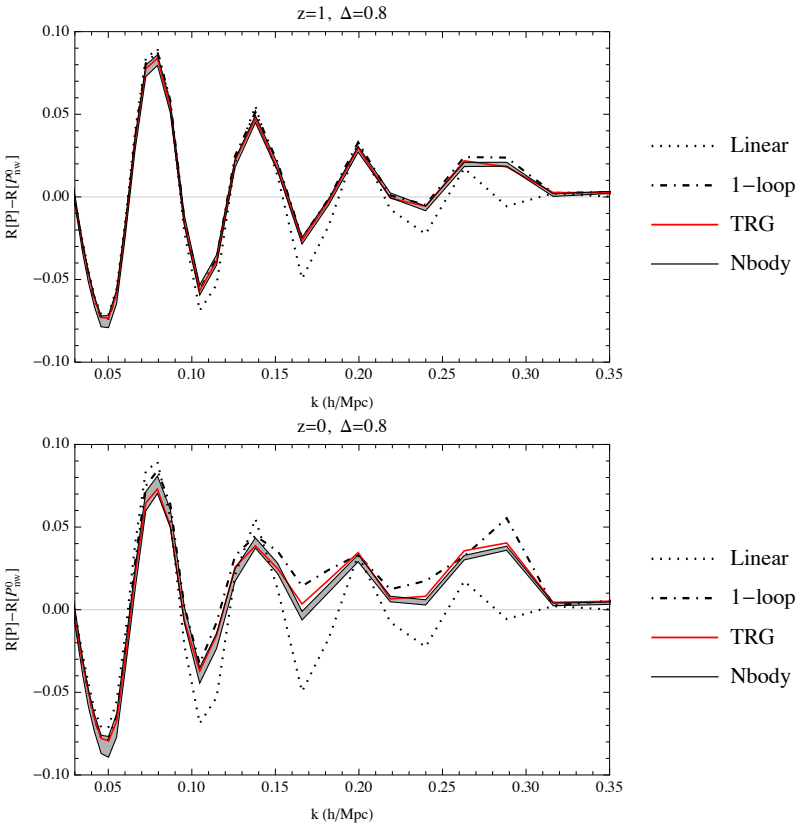

Figure 4.1: The extractor $R[P](k;\Delta)$ applied to the DM PS in real space computed from N-body simulations (grey area), from linear theory (dotted), 1-loop SPT (black, dash-dotted), and TRG (red, obtained from eq. (4.23)), at redshift $z = 1$ (upper panel) and at $z = 0$ (lower panel). The grey area for the N-body results corresponds to the diagonal entries of eq. (4.7) and using the 1σ error on the PS for each bin. For visualisation purposes, the same quantity $R[P^{0,nw}](k)$, where $P^{0,nw}$ is the smooth component of the linear PS, has been subtracted from all the different $R[P](k)$.

In the following, we use the diagonal entries of the covariance matrix for the extractor, eq. (4.7), to indicate the 1σ errors on the extracted $R[P]$ functions in plots such as those in Fig. (4.1), while we use the full matrix to evaluate the various $\chi^2_a(\alpha)$. As for the covariance matrix for the PS from N-body simulations, $\mathrm{cov}^P_{m,n}$, we will estimate its diagonal terms from the scattering of $|\delta_{\mathbf{k}}|^2$ with $\mathbf{k}$'s inside each k bin, while we will neglect the nondiagonal terms. In Appendix F we will investigate the impact of the non-diagonal terms on our analyses, showing that they are negligible.

4.2 A simple model for the extraction of the BAO scale

In this section we present a simple procedure to extract the BAO scale from a given P_{data}. We will use, as data, the halo PS in redshift space (see Appendix E for technical details on our simulations and halo catalogs). The impact of the different types of nonlinear effects on $R[P]$, and the performance of different approximation methods in dealing with them will be discussed in the next sections.

Our model PS is given by

$$P_{model}(k,\mu;A) = e^{-Ak^2} P_{res}(k,\mu)\,, \tag{4.12}$$

with

$$\begin{aligned} P_{res}(k,\mu) = {} & P^{nw,rs,0}(k,\mu) + \Delta P^{nw,rs,1-loop}(k,\mu) \\ & + P^{w,rs,0}(k,\mu)\, e^{-k^2 \Xi^{rs}(\mu;r_s)}\,, \end{aligned} \tag{4.13}$$

where $P^{nw,rs,0}(k,\mu)$ and $P^{w,rs,0}(k,\mu)$ are the smooth and "wiggly" components of the linear PS for DM in redshift space, calculated in the Kaiser approximation, namely,

$$P^{a,rs,0}(k,\mu) = (1+\mu^2 f)^2 P^{a,0}(k)\,, \tag{4.14}$$

with $a = w, nw$. The 1-loop correction in the improved Kaiser approximation is given by

$$\begin{aligned} \Delta P^{nw,rs,1-loop}(k,\mu) = {} & \Delta P^{nw,1-loop}_{\delta\delta}(k) + 2\mu^2 f \Delta P^{nw,1-loop}_{\delta\theta}(k) \\ & + \mu^4 f^2 \Delta P^{nw,1-loop}_{\theta\theta}(k)\,, \end{aligned} \tag{4.15}$$

with $\Delta P^{nw,1-loop}_{\delta\delta}(k)$, etc, the different components of the real space 1-loop PS [55] for the density contrast δ or the velocity divergence θ computed from the linear smooth one.

The resummation of the effect of IR random velocity flows at all orders in SPT is implemented by exponentiating

$$\Xi^{rs}(\mu; r_s) = \left(1 + f\mu^2(2+f)\right)\Xi(r_s) \\ + f\mu^2(\mu^2-1)\frac{1}{2\pi^2}\int dq\, P^{nw,0}(q) j_2(qr_s)\,, \quad (4.16)$$

with

$$\Xi(r_s) \equiv \frac{1}{6\pi^2}\int dq\, P^{nw,0}(q;z)\,(1 - j_0(q\,r_s) + 2j_2(q\,r_s))\,, \quad (4.17)$$

see Appendix C and the previous chapter, where the details of the resummation procedure are discussed.

Multipoles can be computed from $P_{res}(k,\mu)$ as usual, by taking the integrals

$$P_{model,l}(k;A) \equiv \frac{2l+1}{2}\int_{-1}^{1} d\mu\; P_{model}(k,\mu;A)\,\mathcal{P}_l(\mu)\,, \quad (4.18)$$

where $\mathcal{P}_l(\mu)$ is the Legendre polynomial of order l. In what follows we will only consider the monopole ($l = 0$).

The only free parameter in eq. (4.12) is the constant A at the exponent, which, as we will see, can be treated as a nuisance parameter to marginalize over the scale dependence of halo bias and on redshift space effects not captured by the (improved) Kaiser approximation encoded in $P_{res}(k,\mu)$, such as FoG. In [56, 57, 58], a scale-dependent halo bias given by a constant plus a quadratic term in k was predicted by the peaks model, which can be seen as a truncated Taylor expansion of the model used here. Notice that since the definition of $R[P]$, eq. (3.37), is insensitive to the PS normalization, a constant and linear bias parameter would drop off the analysis, so when studying halos we do not need to introduce it. Moreover, in order to fully capture the unaccounted redshift effects such as FoG, a μ-dependent function should be introduced (FoG should scale as something like $\exp(-f^2\sigma_v^2 k^2\mu^2)$), see for instance [59]. However, in this paper we only consider the monopole, therefore we decided to minimise the number of extra functions and incorporate both bias and RSD in the single parameter A.

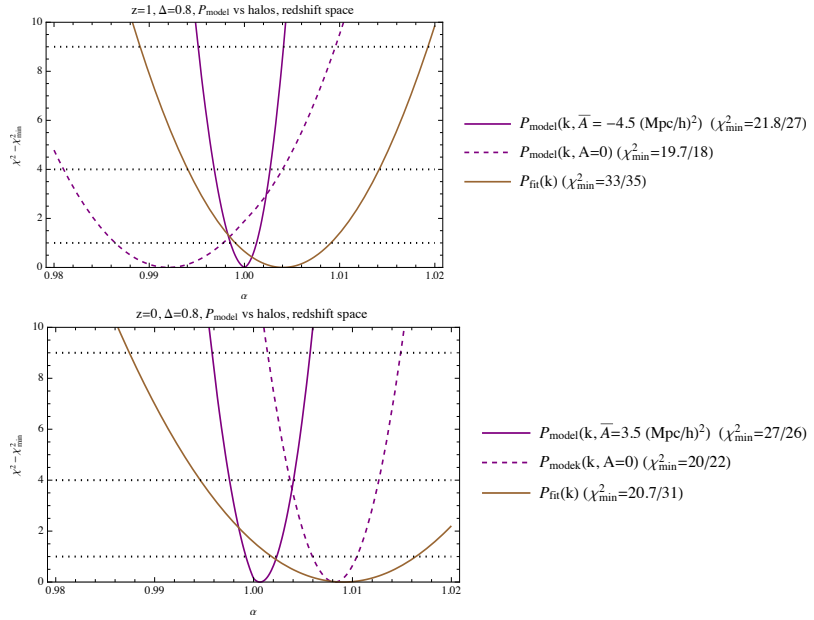

Figure 4.2: The function χ^2 defined in (4.9) as a function of the shift parameter α with respect to halo data using $P_{model,0}(k;A)$ as a model. Each curve has been shifted vertically so to be vanishing at its minimum. The effect of removing the free parameter A is shown by the comparison of the purple solid and dashed lines.

To fix A we use the full monopole power spectra $P_{model,0}$ and $P_{halo,0}$. We take the ratios between the two, and look for the value $\bar{A}$ which minimizes its scale dependence at low k's. Then we compute (4.9) as a function of the parameter α with $P_a = P_{model,0}(k, \bar{A})$ and $P_{data} = P_{halo,0}(k)$. The result is shown in Fig. 4.2, where we show the function $\chi^2(\alpha) - \chi^2(\alpha_{min})$ obtained by this procedure. We also show the effect of removing the parameter A by setting it to zero in (4.12). As we see, the simple model considered here captures the correct BAO scale at better than the 0.1% level both at $z = 0$ and at $z = 1$, moreover the 1σ confidence level corresponds to 0.16 % (0.14 %) at $z = 0$ ($z = 1$). Setting the exponential prefactor to unity ($A = 0$), still reproduces the BAO scale at subpercent level, but with a reduced precision, especially at $z = 1$, where the effect of halo bias is larger, see Sect. 4.3.3.

For comparison, we also plot (brown solid line) the χ^2 obtained by a different procedure, which resembles more closely the standard one employed, for instance, in [49]. In this case, the model PS is fit directly to the full P_{data} PS, instead of considering the $R[P]$ operation, therefore, more parameters are needed to model the broadband feature. Following [49], we consider a model PS given by the 8−parameter function:

$$P_{\rm fit}\left(k;\alpha\right) = P^{\rm smooth}\left(k\right)\left\{1+\left[O^{\rm linear}\left(\frac{k}{\alpha}\right)-1\right]e^{-\frac{k^2\Sigma_{\rm nl}^2}{2}}\right\}\ , \tag{4.19}$$

where the oscillatory component is obtained from the ratio between the total linear and smooth linear power spectrum[2]

$$O^{\rm linear}\left(k\right) \equiv \frac{P^0\left(k\right)}{P^{0,nw}\left(k\right)}\,, \tag{4.20}$$

while the smooth component is given by

$$P_{\rm smooth}\left(k\right) \equiv B_P^2 P^{0,nw}\left(k\right) + A_1\, k + A_2 + \frac{A_3}{k} + \frac{A_4}{k^2} + \frac{A_5}{k^3}\,, \tag{4.21}$$

where the parameters $A_{1,\cdots,5}$ and B_P marginalise over broad-band effects including redshift-space distortions and scale-dependent bias. Notice that, unlike our Ξ function of eq. (5.6), now also the exponential damping containing $\Sigma_{\rm nl}$ in (4.19) is treated as a nuisance parameter. To quantify the precision with which this procedure can reproduce the BAO scale, we fit P_{halo} with

[2]In [49] the smooth PS is derived using the fitting formula of [60] instead of the procedure described in C. This difference does not change things appreciably.

the expression (4.19), fixing $\alpha = 1$ and finding the best fit values for the remaining 7 parameters $\{\Sigma_{\rm nl},\, B_P,\, A_1,\, A_2,\, A_3,\, A_4,\, A_5\}$. With these values fixed [3], we then compute the likelihood

$$\chi^2_{fit}(\alpha) = \sum_n \frac{\left(P_{\rm fit}(k_n,\alpha) - P_{\rm halo}(k_n)\right)^2}{\left(\Delta P_{\rm halo}(k_n)\right)^2}\,, \tag{4.22}$$

as a function of α.

As seen from the figure, both methods are able to return the BAO scale at the subpercent level, as a best fit and are in mutual agreement within $1\,\sigma$. The advantage of the $R[P]$ method appears when looking at the width of the likelihood intervals, which, for these "data", is reduced with respect to the method based on (4.19): it gives a 1σ error on α of $0.16\,\%$ ($0.14\,\%$) at $z = 0$ ($z = 1$) against $1.4\,\%$ ($1\,\%$) by the "standard" procedure.

4.3 Nonlinear effects on $R[P]$

In this section we discuss the sensitivity of the function $R\,[P]\,(k;\Delta)$ to various nonlinear effects.

4.3.1 Nonlinear evolution of the DM field

Assuming that N-body simulations fully account for DM nonlinearities on the scales of interest for this paper, we discuss how different approximations affect the $R[P]$ operation and the extraction of the BAO scale from it. Besides linear theory and 1-loop SPT, we will consider the TRG result of [53], which can be cast, in real space, in the form

$$P^{TRG}(k) = P_{model}(k;\mu=0,A=0) + \Delta P^{nw,TRG}(k)\,, \tag{4.23}$$

where P_{model} has been defined in (4.12). $\Delta P^{nw,TRG}(k) \equiv D(z)^2 \Delta P^{nw}_{11}(k;\eta)$ is the UV correction ($\eta \equiv \log D(z)$, ($D(0) = 1$)), where $\Delta P^{nw}_{11}(k;\eta)$ solves the TRG system discussed in [53], which encodes the difference between the correct UV behavior, extracted from simulations, and the one of 1-loop SPT

[3] We checked that the procedure is converging, in the sense that by fixing the initial α to a slightly different ($\pm 1\%$) value and extracting the corresponding parameters gives very similar χ^2 curves.

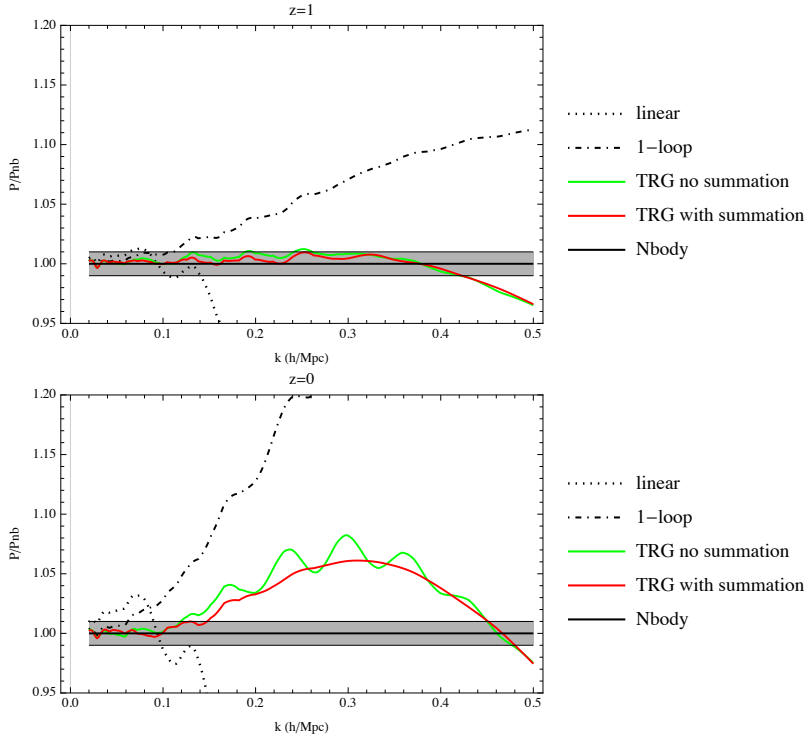

Figure 4.3: Ratios of the nonlinear PS obtained with the different approximations described in the text after eq. (4.23) to the N-body ones.

added (see Appendix refappendicetrg for a discussion, and ref. [53] for full details).

To see how well the nonlinear broadband shape of the PS is reproduced, in Fig. 4.3 we plot the ratios of the different approximations to N-body simulations.

In comparison with 1-loop SPT, the UV effects encoded in the TRG corrections increase the k-range in which the results agree to better than 1 % with simulations from $k \sim 0.06$ (0.1) h^{-1} Mpc to $k \sim 0.14$ (0.42) h^{-1} Mpc at $z = 0$ ($z = 1$). On the other hand, the effect of the resummation of the random motions is seen by comparing the red and the green lines, which are obtained by setting $\Xi^{rs}(0; r_s) = 0$ in (4.23), and by replacing $\Delta P^{nw,1-loop}(k)$ with the full 1-loop correction, $\Delta P^{1-loop}(k)$.

To focus the discussion on the BAO's, we plot in Fig. 4.1, the result of the extraction procedure applied to the different approximations discussed

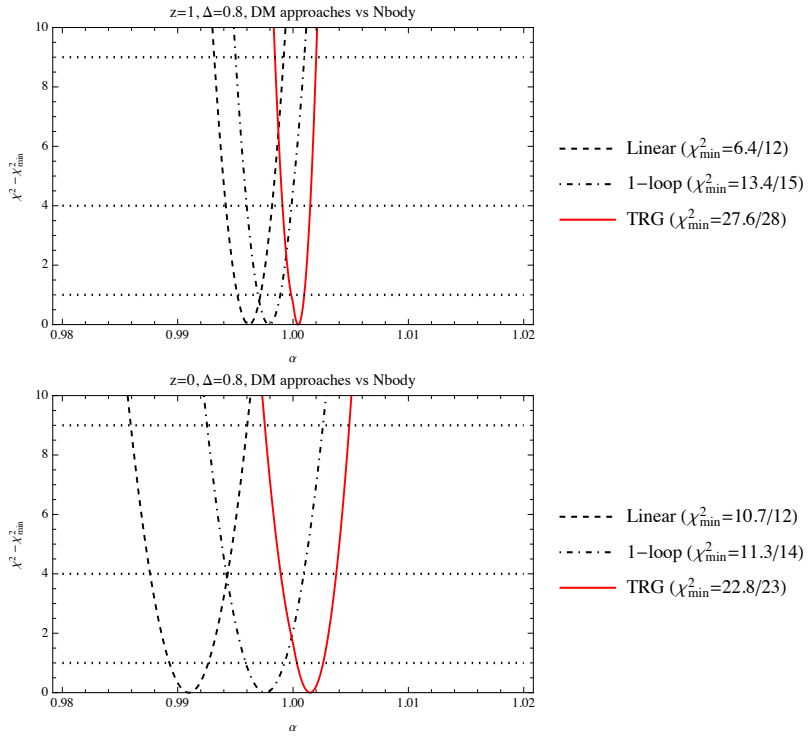

Figure 4.4: The function χ^2 defined in (4.9) as a function of the shift parameter α with respect to N-body data for different approximation to the DM PS. Each curve has been shifted vertically so to be vanishing at its minimum.

above. For all the approaches we have used the same binning in k, and the grey band corresponds to the estimated 1σ statistical error on the N-body PS, evaluated using the diagonal entries of eq. (4.7). We see that the TRG approach reproduces the BAO damping quite well over the full range of wavenumbers.

To quantify the effect of the nonlinear DM evolution on the BAO scale we define a likelihood function, in analogy to (4.9), in which the role of P_{data} is played by the N-body DM PS, and the covariance matrix is obtained from the statistical errors on the N-body PS , while P_a is obtained in linear theory, 1-loop SPT, and in the TRG approach.

The results are plot in Fig. 4.4. The nonlinearities encoded in the N-body simulations shift the BAO scale towards smaller scales by $\sim 0.8\%\,(0.4\,\%)$ at

$z = 0$ ($z = 1$) with respect to the linear theory PS [4]. The 1-loop SPT approximation, on the other hand, gives a much better fit both at $z = 0$ and at $z = 1$, mainly thanks to the fact that it reproduces the lower peaks well. It is a remarkable result, as the 1-loop approximation is generally considered a poor tool for the description of the nonlinear PS in the BAO range of scales. This is of course true, but is mainly related to the broadband part of the PS. As far as the oscillating component extracted by the $R\,[P]$ procedure is concerned, the 1-loop result performs very well. This is fully in line with the previous study by Ref. [62], where it was shown that the BAO scale is robust against the 1-loop SPT correction when the smooth broadband is removed appropriately. We will see, however, that it is not the case in redshift space.

On the other hand, the TRG result (red lines) reproduces the nonlinear shift at better than 0.2 % level both at $z = 0$ and than 0.1 % at $z = 1$. Given that the computational cost for this approach is the same needed for the 1-loop PS, the gain represented by it at low redshifts is clear.

4.3.2 Redshift space distortions

The effect of redshift space distortions on the extracted BAO is given in Fig. 4.5, where we plot the results for the DM field as obtained in N-body simulations both in real and in redshift space (in the latter case we consider the monopole PS). The effect on the extracted α parameter is given in Fig. 4.6, where we have used again eq. (4.9), with P_a being the monopole PS in redshift space and P_{data} the N-body PS in real space. In other words, we try to fit the real space $R[P]$ from the redshift space one. As a result, the extracted BAO scale is rescaled by $\sim 0.5\,\%$, at $z = 1$ and by $\sim 0.7\%$ at $z = 0$, but the fit rapidly gets poorer by including higher wavenumbers. The question is whether one can improve this extraction by applying the TRG approach to redshift space.

The extension of eq. (4.23) to redshift space is (see Appendix D)

$$P^{TRG,rs}(k,\mu) = P_{model}(k;\mu, A = 0) + \Delta P^{nw,rs,TRG}(k,\mu)\,, \tag{4.24}$$

[4] To get an analytic insight on this effect see [54]. Reconstruction techniques are also able to remove the BAO shift, see for instance [61].

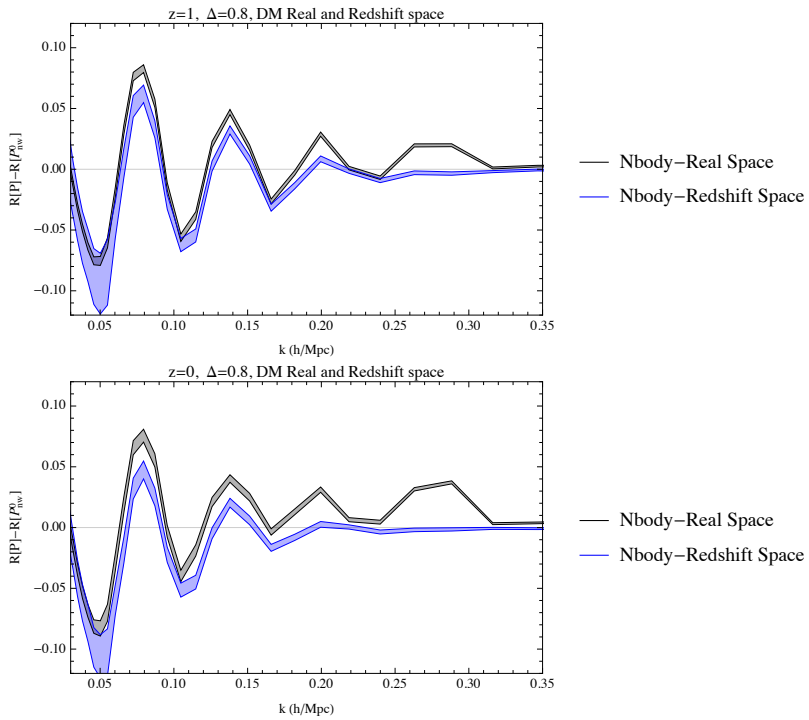

Figure 4.5: Comparison between the $R[P]$'s for the Nbody PS in real and in redshift space (monopole) at $z = 1$ and at $z = 0$.

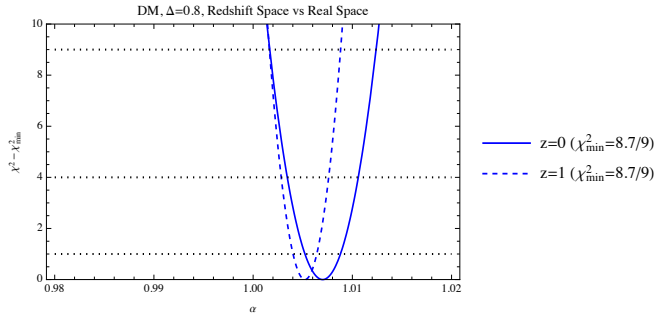

Figure 4.6: χ^2 of the shift α between the real and redshift space PS for DM from N-body simulations.

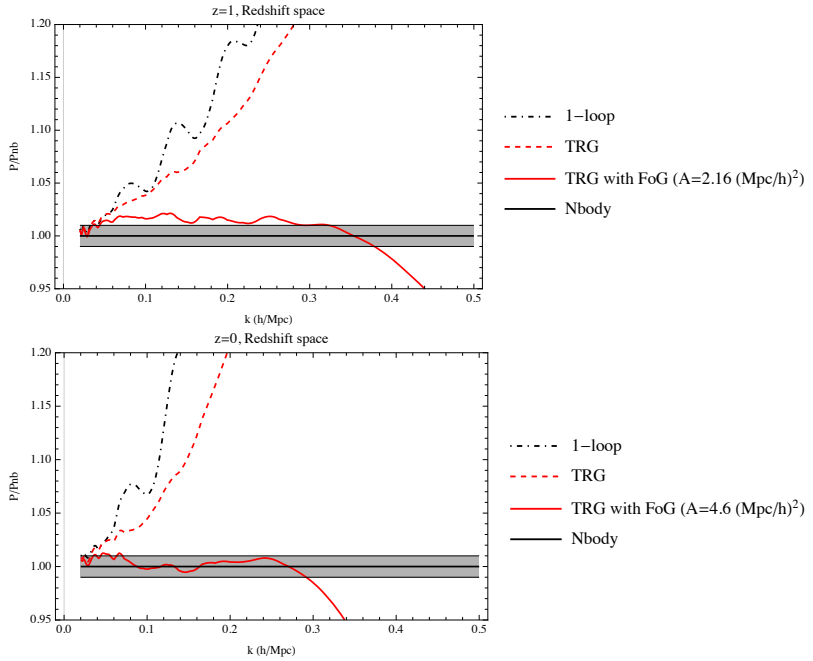

Figure 4.7: Ratios of the nonlinear (monopole) PS in redshift space obtained with the different approximations described in the text at $z = 1$ and at $z = 0$.

where

$$\Delta P^{nw,rs,TRG}(k,\mu) = D(z)^2\Big[\Delta P_{11}^{nw,TRG}(k,\mu;\eta) + 2\mu^2 f \Delta P_{12}^{nw,TRG}(k,\mu;\eta) + \mu^4 f^2 \Delta P_{22}^{nw,TRG}(k,\mu;\eta)\Big]\,, \tag{4.25}$$

where $\Delta P_{ab}^{nw,TRG}$ $(a,b = 1,2)$ are, again, computed using the TRG equations of [53].

The performance of eq. (4.24) in reproducing the broadband shape of the nonlinear PS in redshift space is much worse than for its real space counterpart, as we can see comparing the red dashed lines of Fig. 4.7 to the red solid ones in Fig. 4.3. It still improves somehow with respect to the 1-loop result, however, it deviates from the N-body result by more than one percent already for $k \gtrsim 0.05\,\mathrm{h\,Mpc^{-1}}$. The reason for the poor performance of eq. (4.24), is the absence of any term accounting for the so-called FoG effect. It can be included in a purely phenomenological way by multiplying the full eq. (4.24) by a scale-dependent function, which in this case we take

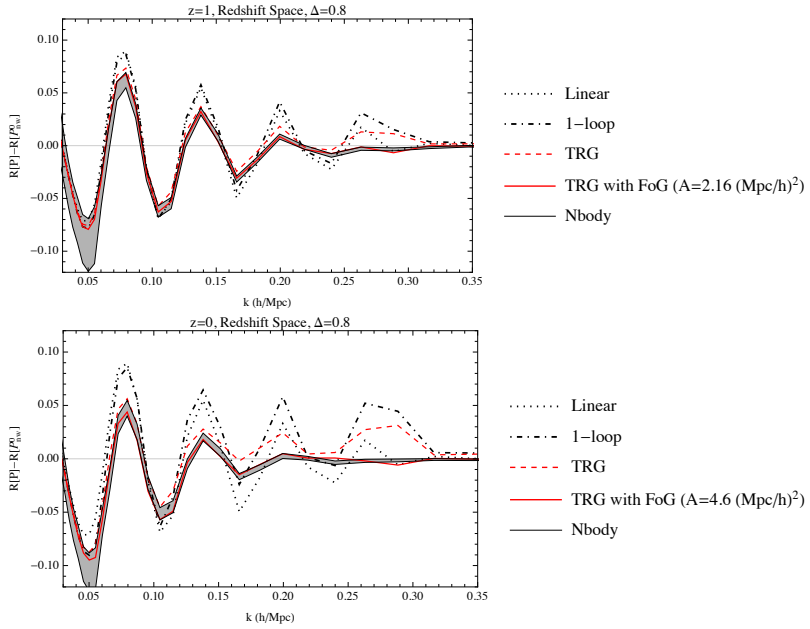

Figure 4.8: The extractor $R[P](k;\Delta)$ applied to the redshift space monopole PS computed from N-body simulations (grey area), from linear theory (blue, dashed), 1-loop SPT (black, dash-dotted), TRG (red), and "TRG+FoG corrections" (orange), as described in the text, at redshift $z = 1$ and at $z = 0$. The grey area for the N-body results corresponds to the error computed using eq. (4.7) and using the 1-σ error on the PS for each bin. For visualisation purposes, the same quantity $R[P^{0,nw}](k)$, where $P^{0,nw}$ is the smooth component of the linear PS, has been subtracted from all the different $R[P](k)$.

of the exponential form, e^{-Ak^2}. Notice that, in general, the FoG modelling depends on the line of sight direction, μ, however, since we are considering only the monopole, we just restrict ourselves to a purely phenomenological, scale dependent, function. In this case the fit on the full PS clearly improves, as illustrated by the red solid lines in Fig. 4.7.

As far as BAO's are concerned, the FoG-corrected TRG gives a very good fit to the N-body $R[P]$ over all the relevant range of scales, while the TRG without FoG correction clearly performs better than linear theory and 1-loop SPT, at least for the lower peaks, see Fig. 4.8. To be more quantitative, we define a new likelihood function, analogous to eq. (4.9), in which the role of P_{data} is taken by the redshift space (monopole) PS from N-body simulations.

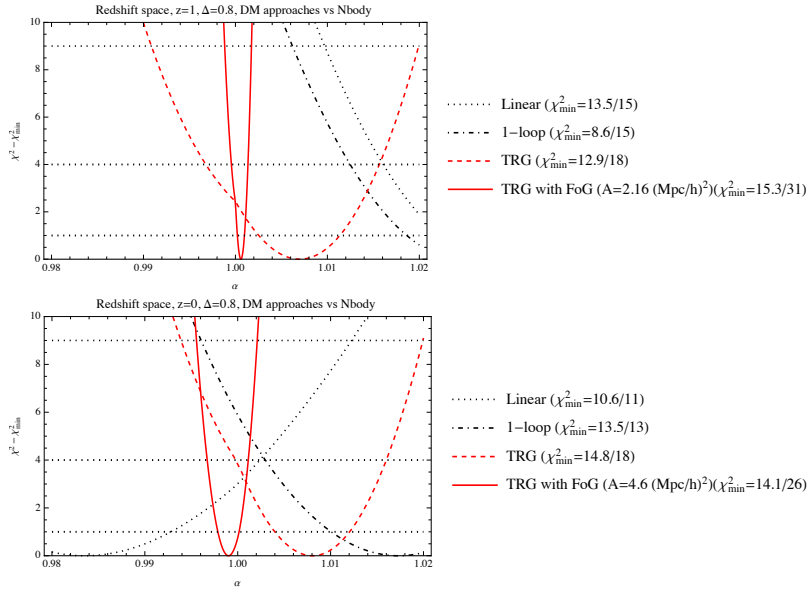

Figure 4.9: χ^2 as a function of the shift parameter α for different DM approaches vs N-body in redshift space.

As we see from Fig. 4.9, the inclusion of the FoG correction on the TRG result reproduces the N-body BAO scale at the 0.1% level, in line with its real space counterparts (see Fig. (4.4)), while without FoG correction it still performs at better than the percent level.

4.3.3 Halo bias

We now study the effect of halo bias on the function $R[P]$. We focus our discussion on halos of mass $M > 10^{13}\,M_\odot$ identified in the N-body simulations described in Appendix E, where we also plot the bias, that is the ratio between the halo and DM PS's, for the complete halo catalog and for its partition in different mass bins, see Fig. E.1. We also list, in Tab. E.2, best fit values for a model bias function given by $P_{halo}(k) = (b_0 + b_1 k^2)^2 P_{Nbody}(k)$. As the $R[P]$ operation is insensitive to a constant bias, we consider in this section, as we did in Sect. 4.2, a single parameter model for the halo, again of the exponential form, e^{-Ak^2}. More refined models can of course be tested but as we will see, this one already provides a very good fit.

The different PS give the $R[P]$'s plotted in Fig. 4.10. The green band

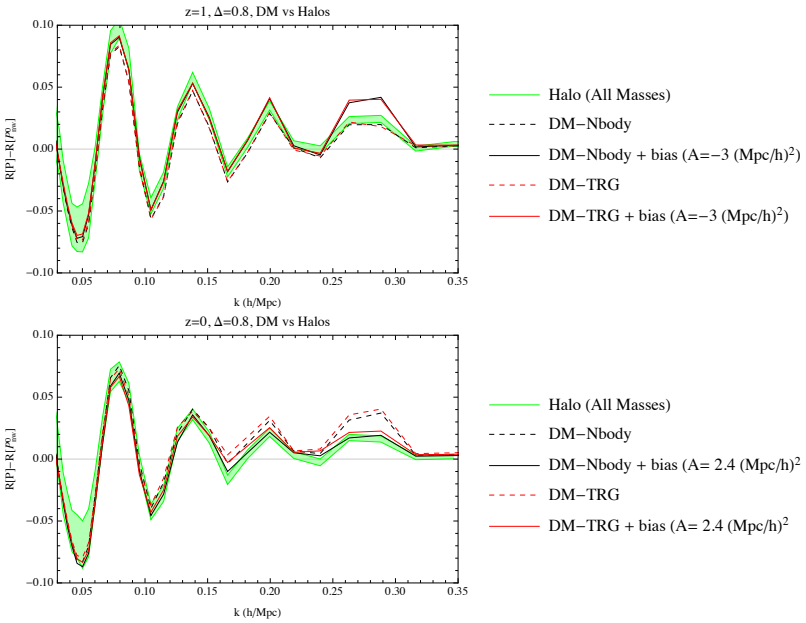

Figure 4.10: The extractor $R[P](k;\Delta)$ applied to the PS of all halos with mass $> 10^{13}\,M_\odot$ (green band). The black dashd lines are obtained from the DM PS from N-body simulations, while the red dashed lines are obtained from the TRG. The corresponding solid lines are obtained by multiplying the PS by e^{-Ak^2}, with A fitted from the smooth component.

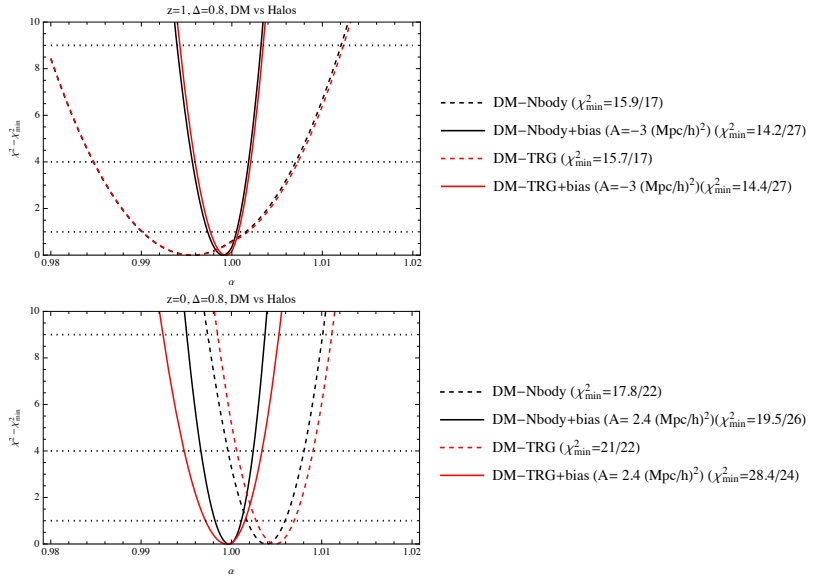

Figure 4.11: χ^2 as a function of the shift parameter α for DM (from N-body and TRG) vs. halos with $M > 10^{13}\, M_\odot$.

is obtained from the total N-Body halo PS, while the DM PS from N-body simulations is given by the black lines: the dashed ones are obtained from the unbiased PS, while the solid ones are from the one multiplied by e^{-Ak^2}, with A fit from the total halo PS bias. The red lines are obtained by the TRG approximation, again unbiased (dashed) and biased (solid).

Then, taking the halo PS (with the corresponding errors) as P_{data} in eq. (4.9), we study the shift in the BAO scale derived by modeling it using the different procedures. The results are given in Fig. 4.11. The dashed curves show that the effect of bias is $O(0.5\%)$ both at $z = 0$ and at $z = 1$, although opposite in sign. Notice, again, that what counts here is the scale dependence of the bias, which is in magnitude roughly the same at the two different redshifts. The bias can be entirely taken into account by our simple exponential function, and the TRG results practically coincide with the N-body ones. Similar results are obtained in redshift space, as one can infer also by looking at Fig. 4.2.

4.4 Conclusions

In this chapter we studied and further developed the estimator $R[P]$ introduced in the previous chapter to extract the BAO scale from a power spectrum P. We showed that the estimator is extremely robust against various physical effects. The estimator is mostly sensitive to the nonlinear evolution of the DM field, which causes a rescaling of the BAO scale of $\gtrsim 1\%$. Redshift space distortions beyond the (improved) Kaiser approximation and halo bias affect the $R[P]$ extraction only at the sub-percent level at all redshifts, as indicated, respectively, by Figures 4.6 and 4.11, and can be taken into account by simple fitting functions, such as the e^{-Ak^2} one considered here. Once the parameter A is fitted to the broadband shape of the PS measured from real data, the extraction of the BAO scale from the $R[P]$ projector is a parameter-free procedure.

We studied how the nonlinear evolution of the DM field can be taken into account in SPT and in the TRG approach described in [53], which improves over 1-loop SPT by including the effect of large scale motions and by correcting the short-scale behavior via the addition of effective coefficients, measured from numerical simulations. As seen in Figure 4.3, in comparison to 1-loop SPT, the short-scale corrections significantly improve the reproduction of the broadband shape of the PS, and are therefore relevant when the latter matters, as, for instance, in studying the effect of massive neutrinos [63, 64, 65] [5]. However, their impact on the BAO scale is greatly alleviated. This proves that the extraction of the BAO scale is to a large extent independent of UV effects, so that expensive simulations (required to either solve the dark matter dynamics, or to compute effective coefficients) are not needed. The main improvement of the TRG method over 1-loop SPT as far as BAO are concerned is in the resummation of the effect of large scale modes, which provides an accurate accounting of the oscillating structure of $R[P]$ over all scales and at all redshifts, see Fig. 4.1. The exponential damping term accounting for such effects in the TRG approach can be immediately computed with a 1-dimensional integral of the linear PS.

We compared our extraction procedure to the standard approach to the BAO scale measurements, which involves a multi-parameter fit to the full PS and makes use of fitting functions for the smooth linear PS. Beside having

[5] Further improvement is required to accurately reproduce the effects of the FoG in redshift space. Improving over the existing phenomenological approaches requires going beyond the single stream approximation.

considerably fewer parameters (or not at all), our approach, when applied to the halo catalog considered in this paper, reduces the error on the extracted scale by a factor ~ 4.7 (~ 3.6) at redshift $z = 0$ ($z = 1$), as shown in Figure 4.2.

In principle, the procedure can be applied to the *reconstructed* PS, obtained after the long range displacements have been undone [24, 61, 50, 51, 54, 52]: therefore it is not an alternative to reconstruction, but rather, it provides a parameter independent procedure to extract BAO information from reconstructed data. We plan to investigate this possibility in a forthcoming work.

In summary, the BAO extracting procedure outlined in Sect. 4.1, and the simple model introduced in Sect. 4.2 allow to compute the BAO scale at sub-percent accuracy, at all redshifts, including bias and redshift space distortions effects. This procedure is extremely fast, and no more computationally expensive than 1-loop (SPT). Moreover, contrary to the standard procedure, it does not require a multi-parameter fit of the data to account for the broadband shape of the PS, which is largely filtered out by the extractor.

Chapter 5

BAO Extractor: Application to BOSS DR12 experimental data

5.1 The BOSS data and reconstruction

The Baryon Oscillation Spectroscopic Survey (BOSS) was part of the effort of the SDSS-III collaboration to map our near Universe. It measured the spectroscopic redshift of luminous galaxies in the $0.2 < z < 0.75$ redshift range and two regions of the sky, denoted by North Galactic Cup (NGC) and South Galactic Cup (SGC), from which, respectively, about 865 000 and 330 000 galaxies were measured [20]. The measurements were made with a 2.5 metre-aperture telescope at the Apache Point Observatory, New Mexico, and covered about 10 000 square degrees. The data is publicly available and accessible through the SDSS-III website [66].

In our analysis we are interested in the PS, of which the BOSS collaboration measured the monopole, quadrupole, and hexadecapole moments. These were divided into 3 overlapping redshift bins: $0.2 < z < 0.5$, $0.4 < z < 0.6$ and $0.5 < z < 0.75$, for which the effective redshifts of $z_{eff} = 0.38$, 0.51 and 0.61 were used in our computations. The experimental data is accompanied by a set of mock galaxies, the MultiDark-Patchy mock catalogues [67, 68] whose primary purpose is to provide the covariance matrices, but can also be used to test the analysis pipeline.

Nonlinear dynamics damps the BAO signal which, if not properly accounted for, degrades to a large extent the information that can be extracted from the data. One approach is to properly model the damping using the

techniques we have presented in [53, 69]. Another approach is to act on the data itself using so called *reconstrution* techniques [24]. The aim of these techniques is to (partially) undo the bulk motions of galaxies, by moving them back to their original position, by reconstructing the velocity field from the density one, via the continuity equation. In linear perturbation theory the displacement Ψ is related to the redshift-space density field by [70]

$$\nabla \cdot \Psi(\mathbf{s}) + \beta \nabla \cdot (\Psi \cdot \hat{s}_{||}) \hat{s}_{||} = -\frac{\tilde{\delta}_{obs}(\mathbf{s})}{b} \,, \tag{5.1}$$

where b is the linear galaxy bias, $\hat{s}_{||}$ is the unit-vector along the line of sight, and $\beta = b/f$ (where f is the linear growth function). The density field $\tilde{\delta}_{obs}(\mathbf{s})$ is smoothed on a scale, which in the BOSS implementation of reconstruction [71] is taken to be $\Sigma_{sm} = 15\,\mathrm{h}^{-1}\mathrm{Mpc}$ using a gaussian filter

$$S(k) = \exp\left[-(k\Sigma_{sm})^2/2\right] . \tag{5.2}$$

Filtering the density to damp the nonlinearities at small scales is required in order to use of the linear continuity equation, eq. (5.1).

Assuming the displacement field is irrotational, the equation above can be solved, and the the line-of-sight and angular positions of the galaxies are shifted as follows

$$\begin{aligned} s_{||}^{\mathrm{new}} &= s_{||}^{\mathrm{old}} - (1+f)\Psi_{||}(\mathbf{s}^{\mathrm{old}}) \,, \\ s_{\perp}^{\mathrm{new}} &= s_{\perp}^{\mathrm{old}} - \Psi_{\perp}(\mathbf{s}^{\mathrm{old}}) \,, \end{aligned} \tag{5.3}$$

where the $(1+f)$ factor multiplying the displacement along the line of sight aims at removing the linear component of redshift-space distortions.

The same displacement procedure is applied to a set of randomly distributed particles. The reconstructed density field are then given by the difference between the displaced galaxy field and the displaced random field.

Therefore we have, for each multipole and each redshift bin, 2 pre- reconstruction PS's (from the NGC and SGC) and 2 post-reconstruction PS's. In the following we are going to apply the extractor analysis to these sets of data and compare the results with those obtained by the analysis performed by the BOSS collaboration using a 10-parameter fit for the model PS, both for the pre-reconstruction and post-reconstruction datasets.

5.2 The model

In [69] we tested the performance of a simple model function to reproduce the extracted PS obtained from N-Body simulations and found good agreement, both for matter and for halos, in real and redshift space. This is particularly interesting since the model did not include any short-scale effects, which are otherwise essential to model the full PS, and both the scale dependence of RSD and halo bias are encoded in a single exponential prefactor containing just one extra parameter.

We will use a similar model to analyze BOSS experimental data, namely,

$$P_{model}(k,\mu;b,A) = e^{-Ak^2}\Bigg[\Big(b+\mu^2 f\mathcal{R}(k)\Big)^2\Big(P^{nw,l}(k)+P^{w,l}(k)e^{-k^2\Xi^{rs}(\mu)/\gamma_{rec}}\Big) + b^2\Delta P^{nw,1l}_{\delta\delta}(k) + 2b\mu^2 f\Delta P^{nw,1l}_{\delta\theta}(k) + \mu^4 f^2\Delta P^{nw,1l}_{\theta\theta}(k)\Bigg] \tag{5.4}$$

where μ is the cosine of the angle between the wavevector and the line of sight, $P^{nw,l}$ and $P^{nw,l}$ are, respectively, the smooth and the oscillating components of the linear PS, while $\Delta P^{nw,1l}_{ij}(k)$ $(i,j=\delta,\theta)$ denote the components of the real space 1-loop PS, computed using the smooth linear one. The smooth PS is obtained by spline interpolating the linear PS on the points corresponding to nodes of $\sin(k\,r_{\rm bao})$, and the wiggly PS is then the difference between the linear PS and the smooth one.

The $R_{sd}(k)$ term accounts for the removal of large scale redshift space distortions by the reconstruction procedure discussed in the previous section, eq. (5.3), and in the BOSS analysis the 'Rec-Iso' convention of [72] is adopted,

$$\mathcal{R}(k) = \begin{cases} 1 & \text{before reconstruction} \\ \left(1-e^{-\frac{k^2\Sigma_{sm}^2}{2}}\right) & \text{after reconstruction} \end{cases} \tag{5.5}$$

The remaining, nonlinear, redshift space distortions effect is modelled, together with scale dependent bias, by the single pre-factor e^{-Ak^2}. In general, this would be expected to be a poor approximation, as, for instance, it lacks any μ-dependence. However, since, as we will see, we will only include monopole data in our BAO analysis, our simple μ-independent parameterization can be considered as an effective one, after μ-averaging.

The effect of BAO damping by large-scale bulk flows is encoded in the $e^{-k^2\Xi^{rs}(\mu)/\gamma_{rec}}$ term, where the function $\Xi^{rs}(\mu)$ is given by [69]

$$\Xi^{rs}(\mu; r_{bao}) = \left(1 + f\mu^2(2+f)\right)\Xi(r_{bao}) \\ + f\mu^2(\mu^2-1)\frac{1}{2\pi^2}\int dq\, P^{nw,l}(q) j_2(q r_{bao})\,, \quad (5.6)$$

with

$$\Xi(r_{bao}) \equiv \frac{1}{6\pi^2}\int dq\, P^{nw,l}(q;z)\left(1 - j_0(q\, r_{bao}) + 2j_2(q\, r_{bao})\right), \quad (5.7)$$

with $j_n(x)$'s the spherical Bessel functions. Typically, the reconstruction reduces the damping of the BAO of a factor ~ 4 [25]. Hence we divide the exponential damping by a quantity γ_{rec} which is equal to 1 for pre-reconstruction data and to 4 for reconstructed data.

We stress again that eq. (5.4) does not include any short scale correction term as those implemented in the TRG approach discussed in [53], or in the Effective Field Theory of the LSS [37]. Here we want to focus on the performance of the Extractor compared to the standard BAO analysis, as implemented by the BOSS collaboration, and our main goal is to assess the effect of the reduction in nuisance parameters.

From the PS model above we are going to calculate the multipole moments:

$$P_l(k; b, A) \equiv \frac{2l+1}{2}\int d\mu P_{\rm model}(k, \mu; b, A)\mathcal{P}_l(\mu), \quad (5.8)$$

where $\mathcal{P}_l$ are the Legendre polynomials, and $l = 0, 2$ correspond, respectively, to the monopole and quadrupole moment.

5.3 Determining the BAO scale

Our aim is to determine the BAO scale contained in the data. To do this, following the BOSS analysis, we are going to define a parameter α that rescales isotropically the BAO length imprinted in the data with respect to our fiducial cosmological model. In the previous chapters we considered a likelihood function $\chi^2(\alpha)$,

$$\chi^2(\alpha, \cdots) = \sum_{i,j=n_{min}}^{n_{max}} \delta R[P](k_i; \alpha, \cdots)\, c_{ij}^{-1}\, \delta R[P](k_j; \alpha, \cdots)\,, \quad (5.9)$$

with

$$\delta R[P](k_i;\alpha,\cdots) \equiv R[P_{model}](k_i/\alpha,\cdots) - R[P_{data}](k_i)\,, \tag{5.10}$$

where c_{ij} is the covariance matrix of eq. (5.18) below, and dots indicate other possible parameters of the model. Notice the role of the α parameter in rescaling the length scales: if the best fit is for $\alpha = 1$ the model and the data agree on the BAO scale.

In the present analysis, our model contains 2 nuisance parameters, b and A. b mainly fixes the overall normalization of the PS, to which the Extractor operator is essentially insensitive, therefore we fix it with a preliminary fit of the monopole $P_0(k;b,A)$ and quadrupole $P_2(k;b,A)$ up to $k \simeq 0.15\,\mathrm{h\ Mpc^{-1}}$. We will indicate this value with $\bar{b}$. We verified that the specific value of $\bar{b}$ has little impact on the final result.

The parameters A and α have two different physical origins and roles. A is related to RSD and scale-dependent bias, and it mostly modifies the broadband shape of the PS. On the other hand, α carries information on the BAO scale imprinted on the wiggly component. We would like to extract α from the latter and A from the former. Therefore we will combine the two constraints by considering a composite χ^2 (in eq. (5.15) below). In doing so we need to take care of two aspects. First, we need to consider the cross correlations between $P^0(k)$ and $R[P^0](k)$. Second, we must not use the same information twice, both in the full PS and the extracted one.

In order to take care of these two issues we reformulate our procedure as follows (we specify the discussion to the monopole, the procedure is the same for the quadrupole):

First of all we define a list of indices:

$$\{\pi_1,\ldots,\pi_{max},\rho_1,\ldots,\rho_{max}\}, \tag{5.11}$$

where the π_i's are the wavenumber bins used for the full PS, while the ρ_i's are those used for the extracted PS. To make sure we avoid double counting the data, each bin is present at most once in the list, so it will not be used for the fit of the full and extracted PS at the same time. We then define a vector:

$$\begin{aligned} \mathrm{X}(\alpha,A) \equiv \quad & \Big\{\Delta_P(k_{\pi_1},\alpha,A),\ldots,\Delta_P(k_{\pi_{max}},\alpha,A), \\ & \Delta_{RP}(k_{\rho_1},\alpha,A),\ldots,\Delta_{RP}(k_{\rho_{max}},\alpha,A)\Big\}, \end{aligned} \tag{5.12}$$

where

$$\Delta_P(k_i, A) \equiv P^0_{data}(k_i) - P^0_{model}(k_i/\alpha, \bar{b}, A) \tag{5.13}$$

and

$$\Delta_{RP}(k_i, \alpha, A) \equiv R[P^0_{data}](k_i) - R[P^0_{model}](k_i/\alpha, \bar{b}, A). \tag{5.14}$$

χ^2 is now defined as

$$\chi^2(\alpha, A) \equiv \sum_{i,j} \mathrm{X}_i(\alpha, A) C^{-1}_{i,j} \mathrm{X}_j(\alpha, A). \tag{5.15}$$

In this expression we used the covariance matrix

$$C_{i,j} \equiv \begin{cases} \langle \delta P_i \ \delta P_j \rangle & i \in (\pi_1, \pi_{max}), j \in (\pi_1, \pi_{max}) \\ \langle \delta P_i \ \delta R_j \rangle & i \in (\pi_1, \pi_{max}), j \in (\rho_1, \rho_{max}) \\ \langle \delta R_i \ \delta P_j \rangle & i \in (\rho_1, \rho_{max}), j \in (\pi_1, \pi_{max}) \\ \langle \delta R_i \ \delta R_j \rangle & i \in (\rho_1, \rho_{max}), j \in (\rho_1, \rho_{max}) \end{cases} \tag{5.16}$$

where the PS covariance matrix elements, $c_{ij} \equiv \langle \delta P_i \ \delta P_j \rangle$, are obtained from the mock catalogue that we discuss in the following section, while the elements of the last three lines are given in terms of the former by the relations

$$\langle \delta R_i \delta P_j \rangle = D_i^{-1} P_i^{-2} \sum_l f_{i,l} \Big(- P_i \langle \delta P_l \ \delta P_j \rangle + P_l \langle \delta P_i \ \delta P_j \rangle \Big), \tag{5.17}$$

and

$$\begin{aligned} \langle \delta R_i \, \delta R_j \rangle =& D_i^{-1} P_i^{-2} D_j^{-1} P_j^{-2} \sum_{m,n} \Bigg[P_{i+m} \, P_{j+n} \ \langle \delta P_i \delta P_j \rangle \\ & - P_{i+m} \, P_j \ \langle \delta P_i \delta P_{j+n} \rangle - P_i \, P_{j+n} \ \langle \delta P_{i+m} \delta P_j \rangle + P_i \, P_j \ \langle \delta P_{i+m} \delta P_{j+n} \rangle \Bigg]. \end{aligned} \tag{5.18}$$

We note that if we were to repeat one index in π_i and ρ_i the covariance matrix $C_{i,j}$ would become singular, making the analysis procedure fail. In fact, this feature works as a "safety" mechanism that prevents us from inadvertently run into overfitting.

From this $\chi^2(\alpha, A)$ we construct a probability distribution function (PDF) for each redshift bin z, combining the North and South samples, and marginalize over A:

$$f_z(\alpha) = \frac{1}{\mathcal{N}} \int dA \ e^{-\frac{\chi^2_{N,z}(\alpha,A) + \chi^2_{S,z}(\alpha,A)}{2}}. \tag{5.19}$$

The factor $\mathcal{N}$ normalises the total probability to 1. When reporting the results, the error on α is going to be the 1σ interval of the PDF, which integrated gives the value of 0.683. In constructing the PDF as shown above we are assuming that the parameter A is the same for the NGC and SGC samples. We tested the impact of assuming two separate parameters A_N and A_S and marginalising over them separately and found analogous results.

5.4 Calibration with Mock galaxies

Before applying the procedure to the experimental data we tested it on the MultyDark Patchy mock catalogues of the BOSS collaboration [67, 68]. The fiducial cosmological model used to generate these mocks was a flat ΛCDM model with $\Omega_M = 0.307115$, $\Omega_b = 0.048206$, $\sigma_8 = 0.8288$, $n_s = 0.9611$ and $H_0 = 67.7$ km s^{-1} Mpc^{-1}. In fig. 5.1 we plot the output of the extractor applied to the monopole PS, pre- and post-reconstruction. The corresponding χ^2 is plotted in fig. 5.2. These results have been obtained using $\pi_i = \{1, 2, 3, 7, 15\}$ and $\rho_i = \{4, \ldots, 6, 8, \ldots, 14, 16, \ldots, 25\}$, where the correspondence between the bin number and the actual wavenumber can be read from the plot. We also mark with a red horizontal line the value for A that is obtained through a many-parameter fit of eq. 5.4 against the monopole data (before applying the Extractor) up to $k < 0.155\,\mathrm{hMpc}^{-1}$.

The optimal configuration is to use most bins in ρ, given that the extracted PS has greater constraining power on α, and use just a few bins in π to determine A. Apart from this, however, the results do not depend on the exact choice for π and ρ. Since the extractor is an integrated quantity, the first bins of R[P] are affected by boundary effects, so a natural choice is for them to be in π. Furthermore we found that considering points up to $k \leq k_{max} = 0.26\,\mathrm{hMpc}^{-1}$ yields the optimal trade-off between accuracy on α and the $\chi^2/n_{d.o.f.}$

The results for the α parameter from the monopole are listed in Table 5.1. The recovered values of α are compatible with 1 for all redshift bins, which shows that our procedure provides an unbiased estimate of the BAO scale contained in the mock data. Moreover, the constraints we get are well below the 1 % level and, compared to the 10-parameter fit of the BOSS analysis, tighter by a factor $2.7 - 2.8$ for the data pre-reconstruction and $1.7 - 1.9$ after reconstruction.

We also applied the extractor to the mock quadrupole moment. As can

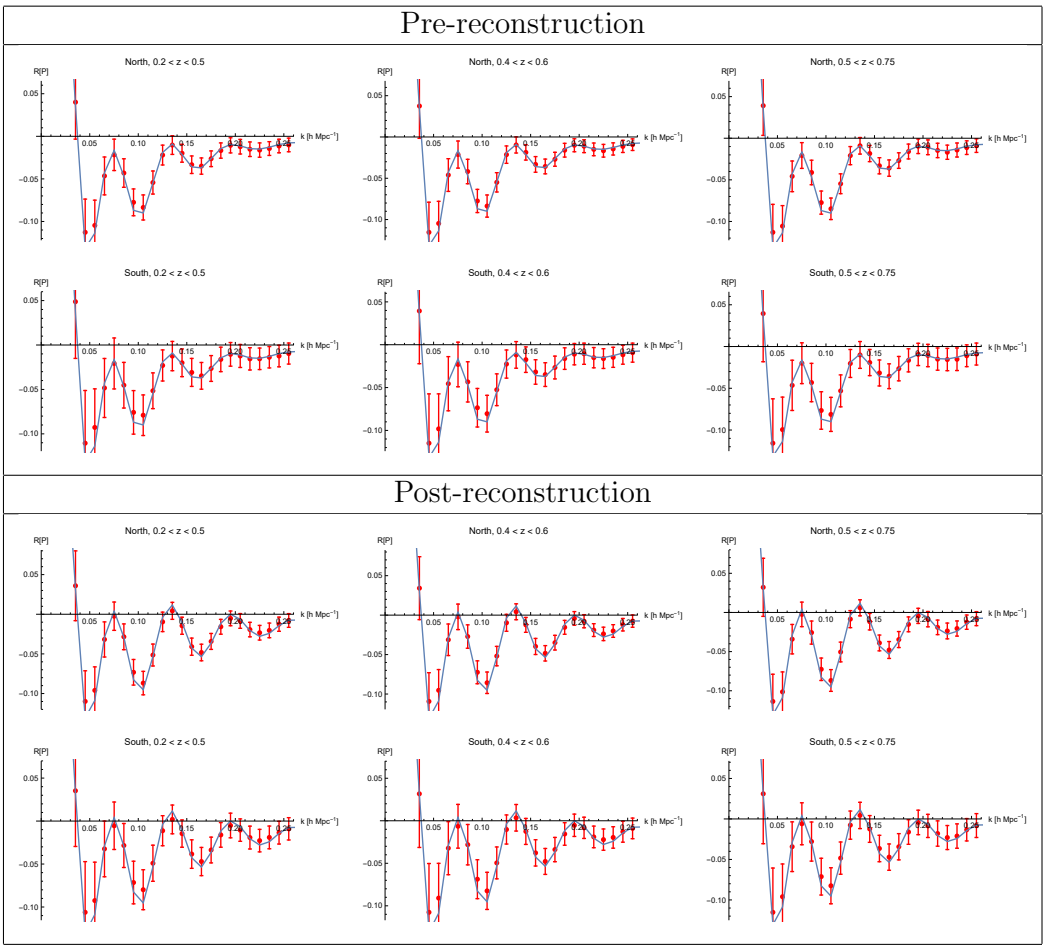

Figure 5.1: Extracted monopoles for the MultyDark Patchy mock galaxies. Solid lines correspond to the best fit model of eq. (5.4).

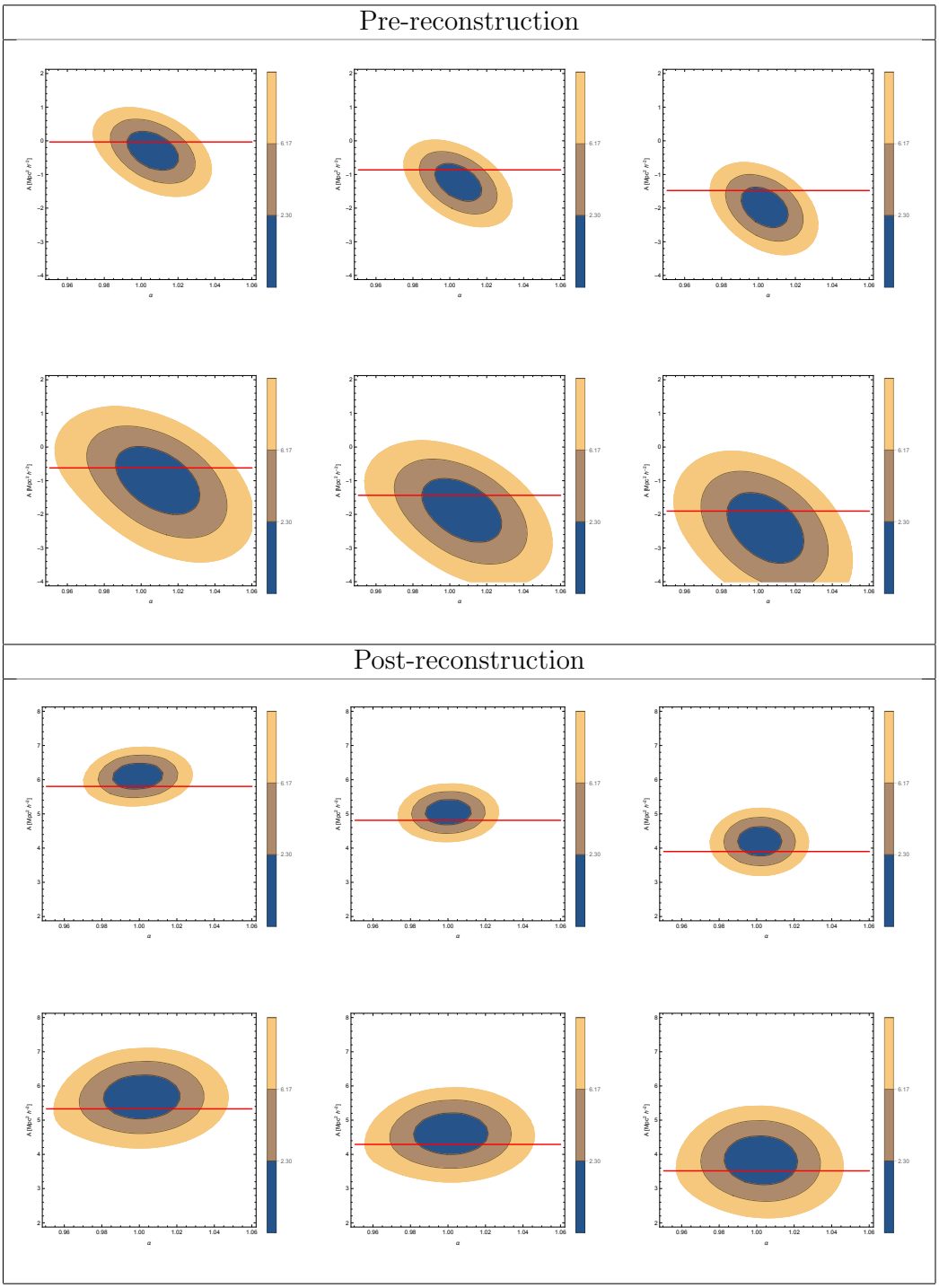

Figure 5.2: Values of $\chi^2(\alpha, A) - \chi^2_{min}$ for mock galaxies. The contour lines correspond to the 1σ (2.30), 2σ (6.17) and 3σ (11.8) intervals for the 2D χ^2 distribution. The red horizontal line marks the best-fit value for A that is obtained by fitting eq. 5.4 directly on the PS, without applying the Extractor and without any shift.

BOSS collaboration				
	Pre-reconstruction		Post-reconstruction	
	α	error	α	error
$0.2 < z < 0.5$	1.010	0.022	1.002	0.013
$0.4 < z < 0.6$	1.010	0.019	1.003	0.012
$0.5 < z < 0.75$	1.008	0.019	1.003	0.012
Extractor procedure				
	Pre-reconstruction		Post-reconstruction	
	α	error	α	error
$0.2 < z < 0.5$	1.007	0.008	0.999	0.007
$0.4 < z < 0.6$	1.005	0.007	1.001	0.007
$0.5 < z < 0.75$	1.004	0.007	1.002	0.007

Table 5.1: Results for the parameter α obtained with the standard procedure (BOSS collaboration, Ref. [71]) and by applying our analysis to mock galaxy data.

be seen in fig. 5.3, in the extracted quadrupole there is no evident oscillatory feature, meaning that the BAO signal is covered by the noise. In fact, adding the quadrupole to the analysis brings no improvement on the determination on α, therefore in this work we will restrict the analysis of the BOSS data to the monopole.

5.5 Application to BOSS DR12 data

Having tested our procedure, and found the optimal setup, with mock galaxies, we apply it to the experimental data. The reference cosmological model is the same as that used for generating the mock catalogues. The extracted monopoles are shown in fig. 5.4. As in the case of the mock PS, we can see the effect of reconstruction in enhancing the amplitude of the BAO wiggles. The corresponding contour plots for χ^2 are shown in fig. 5.5.

Finally, the results for α are shown in Tab. 5.2. The obtained precision is analogous to the one obtained for the mock galaxies, well below the percent level both for pre- and post-reconstruction data. The gain for pre-reconstruction data is around a factor $2.3-2.7$, while for post-reconstruction data it is about 2.2 for the lowest redshift range and around 1.4 for the two

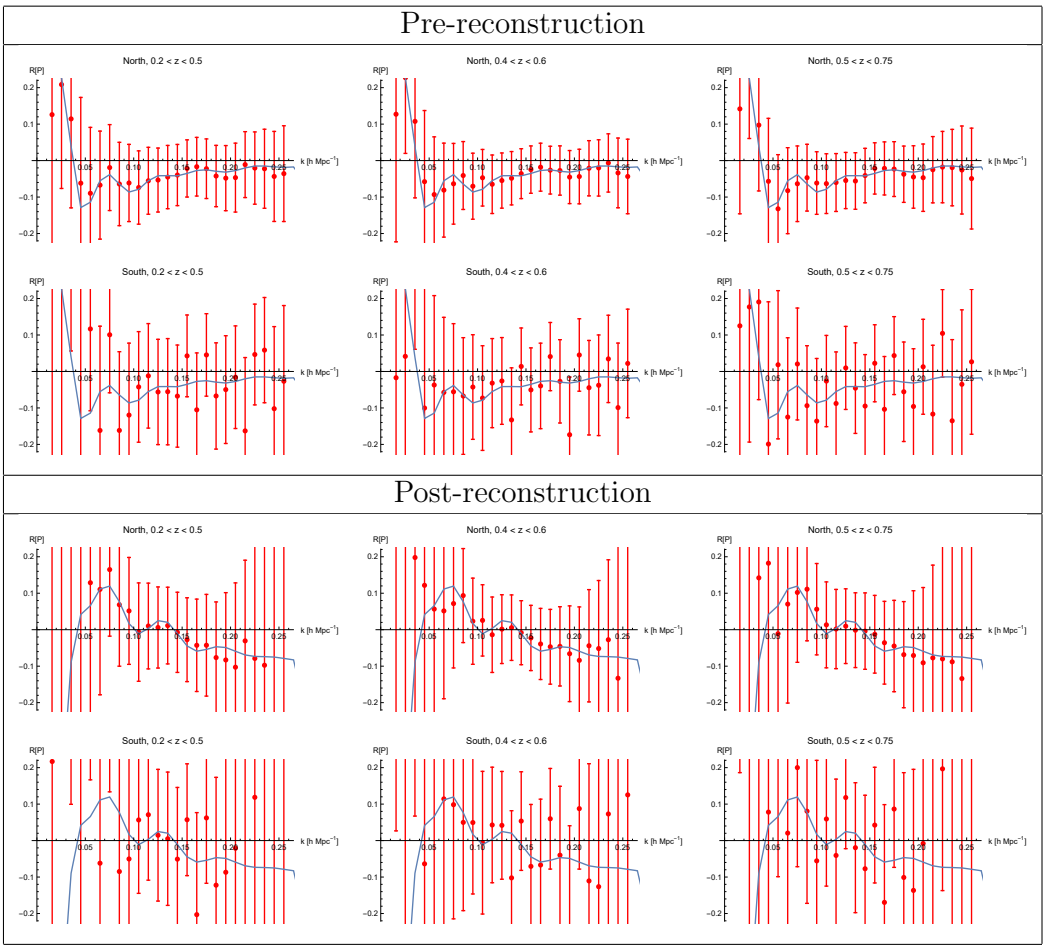

Figure 5.3: Extracted quadrupoles for the MultyDark Patchy mock galaxies. Solid lines correspond to the best fit model of eq. (5.4).

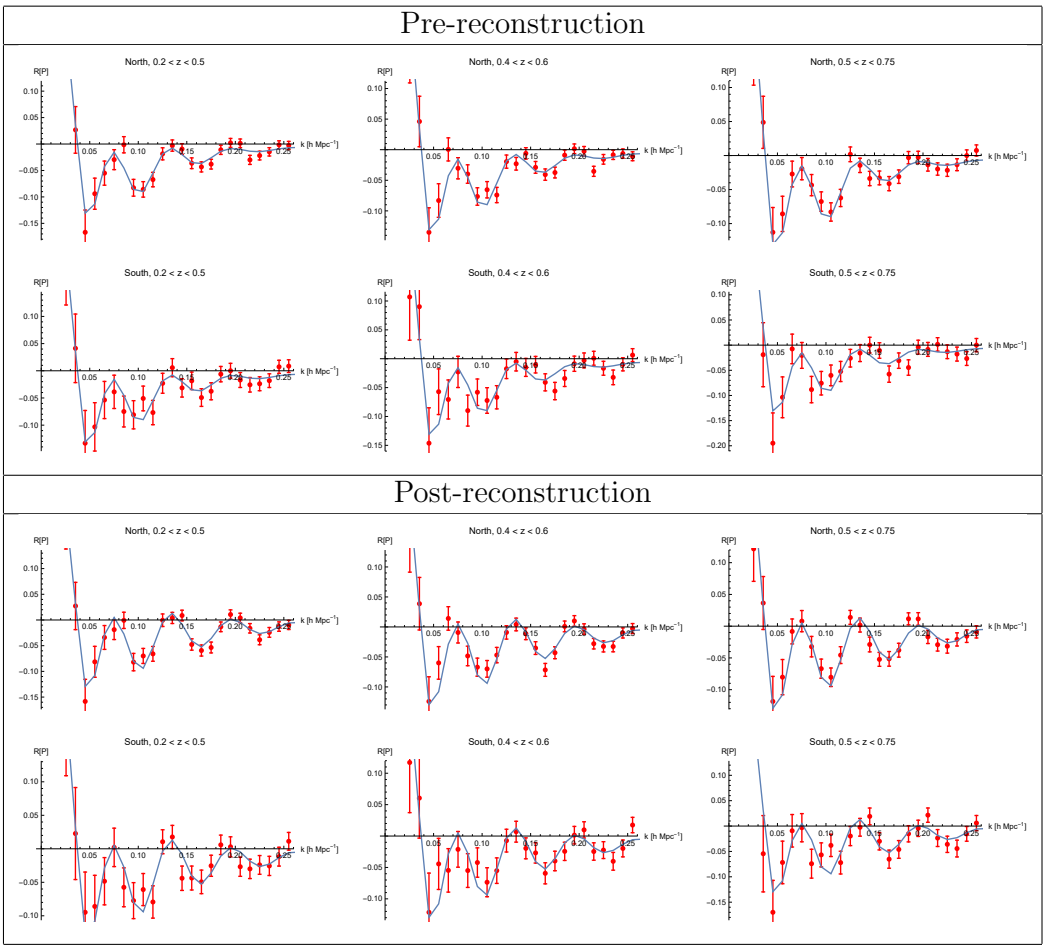

Figure 5.4: Extracted monopoles for the BOSS data. Solid lines correspond to the best fit model of eq. (5.4).

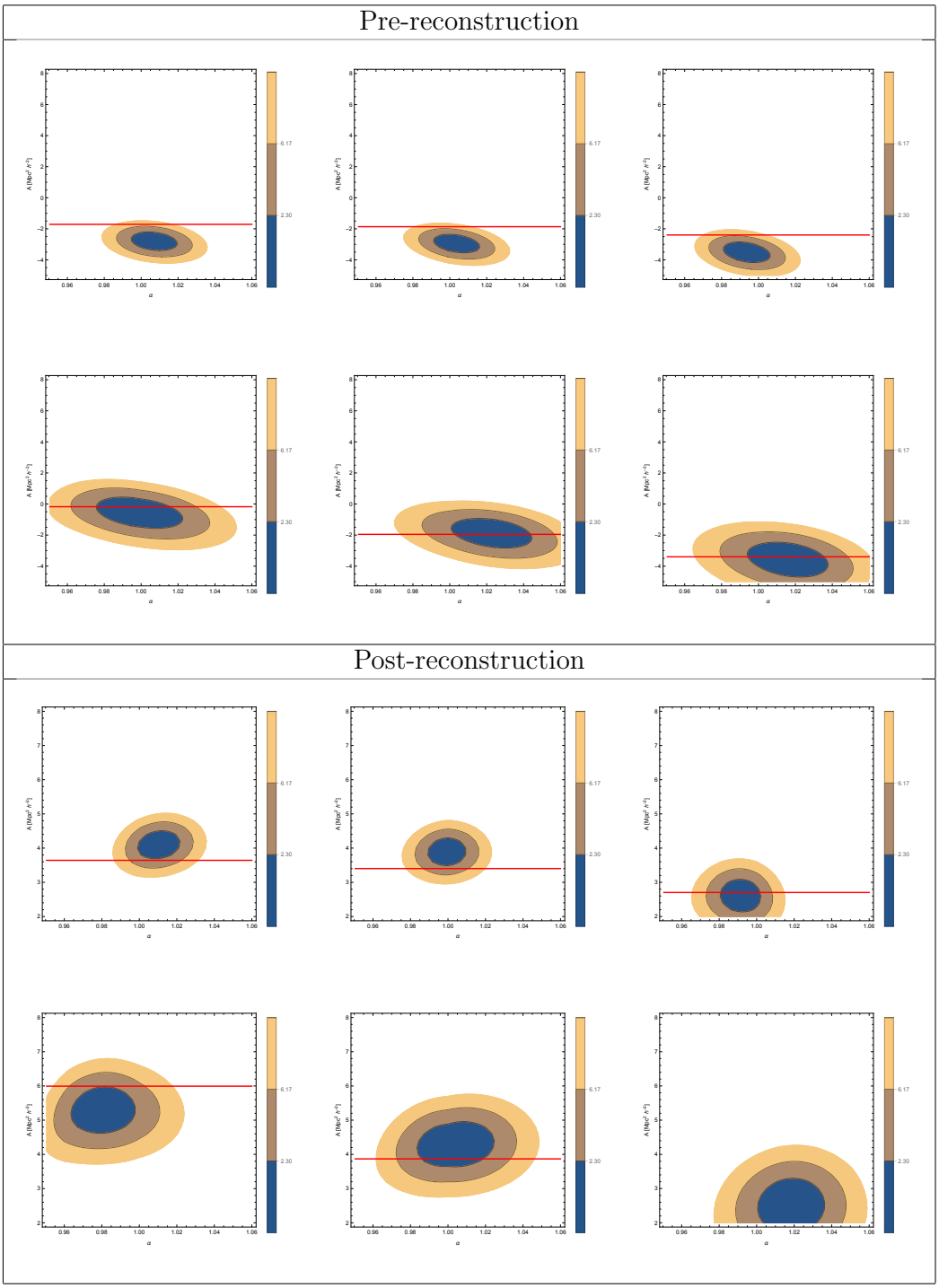

Figure 5.5: Values of $\chi^2(\alpha, A) - \chi^2_{min}$ for BOSS data. The contour lines correspond to the 1σ (2.30), 2σ (6.17) and 3σ (11.8) intervals for the 2D χ^2 distribution. The red horizontal line marks the best-fit value for A that is obtained by fitting eq. 5.4 directly on the PS, without applying the Extractor and without any shift.

higher redshift ones.

5.6 Conclusions

The Extractor procedure represents a promising approach to the study of BAOs, both from a theoretical and data analysis point of view. Despite using a simple model, eq. (5.4), the procedure was able to reach a subpercent precision for all redshift bins, using only a one nuisance parameter besides α. Applying the Extractor procedure on unreconstructed data gives constraints tighter than those obtained in the standard analysis after reconstruction. On the other hand, reconstruction does not add any substantial improvement on the constraints obtained with the Extractor procedure.

The BAO signature, as defined by the Extractor prescription, is mostly confined to the monopole PS. This is clear from fig. 5.3, and from the analogous one for the quadrupole from real data. Adding higher multipoles does not lead to any substantial improvement in our results. Therefore, constraining anisotropic scaling parameters, $\alpha_\perp$ and $\alpha_{||}$, appears to us premature, given the present data.

There are a number of ways this method can be improved, also in view of future data. The exploration of the parameter space can go beyond the α-parameterization, by using Monte Carlo Markov Chain algorithms. On the theoretical side, the model we used used essentially a 1-loop approximation, while we showed that using the full TRG method presented in [53] improves the BAO scale extraction at virtually no extra computational cost. Although the modelling of RSD and halo bias presented here was very basic, the simple exponential factor $\exp(-Ak^2)$ gave already good results. A more detailed description of these effect would likely improve further the constraints on α. Moreover, by modelling the angular dependence of RSD more accurately, the quadrupole and, possibly, the hexadecapole data could be included in the analysis. We leave these improvements to future work.

BOSS collaboration				
	Pre-reconstruction		Post-reconstruction	
	α	error	α	error
$0.2 < z < 0.5$	1.006	0.016	1.000	0.013
$0.4 < z < 0.6$	1.016	0.017	0.9936	0.0082
$0.5 < z < 0.75$	0.991	0.019	0.9887	0.0087
Extractor procedure				
	Pre-reconstruction		Post-reconstruction	
	α	error	α	error
$0.2 < z < 0.5$	1.005	0.007	1.003	0.006
$0.4 < z < 0.6$	1.008	0.007	1.000	0.006
$0.5 < z < 0.75$	0.999	0.007	0.999	0.006

Table 5.2: Results for the parameter α obtained with the standard procedure (BOSS collaboration, Ref. [71]) and by applying our analysis to BOSS experimental data

Chapter 6

Conclusions and outlook

In this thesis we have introduced the improved TRG model, with corrections in the IR and UV sectors and tested its performance. We compared its results against N-Body simulations and in Section 4.3 we have shown that the PS generated with the TRG at 1-loop agrees with N-Body simulations at the sub-percent level in the whole BAO region for $z \geq 0.5$ and up to $k \sim 0.14h^{-1}$ Mpc at $z = 0$.

We have defined the Extractor operator as a means to extract the oscillating part of any PS, and have shown that this component, unlike the smooth part, is weakly dependent on the UV contributions. Therefore, it can be modelled using only the IR corrections. We have also tested the ability of the Extractor operator to retrieve the BAO scale from a given PS using N-Body simulations. As shown in Chapter 4 the Extractor procedure recovers the BAO scale with sub-percent accuracy also in the presence of halo bias and RSD, whose scale dependence can be taken into account with the addition of a single nuisance parameter, in the form of an exponential factor e^{-Ak^2}.

We then proceeded to the application of our analysis to the BOSS DR12 dataset. The Extractor procedure was able to determine the BAO scale from the monopole data with an accuracy that is $\sim 30\%$ better than what is obtained with the standard 8-parameter fit, when applied to pre-reconstruction data, while it yields similar results when applied to reconstructed data. When applying the Extractor to quadrupole data we find no clear BAO signal, signifying that better data is required to perform an angular analysis with the Extractor.

The content of Chapters 3 and 4 have been published on the Journal of

Cosmology and Astrophysics, as Noda, Peloso and Pietroni, *A Robust BAO Extractor*, (JCAP 1708, 2017, no. 08 007) and Nishimichi, Noda, Peloso and Pietroni, *BAO Extractor: bias and redshift space effects*, (JCAP 1801, 2018, no. 01 035). The analysis of BOSS data contained in Chapter 5 will be the matter of a forthcoming publication.

Several improvements can be made to the methods introduced in this thesis. In this work the PS has been calculated with the improved TRG with UV corrections evaluated at 1-loop order. At $z = 0$, this level of approximation performs well in extracting the acoustic scale from BAO's, however, if one is interested in the broadband shape of the PS, as for instance is required to derive limits on the neutrino mass scale, a 2-loop calculation is needed.

As pointed out in the text, the BAO Extractor performance on real data can also be improved, by adding the effect of UV sources and by treating the angular dependence of RSD more accurately.

So far we have studied how well the Extractor can measure the BAO scale. A further step forward would be to see how this measurement maps on the determination of the cosmological parameters. In particular it would be important to test whether this procedure converges to the exact solution when exploring the parameter space. In the setting we have presented, the numerical computations are very fast, therefore the Extractor procedure appears to be a promising candidate in the parameter estimation analysis.

The ability of the improved TRG to correctly reproduce the nonlinear dynamics can be used to test, apart from ΛCDM, all the models that predict a signature on the full shape of the PS, like massive neutrinos, Modified Gravity, fuzzy DM, coupled quintessence and so on. In parallel, the Extractor offers the opportunity to study the same models by using the BAO as a precision probe. In particular we could exploit both the position and the amplitude of the BAO peaks.

In summary the improved TRG and the Extractor operator constitute two promising tools, which combined will contribute to the study of the Universe at Large Scales.

Appendix A

Diagrammatic representation of SPT

In Section 2.1.1 we have introduced the approach of SPT. Each n-order contribution to the field φ can be obtained via an iterative relation (see for example [21]), which is particularly suited for numerical algorithms. However Crocce and Scoccimarro [26, 27] introduced a way to organise the contribution in diagrams that give a better insight in the mode-coupling structure of each contribution.

The equation of motion, Eq. 2.16, has a formal solution which is the sum of the homogeneous solution plus a non-homogeneous solution:

$$\begin{aligned}\varphi_a(\mathbf{k},\eta) &= g_{ab}(\eta,\eta_{in})\varphi_b(\mathbf{k},\eta_{in}) \\ &\quad + \int_{\eta_{in}}^{\eta} d\eta' g_{ab}(\eta-\eta') I_{\mathbf{k},\mathbf{p},\mathbf{q}} e^{\eta'} \gamma_{bcd}(\mathbf{k},\mathbf{p},\mathbf{q})\varphi_c(\mathbf{p},\eta')\varphi_d(\mathbf{q},\eta'). \quad \text{(A.1)}\end{aligned}$$

Here $g_{ab}(\eta_1,\eta_2)$ is the Green function of the linear equation, also called *propagator* and reads:

$$g_{ab}(\eta_1,\eta_2) = \frac{1}{5}\left[\begin{pmatrix}3 & 2\\ 3 & 2\end{pmatrix} + e^{-\frac{5}{2}(\eta_1-\eta_2)}\begin{pmatrix}2 & -2\\ -3 & 3\end{pmatrix}\right], \quad \text{(A.2)}$$

The n-th order perturbative contribution is obtained by reiterating the equation of motion at the r.h.s. n times starting from the homogeneous

solution:

$$\begin{aligned}
\varphi_a^{(1)}(\mathbf{k},\eta) &= g_{ab}(\eta,\eta_{in})\varphi_b(\mathbf{k},\eta_{in}) \\
\varphi_a^{(2)}(\mathbf{k},\eta) &= \int_{\eta_{in}}^{\eta} d\eta' g_{ab}(\eta-\eta') I_{\mathbf{k},\mathbf{p},\mathbf{q}} e^{\eta'} \gamma_{bcd}(\mathbf{k},\mathbf{p},\mathbf{q}) \\
&\quad \times g_{ce}(\eta',\eta_{in})\varphi_e(\mathbf{k},\eta_{in}) g_{df}(\eta',\eta_{in})\varphi_f(\mathbf{k},\eta_{in}) \\
&\quad \dots \\
\varphi_a^{(n)}(\mathbf{k},\eta) &= \sum_{m=1}^{n-1} \int_{\eta_{in}}^{\eta} d\eta' g_{ab}(\eta-\eta') I_{\mathbf{k},\mathbf{p},\mathbf{q}} e^{\eta'} \gamma_{bcd}(\mathbf{k},\mathbf{p},\mathbf{q}) \varphi_c^{(m)}(\mathbf{p},\eta') \varphi_d^{(n-m)}(\mathbf{q},\eta').
\end{aligned} \tag{A.3}$$

At this point it becomes clear that all the contributions can be constructed starting from 3 building blocks: the initial fields $\varphi_a(\mathbf{k},\eta_{in})$, the propagator $g_{ab}(\eta,\eta')$ and the interaction function $e^{\eta}\gamma_{abc}(\mathbf{k},\mathbf{p},\mathbf{q})$.

The quantity that we want to calculate is the 2-point correlation function, and at a finite order n it will be given by the sum of the 2-point correlators $\langle \varphi^{(l)} \varphi^{(m)} \rangle$ for which $n = l + m$. This will break down in combinations of n-point correlation functions of initial fields $\varphi(\mathbf{k},\eta_{in})$. If we make the further assumption of Gaussian initial conditions, Wick's theorem, Eq. 2.22, then the initial n-point correlators will break down to combinations of initial PS. At this point any finite order PS is made entirely from $g_{ab}(\eta,\eta')$, $e^{\eta}\gamma_{abc}(\mathbf{k},\mathbf{p},\mathbf{q})$ and the initial PS, $P^0(\mathbf{k})$. If we define a graphical representation for each of these components, as shown in Fig A.1, then we can draw a diagram for each of the terms that make up our SPT PS. These diagrams can be classified based on their topology and more specifically on their number of closed *loops*. The number of loops directly correlates to the perturbative order, 1-loop containing 2 initial PS, 2-loops containing 3 and so on.

As an example we are going to write down the expression for the 1-loop correction to the PS. It is the sum of two types of contributions, or diagrams:

$$\Delta P_{ab}^{1-loop}(\mathbf{k},\eta) = P_{ab}^{13}(\mathbf{k},\eta) + P_{ba}^{13}(\mathbf{k},\eta) + P_{ab}^{22}(\mathbf{k},\eta), \tag{A.4}$$

where

$$\begin{aligned}
P_{ab}^{22}(\mathbf{k},\eta) &= 2\int^{\eta} ds \int^{\eta} ds' g_{ac}(\eta-s) g_{bf}(\eta-s') \\
&\quad \times I_{\mathbf{k},\mathbf{p},\mathbf{q}} e^{s} \gamma_{cde}(\mathbf{k},\mathbf{p},\mathbf{q}) e^{s'} \gamma_{fgh}(-\mathbf{k},-\mathbf{p},-\mathbf{q}) P_{dg}^0(p) P_{eh}^0(q)
\end{aligned} \tag{A.5}$$

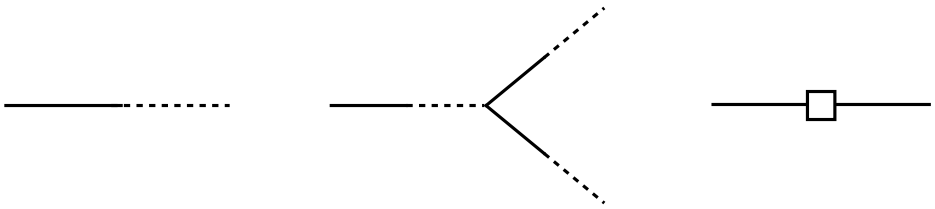

Figure A.1: Graphical representation of the three building blocks of SPT. From left to right: the propagator $g_{ab}(\eta, \eta')$, the interaction function $\gamma_{abc}(\mathbf{k}, \mathbf{p}, \mathbf{q})$ and the initial PS, $P^0(\mathbf{k})$

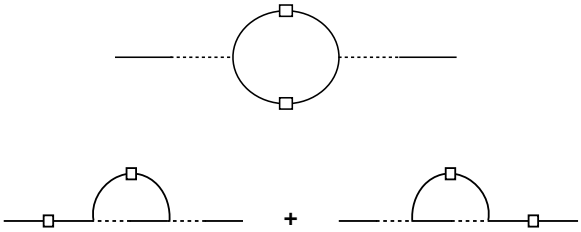

Figure A.2: Diagrammatic representation of the P^{22} contribution (top) and P^{13} contribution (bottom)

and

$$P^{13}_{ab}(\mathbf{k}, \eta) = 4 \int^{\eta} ds g_{ac}(\eta - s) \int^{s} ds' g_{ef}(s - s') \\ I_{\mathbf{k},\mathbf{p},\mathbf{q}} e^{s} \gamma_{cde}(\mathbf{k}, \mathbf{p}, \mathbf{q}) e^{s'} \gamma_{fhg}(-\mathbf{q}, -\mathbf{p}, -\mathbf{k}) P^0_{dh}(p) P^0_{gb}(k). \qquad \text{(A.6)}$$

In writing these expressions we have assumed that the initial PS was in the growing mode, so that $g_{ac}(\eta, \eta_{in}) g_{bd}(\eta, \eta_{in}) P^0_{cd}(\mathbf{k}) = P^0_{ab}(\mathbf{k})$. This is a sensible assumption since the decaying mode becomes less and less relevant with time. These terms are graphically represented in Fig. A.2 where the 1-loop topology becomes apparent.

Appendix B

Computation of $\Delta\alpha\left(\eta\right)$

In this Appendix we briefly discuss how we computed the coefficient $\frac{\Delta\alpha(\eta)}{k_m^2}$ used in the TRG equations (3.31) and (3.35). We recall from equations (3.18) and (3.19) that it is obtained from the correlator between the source h_a^R and the course grained fields φ^R measured from N-body simulations, minus the corresponding quantity evaluated in single stream approximation.

We use the N body simulations of the 'reference' cosmology of [40] (see Section 4 of that work for details). We use the simulations to evaluate $\frac{\langle h_2^R(\mathbf{k},\eta)\varphi_1^R(-\mathbf{k},\eta)\rangle'}{\langle\varphi_1^R(\mathbf{k},\eta)\varphi_1^R(-\mathbf{k},\eta)\rangle'}$ at the redshifts $z = 0$, 0.25, 0.5, 1, 1.5, 2, 3, 5. We fix the filter scale at $R = 2\,\mathrm{Mpc}\,h^{-1}$, which is the smallest value of R at which the resulting $\Delta\alpha$ is in the plateau region visible in the left panel of Figure 3.2 (we verified that using larger values of R does not change the final values of $\Delta\alpha$ significantly). We then evaluate the coefficient $\frac{\alpha^R}{k_m^2}$ at $k = 0.1\,h/\mathrm{Mpc}$ (as visible from the right panel of Figure 3.2, the result does not significantly change if we use a different but comparable scale).

From this quantity we subtract the analogous ratio $\frac{\langle h_2^R(\mathbf{k},\eta)\varphi_1^R(-\mathbf{k},\eta)\rangle'}{\langle\varphi_1^R(\mathbf{k},\eta)\varphi_1^R(-\mathbf{k},\eta)\rangle'}$, with the numerator evaluated in single stream approximation through a one loop computation, and with the Coyote Emulator [45] PS in the denominator. The one loop computation is performed following Appendix A of [40]. [1]

[1]Specifically, we add up "22" and "13" contributions. The "22" contributions are obtained from the terms $\mathcal{C}^{h0}$ (only half of it) and $\mathcal{C}^{hh}$ written in Eqs. (A.13) and (A.14) of [40]; the "13" contributions are obtained from Eqs. (A.20)-(A.21)-(A.22)-(A.23) of [40]. The correlators written in [40] are given in terms of the quantity denoted as $\bar{\varphi}^{(h)}$ in that work. To obtain the correlators in terms of h_a we formally performed the replacement $g_{ac}\left(\eta - s\right) \to \delta_{ac}\delta^{(D)}\left(\eta - s\right)$ in the expressions of [40].

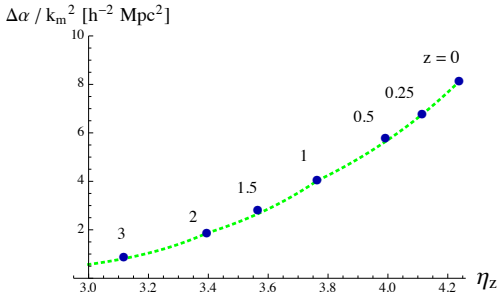

Figure B.1: Coefficient $\frac{\Delta\alpha}{k_m^2}$ as a function of the logarithm η of the linear growth factor. The points are the data obtained at various redshift, as explained in the text. The numerical value next to each point indicates the corresponding redshift. The green dashed curve is the fit (B.1), with the coefficients $\mathcal{C}_0 = 8.11\,h^{-2}\,\mathrm{Mpc}^2$, $n_1 = 1.48$, and $n_2 = 2.09$.

From this subtraction, we obtain the coefficient $\frac{\Delta\alpha}{k_m^2}$ at the various redshifts listed above. In the ETRG system a continuous function $\alpha\,(\eta)$ is needed. We find that the time dependence is well reproduced by the three-parameter fit:

$$\frac{\Delta\alpha\,(\eta)}{k_m^2} = \begin{cases} \mathcal{C}_0\,\mathrm{e}^{n_1(\eta-\eta_0)} & , \quad \eta_1 \le \eta \le \eta_0 \ , \\ \mathcal{C}_0\,\mathrm{e}^{n_1(\eta_1-\eta_0)}\,\mathrm{e}^{n_2(\eta-\eta_1)} & , \quad \eta_2 \le \eta \le \eta_1 \ , \\ \mathcal{C}_0\,\mathrm{e}^{n_1(\eta_1-\eta_0)}\,\mathrm{e}^{n_2(\eta_2-\eta_1)}\,\mathrm{e}^{3(\eta-\eta_2)} & , \quad \eta \le \eta_2 \ , \end{cases} \tag{B.1}$$

where $\eta_i = \eta\,(z_i)$. This parameterization ensures that $\Delta\alpha\,(\eta)$ is continuous, and that it grows faster than the 1-loop single stream term at $z > z_2$ (as suggested by the fact that this subtracted quantity contains terms that are of higher order in perturbation theory. This behavior is in qualitative agreement with our highest redshift data). We perform a fit of the data at $z = 0,\ 0.25,\ 0.5,\ 1$ in a $\{\log\eta,\ \log\Delta\alpha\}$ plane, and obtain the best fit values $\mathcal{C}_0 = 8.11\,h^{-2}\,\mathrm{Mpc}^2$ and $n_1 = 1.48$. We then fit the data at $z = 1,\ 1.5,\ 2$ to obtain the best fit value $n_2 = 2.09$. The parameterization (B.1), with these values for the three fitting parameters $\mathcal{C}_0$, n_1, n_2, is used in the TRG evolutions of the main text.

Appendix C

TRG

Here we summarize the Time Renormalization Group (TRG) system of equations for the PS derived in [53] and used in this work. The PS comprises of two parts: a smooth broadband ("no-wiggle") component P^{nw}, and a smaller ("wiggle") part P^{w} that contains the BAO oscillations. We consider two separate equations for the two components. As a starting point we separate the linear power spectrum in a smooth plus an oscillatory component, $P^0 = P^{0,nw} + P^{0,w}$. To achieve this, we notice that the oscillatory part is of the form $P^{0,w} = \tilde{P}(k) \sin(k\, r_{bao})$, where $\tilde{P}(k)$ is a smooth function, and the scale r_{bao} can be estimated, for any given cosmology, through eq. (6) of [47]. We construct $P^{0,nw}$ by evaluating the PS at the nodes of $\sin(k\, r_{bao})$ and by interpolating in a smooth way between these values.

We then use $P^{0,nw}$ to compute the one-loop SPT correction $\Delta P^{1-loop,nw}$.

SPT fails to accurately reproduce the PS at scales $k \gtrsim 0.1\, h\,\mathrm{Mpc}^{-1}$. This is due both to UV effects that go beyond the single stream approximation, and to IR effects, such as large scales bulk flow. As discussed in [53], UV effects mostly impact the smooth component P^{nw}, and can be accounted for by including additional terms in the TRG evolution equation for the PS. These terms can be evaluated through N-body simulations [39, 40, 53]. While this correction considerably improves the PS at $k \gtrsim 0.1\,\mathrm{h\ Mpc}^{-1}$, it does not affect the BAO oscillation scale extracted from $R[P]$ [53]. We demonstrate this in Section 4.2, where we show that the scale extracted from the halo catalog from our numerical simulations is in excellent agreement with that extracted from a theoretical PS obtained without this UV terms.

On the contrary, IR bulk flows decease the coherency of the BAO oscillations, and need to be included in order to accurately reproduce the oscillatory

behavior of P^w. These effects can be resummed in an exponential (scale-dependent) suppression of the oscillatory term, given by the last term of eq. (4.13). While this result case derived in [53] on the basis on the consistency relations between the power spectrum and the squeezed bispectrum (the soft mode of which is a IR bulk flow) [35], in D we provide an alternative proof that can be more immediately extended to redshift space.

Appendix D

IR resummation

In this appendix we study how IR bulk flows resum to the exponential term in eq. (4.13) of the main text. This effect of the IR modes on the oscillatory part of the PS was derived in real space in [53]. We rederive this result using a Lagrangian formulation, that can be easily extended to redshift space.

We consider a large set of particles, and we split their velocities in long ("l") and short ("sh") wavelength components, treating the former in linear theory (the splitting can be done, for instance, by computing the average velocity of the particles contained in a "large" volume, and splitting the velocity of each particle in that volume as the average plus a residual). We denote as f the phase space distribution of the particles and as $f^{\rm sh}$ the distribution that the particles would have if their position was not changed by the long wavelength velocity. The two distributions are related by

$$f\left(\mathbf{x},\mathbf{p}^{l},\mathbf{p}^{sh},\eta\right)=\int d^{3}y\, f^{sh}\left(\mathbf{y},\mathbf{p}^{l},\mathbf{p}^{sh},\eta\right)\delta_{D}\left(\mathbf{y}-\mathbf{x}+\frac{\mathbf{p}^{l}}{am\mathcal{H}f}\right)\,, \quad \text{(D.1)}$$

where $\mathbf{x}$ and $\mathbf{y}$ are spatial coordinates, δ_D the Dirac-delta function, and where the comoving momentum of the particles is related to their velocity by the non relativistic expression $\mathbf{v}=\frac{\mathbf{p}}{a\,m}$ (where a is the scale factor and m the mass of the particles). Integrating the distribution function over the momentum gives the particle number density

$$n\left(\mathbf{x},\eta\right)=\bar{n}\left(1+\delta(\mathbf{x},\eta)\right)=\int d^{3}p^{l}d^{3}p^{sh}f(\mathbf{x},\mathbf{p}^{l},\mathbf{p}^{sh},\eta)\,, \quad \text{(D.2)}$$

where $\bar{n}$ is the average number density, and $\delta\left(\mathbf{x}\right)$ the density contrast. By

Fourier transfroming this relation, and using eq. (D.1), we can write

$$\begin{aligned}(2\pi)^3\delta_D(\mathbf{k})+\delta(\mathbf{k},\eta) &= \bar{n}^{-1}\int d^3y d^3p^l\, d^3p^{sh} e^{-i\mathbf{k}\cdot\mathbf{y}} e^{-i\frac{\mathbf{k}\cdot\mathbf{p}^l}{am\mathcal{H}f}} f^{sh}(\mathbf{y},\mathbf{p}^l,\mathbf{p}^{sh},\eta)\\ &= \int d^3y\, e^{-i\mathbf{k}\cdot\mathbf{y}}\left(1+\delta_{sh}(\mathbf{y},\eta)\right) e^{-i\frac{\mathbf{k}\cdot\mathbf{v}^l(\mathbf{y},\eta)}{\mathcal{H}f}+\cdots}\,, \qquad \text{(D.3)}\end{aligned}$$

where the second line has been obtained by expanding the exponent in the first line around $\mathbf{p}^l=0$, where δ_{sh} is defined from f^{sh} as in eq. (D.2), where bv^l is the first moment

$$\left(1+\delta_{sh}(\mathbf{y},\eta)\right)\mathbf{v}^l(\mathbf{y},\eta)=\bar{n}^{-1}\int d^3p^l\, d^3p^{sh}\,\frac{\mathbf{p}^l}{am}\, f^{sh}(\mathbf{y},\mathbf{p}^l,\mathbf{p}^{sh},\eta)\,, \qquad \text{(D.4)}$$

and where the ellipsis includes the higher moments that we disregard. From (D.3) we obtain the effect of the long wavelength modes on the PS

$$\begin{aligned}P(k) &= \int d^3r\, e^{-i\mathbf{k}\cdot\mathbf{r}}\left\langle (1+\delta_{sh}(\mathbf{r}/2,\eta))(1+\delta_{sh}(-\mathbf{r}/2,\eta)) e^{-i\frac{\mathbf{k}\cdot\left[\mathbf{v}^l(r/2)-\mathbf{v}^l(-r/2)\right]}{\mathcal{H}f}}\right\rangle\\ &\simeq \int d^3r\, e^{-i\mathbf{k}\cdot\mathbf{r}}\left\langle (1+\delta_{sh}(\mathbf{r}/2,\eta))(1+\delta_{sh}(-\mathbf{r}/2,\eta))\right\rangle\\ &\qquad\qquad \times\exp\left[-\int^{\Lambda}\frac{d^3q}{(2\pi)^3}\frac{(\mathbf{k}\cdot\mathbf{q})^2}{q^4}(1-\cos(\mathbf{q}\cdot\mathbf{r}))P^0(q)\right]\,. \qquad \text{(D.5)}\end{aligned}$$

To obtain the second line, we have treated $\mathbf{v}^l$ as linear, gaussian, and uncorrelated with δ_{sh}. The cut-off Λ is introduced as a reminder that only IR modes contribute to $\mathbf{v}^l$. [1]

If we consider the oscillating component of the PS, namely,

$$P^w_{sh}(k)\equiv\int d^3r e^{-i\mathbf{k}\cdot\mathbf{r}}\left\langle (1+\delta^w_{sh}(\mathbf{r}/2,\eta))(1+\delta^w_{sh}(-\mathbf{r}/2,\eta))\right\rangle=\tilde{P}(k)\sin(k\, r_{bao})\,, \qquad \text{(D.6)}$$

[1] The dependence of the results on the cut-off $\Lambda(k)$ has been discussed in [53], where it has been showed that, as long as a ΛCDM linear PS is considered, omitting the cut-off still provides a numerically accurate description of the IR resummation. For this reason we also set $\Lambda(k)=\infty$ in our computations, and we omit the k-dependence from the argument of Ξ.

eq. (D.5) gives a simple result. We insert this expression into (D.5), and we expand the exponential term

$$
\begin{aligned}
P^w(k) = \sum_{n=0}^{\infty} \frac{(-1)^n}{n!} \int d^3r\, e^{-i\mathbf{k}\cdot\mathbf{r}} \int \frac{d^3p}{(2\pi)^3} e^{i\mathbf{p}\cdot\mathbf{r}} \tilde{P}(p) \sin(p\, r_{bao}) \\
\times \int^{\Lambda} \frac{d^3q_1}{(2\pi)^3} \frac{(\mathbf{k}\cdot\mathbf{q}_1)^2}{q_1^4} P^0(q_1)\,(1-\cos(\mathbf{q}_1\cdot\mathbf{r}))\cdots \\
\times \int^{\Lambda} \frac{d^3q_n}{(2\pi)^3} \frac{(\mathbf{k}\cdot\mathbf{q}_n)^2}{q_n^4} P^0(q_n)\,(1-\cos(\mathbf{q}_n\cdot\mathbf{r}))\ .
\end{aligned}
\tag{D.7}
$$

Let us focus on the $n=1$ term. Integrating over r introduces a series of δ_D functions, that can be used in the integral over p, to give

$$
\begin{aligned}
&-\int \frac{d^3q_1}{(2\pi)^3} P^0\left(q_1\right) \frac{\left(\mathbf{k}\cdot\mathbf{q}_1\right)^2}{q_1^4} \Bigg\{ \tilde{P}\left(k\right) \sin\left(k\, r_{\mathrm{BAO}}\right) \\
&\qquad\qquad - \sum_{r_1=\pm} \frac{1}{2} \tilde{P}\left(\left|\mathbf{k}+r_1\mathbf{q}_1\right|\right) \sin\left(\left|\mathbf{k}+r_1\mathbf{q}_1\right| r_{\mathrm{BAO}}\right) \Bigg\} \\
&\simeq -\int \frac{d^3q_1}{(2\pi)^3} P^0\left(q_1\right) \frac{\left(\mathbf{k}\cdot\mathbf{q}_1\right)^2}{q_1^4} \tilde{P}\left(k\right) \sin\left(k\, r_{\mathrm{BAO}}\right) \left[1-\cos\left(\mathbf{q}_1\cdot\hat{\mathbf{k}}\, r_{\mathrm{BAO}}\right)\right]\ ,
\end{aligned}
\tag{D.8}
$$

where the second line has been obtained by expanding the term in parenthesis in the first line in the limit of $q_1 \ll k$ (which is appropriate, as we are considering the effect of IR modes). A direct inspection of the $n=2,3,\ldots$ terms show that the $\int d^3r d^3p$ integration produces an expression that can be simplified analogously to (D.8) (one can expand recursively over the $\mathbf{q}_i$ momenta). This leads to

$$
P^w(k) \simeq P^w_{sh}\left(k\right) \sum_{n=0}^{\infty} \frac{(-1)^n}{n!} \left[k^2\, \Xi\left(r_{\mathrm{bao}}\right)\right]^n = \mathrm{e}^{-k^2\, \Xi(r_{\mathrm{bao}})}\, P^w_{sh}\left(k\right)\ , \tag{D.9}
$$

where

$$
\begin{aligned}
\Xi(r) &\equiv \frac{1}{k^2} \int^{\Lambda} \frac{d^3q}{(2\pi)^3} \frac{(\mathbf{k}\cdot\mathbf{q})^2}{q_1^4} P^0(q) \left(1-\cos(\mathbf{q}\cdot\hat{\mathbf{k}}\, r_{bao})\right) \\
&= \frac{1}{6\pi^2} \int^{\Lambda} dq P^0(q)(1-j_0(qr)+2j_2(qr))\,.
\end{aligned}
\tag{D.10}
$$

This computation can be readily extended to redshift space. In this case, the relation (D.3) is modified into

$$(2\pi)^3\delta_D(\mathbf{k}) + \delta_s(\mathbf{k}) = \int d^3y\, e^{-i\mathbf{k}\cdot\mathbf{y}}\, e^{-i\mathbf{k}\cdot\mathbf{y}}\, (1+\delta_{s,sh}(\mathbf{y}))\, e^{-i\frac{\mathbf{k}\cdot\mathbf{v}^l(\mathbf{y})}{\mathcal{H}f} - i\frac{k_z v_z^l(\mathbf{y})}{\mathcal{H}} + \cdots}\,, \tag{D.11}$$

where δ_s is the density contrast in redshift space, and the $z-$direction is orient along the line of sight. Starting from this expression, and repeating the same steps done to obtain (D.9) now leads to

$$P_w^s(k,\mu) = e^{-k^2\Xi(r,\mu)} P_w^{s,sh}(k)\,, \tag{D.12}$$

where

$$\Xi(r,\mu) \equiv (1+f\mu^2(2+f))\Xi(r) + f^2\mu^2(\mu^2-1)\frac{1}{2\pi^2}\int^{\Lambda} dq P^0(q) j_2(qr)\,, \tag{D.13}$$

and $P_w^{s,sh}(k)$ is the oscillatory part of the PS obtained from the $\delta_{s,sh}(\mathbf{y})$ field.

Appendix E

N-body simulations

We employ a set of N-body simulations created using the public GADGET-2 code [73]. The data consisted in cubic boxes of comoving side length $L_{box} = 2048\ h^{-1}$ Mpc and 2048^3 particles . The cosmological parameters follow those of the Planck 2015 results [74], and are reported in Table E.1.

The initial condition were created at redshift z=29.4 using the generator developed in [75] and parallelized in [76]. The particles were displaced from a uniform grid using second order Lagrangian perturbation theory (2LPT) [77, 78]. The initial redshift is somewhat lower than the values commonly used in literature, but it has been in shown that a higher starting redshift does not improve the result [79].

We employed the method by Angulo and Pontzen [80] to suppress cosmic variance. It consists in running two simulations which have initial conditions with the same magnitude, but opposite phase and then taking the average of the PS obtained from them. In this work we used the data collected at redshift $z = 1.10911$ (in the rest of the paper just indicated with $z = 1$) and $z = 0$. In F we discuss in detail how the diagonal elements of the covariance matrix from our simulations have been measured, and compute the nondiagonal ones in perturbation theory, showing that their effects on our analyses is negligible.

From the data we constructed a halo catalog using the ROCKSTAR halo finder [81] which is based on an adaptive algorithm for refining friend-of-friend groups of particles looking at their six-dimensional phase space distribution. ROCKSTAR also keeps track of the time evolution to improve the consistency of the hierarchy of substructures throughout the evolution. In our work we kept halos more massive than 10^{13} solar masses. Using the

Ω_m	Ω_Λ	Ω_b	h	$\ln(10^{10}A_s)$	n_s
0.3156	0.6844	0.0491	0.6727	3.094	0.9645

Table E.1: Cosmological parameters

	$z=0$			$z=1$		
Mass range	N_{halos}	b_0	b_1	N_{halos}	b_0	b_1
$M_{halo} \geq 10^{13} M_\odot$ (All masses)	3890690	1.387	-0.848	1763542	2.839	4.976
$1.0 \times 10^{13} M_\odot \leq M_{halo} \leq 1.5 \times 10^{13} M_\odot$	1338222	1.145	0.510	796154	2.425	4.242
$1.5 \times 10^{13} M_\odot \leq M_{halo} \leq 3.0 \times 10^{13} M_\odot$	1370335	1.293	-0.226	665216	2.844	5.953
$3.0 \times 10^{13} M_\odot \leq M_{halo} \leq 5.0 \times 10^{13} M_\odot$	547274	1.497	-1.204	191029	3.555	8.608
$M_{halo} \geq 5.0 \times 10^{13} M_\odot$	634859	2.026	-4.150	111144	4.722	30.45

Table E.2: The table shows the number of halos in our Nbody simulation for $z = 0$ and $z = 1$, averaged over realizations and divided in different bins according to their mass. The other columns refer to the parameters for the halo PS, where we used $P_{halo}(k) = (b_0 + b_1 k^2)^2 P_{Nbody}(k)$ as the scale dependence bias funtion (the coefficient b_1 is given in units of $h^{-2}\,\mathrm{Mpc}^2$).

Cloud-in-Cell interpolation we constructed the density contrast field for the Dark Matter and Dark Matter Halos, both in real space and in redshift space (using the distant observer approximation). From these we then calculate the relevant PS after moving to Fourier space, via FFT.

At this point we can estimate the effect of bias on the nonlinear PS. In figure E.1 we plot the ratio between the halo density PS and the underlying DM PS at redshift $z = 0$ and $z = 1$, divided in mass bins. The number of halos in each bin is shown in Table E.2.

We use $P_{halo}(k) = (b_0 + b_1 k^2)^2 P_{DM}(k)$ as the scale-dependent model for the halo bias. Although it does not fit well the data at all scales, we verified that in order to extract the BAO it is sufficient to fit just the largest scales. To this end, we obtain the coefficients b_0 and b_1 by imposing that the bias function reproduces the ratio between the halo and matter PS at $k = 0.05$ h Mpc^{-1} and at $k = 0.1$ h Mpc^{-1}. The resulting coefficients are listed in Table E.2, and the performance of the fitting functions are of the same quality than those shown in Figure E.1, which have been obtained by using an exponential function e^{-Ak^2}.

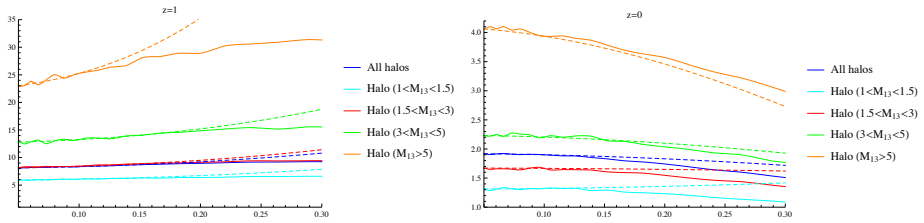

Figure E.1: Bias for each halo bin and for the total halos of $M > 10^{13}\, M_\odot$ in our simulations. The solid lines are the ratio between the halo and the matter power spectra. The dashed lines is the scale dependent bias $(b_0 + b_1\, k^2)^2$, with the coefficients chosen so to match the ratio at $k = 0.05\, h/\text{Mpc}$ and at $k = 0.1\, h/\text{Mpc}$. As we study in Section 4.3.3, obtaining a good bias function at these scales allows for a very good extraction of the BAO oscillation pattern.

Appendix F

Covariance matrix of the Power Spectrum from N-body simulations in the Angulo-Pontzen method.

In the analyses presented in this paper, we ignore the off-diagonal components of the covariance matrix for the PS, while the diagonal part is estimated from the scatter of $|\delta_{\vec{k}}|^2$ for $\vec{k}$'s in each of the k bins. In this appendix we discuss the covariance matrix for the PS obtained in the Angulo-Pontzen method [80] and compute the effects of its nondiagonal entries using PT and with a new set of simulations.
We start from the definition of covariance matrix for the PS. Given a realization, we can define a PS estimator in the momentum bin k_m as [82] (note that our $(2\pi)^3$ convention is different from that paper)

$$\hat{P}_m = \frac{1}{V}\int_{k_m} \frac{d^3k}{V_s(k_m)}\delta_{\mathbf{k}}\delta_{-\mathbf{k}}\,, \tag{F.1}$$

where the integral is made over a momentum shell centered at k_m, $V_s(k_m) = 4\pi k_m^2 \delta k_m$, with δk_m the width of the m'th bin, and V is the volume of the simulation/survey. Moreover, we have $(2\pi)^3\delta_D(0) = V$.
Then, by considering an ensemble of realizations, we define the covariance

matrix as

$$\begin{aligned}\mathrm{cov}^P_{mn} &= \langle \hat{P}_m \hat{P}_n \rangle - \langle \hat{P}_m \rangle \langle \hat{P}_n \rangle \\ &= \frac{(2\pi)^3}{V}\left[\frac{2P_m^2}{V_s(k_m)}\delta_{mn} + \frac{1}{(2\pi)^3}\bar{T}_{mn}\right], \\ &= \langle \delta P_m \, \delta P_n \rangle \,, \end{aligned} \tag{F.2}$$

where $P_m = \langle \hat{P}_m \rangle$ is the average of the PS among the realizations and $\bar{T}_{mn}$ is the bin-averaged trispectrum

$$\begin{aligned}\bar{T}_{mn} &\equiv \int_{k_m} \frac{d^3k}{V_s(k_m)} \int_{k_n} \frac{d^3k'}{V_s(k_n)} T(\mathbf{k}, -\mathbf{k}, \mathbf{k}', -\mathbf{k}') \,, \\ &= \frac{1}{2}\frac{1}{k_m^2 k_n^2 \delta k_m \delta k_n} \int_{k_m}^{k_m+\delta k_m} k^2 dk \int_{k_n}^{k_n+\delta k_n} k'^2 dk' \int_{-1}^{1} d\cos\theta \, \tilde{T}(k, k', \cos\theta) \,, \end{aligned} \tag{F.3}$$

where in the last line we have used rotational invariance. At the third line of (F.2) we have defined $\delta P_m = \hat{P}_m - P_m$.
In the Angulo-Pontzen method [80], hereafter "AP method", the linear density field (the initial condition for the simulation) is not sampled from a gaussian distribution but is set as follows,

$$\delta^{(0)}_{\mathbf{k}} = \sqrt{V P^0(k)}\, e^{i\theta_{\mathbf{k}}} \,, \tag{F.4}$$

where $\theta_{\mathbf{k}} = -\theta_{-\mathbf{k}}$ is drawn with uniform probability between 0 and 2π[1]. The ensemble expectation values of the linear fields in the AP distribution are

[1]The PDF leading to (F.4) is $\mathcal{P}_{AP}(|\delta^{(0)}_{\mathbf{k}}|, \theta_{\mathbf{k}}) = (2\pi)^{-1}\delta_D\left(|\delta^{(0)}_{\mathbf{k}}| - \sqrt{VP^0(k)}\right)$, while for the gaussian distribution it is $\mathcal{P}_{Gauss}(|\delta^{(0)}_{\mathbf{k}}|, \theta_{\mathbf{k}}) = |\delta^{(0)}_{\mathbf{k}}|/(\pi V P^0(k)) \exp\left(-|\delta^{(0)}_{\mathbf{k}}|^2/VP^0(k)\right)$

zero for any product of odd fields, while for the even ones we have

$$
\begin{aligned}
&\langle \delta^{(0)}_{\mathbf{k}} \delta^{(0)}_{\mathbf{k}'} \rangle_{AP} = V \sqrt{P^0(k)\, P^0(k')}\, \langle e^{i(\theta_{\mathbf{k}}+\theta_{\mathbf{k}'})} \rangle_{AP} = (2\pi)^3\, P^0(k) \delta_{\mathbf{k},-\mathbf{k}'}\,, \\
&\langle \delta^{(0)}_{\mathbf{k}} \delta^{(0)}_{\mathbf{k}'} \delta^{(0)}_{\mathbf{k}''} \delta^{(0)}_{\mathbf{k}'''} \rangle_{AP} \\
&= V^2 \sqrt{P^0(k)\, P^0(k')\, P^0(k'')\, P^0(k''')}\, \langle e^{i(\theta_{\mathbf{k}}+\theta_{\mathbf{k}'}+\theta_{\mathbf{k}''}+\theta_{\mathbf{k}'''})} \rangle_{AP}\,, \\
&= (2\pi)^6 \Bigg(\delta_{\mathbf{k},-\mathbf{k}'} \delta_{\mathbf{k}'',-\mathbf{k}'''} P^0(k) P^0(k'') + \delta_{\mathbf{k},-\mathbf{k}''} \delta_{\mathbf{k}',-\mathbf{k}'''} P^0(k) P^0(k') \\
&\qquad\qquad + \delta_{\mathbf{k},-\mathbf{k}'''} \delta_{\mathbf{k}',-\mathbf{k}''} P^0(k) P^0(k') \Bigg) \\
&- \frac{(2\pi)^9}{V} (P^0(k))^2 \Bigg(\delta_{\mathbf{k},\mathbf{k}'} \delta_{\mathbf{k},-\mathbf{k}''} \delta_{\mathbf{k},-\mathbf{k}'''} + \delta_{\mathbf{k},\mathbf{k}''} \delta_{\mathbf{k},-\mathbf{k}'} \delta_{\mathbf{k},-\mathbf{k}'''} + \delta_{\mathbf{k},\mathbf{k}'''} \delta_{\mathbf{k},-\mathbf{k}'} \delta_{\mathbf{k},-\mathbf{k}''} \Bigg)\,, \\
&\dots
\end{aligned}
\tag{F.5}
$$

While the two-point correlator is the same as for the gaussian distribution, for the four-point one the AP distribution gives the extra contribution at the last line, which represents the violaton of Wick's theorem due to the non-gaussianity of the AP PDF (notice that our results differs by a factor 2 with respect to eq. (10) in [80]).
This contribution is exactly what sets to zero the $O((P^0(k))^2)$ contributions to the covariance of the PS,

$$
\begin{aligned}
&\mathrm{cov}^P_{AP,mn} = \langle \hat{P}_m \hat{P}_n \rangle_{AP} - \langle \hat{P}_m \rangle_{AP} \langle \hat{P}_n \rangle_{AP} \\
&\frac{1}{V} \int_{k_m} \frac{d^3k}{V_s(k_m)} \frac{1}{V} \int_{k_n} \frac{d^3k'}{V_s(k_n)} \Bigg(\langle \delta_{\mathbf{k}} \delta_{-\mathbf{k}} \delta_{\mathbf{k}'} \delta_{-\mathbf{k}'} \rangle_{AP} - \langle \delta_{\mathbf{k}} \delta_{-\mathbf{k}} \rangle_{AP} \langle \delta_{\mathbf{k}'} \delta_{-\mathbf{k}'} \rangle_{AP} \Bigg) \\
&\frac{1}{V} \int_{k_m} \frac{d^3k}{V_s(k_m)} \frac{1}{V} \int_{k_n} \frac{d^3k'}{V_s(k_n)} V^2 \Bigg(P^0(k) P^0(k') - P^0(k) P^0(k') \Bigg) + O((P^0(k))^3)\,, \\
&= O((P^0(k))^3)\,.
\end{aligned}
\tag{F.6}
$$

Using the compact formalism for the vertices and fields (that is $\delta_k = e^{\eta} \varphi_{1,\mathbf{k}}$, $-\theta/\mathcal{H}f = e^{\eta} \varphi_{2,\mathbf{k}}$, with $\eta = \log D_+$), we rewrite (F.6) as

$$
\begin{aligned}
\mathrm{cov}^P_{AP,mn} \;=\; & \frac{e^{4\eta}}{V^2} \int_{k_m} \frac{d^3k}{V_s(k_m)} \int_{k_n} \frac{d^3k}{V_s(k_n)} \Bigg(\langle \varphi_{1,\mathbf{k}} \varphi_{1,-\mathbf{k}} \varphi_{1,\mathbf{k}'} \varphi_{1,-\mathbf{k}'} \rangle_{AP} \\
& - \langle \varphi_{1,\mathbf{k}} \varphi_{1,-\mathbf{k}} \rangle_{AP} \langle \varphi_{1,\mathbf{k}'} \varphi_{1,-\mathbf{k}'} \rangle_{AP} \Bigg)\,.
\end{aligned}
\tag{F.7}
$$

As we have seen, the quantity inside parentheses vanishes at lowest PT order ($O((P^0)^2)$), At $O((P^0)^3)$, the first term in parentheses has the following contributions

$$\langle\varphi_{1,\mathbf{k}}\varphi_{1,-\mathbf{k}}\varphi_{1,\mathbf{k}'}\varphi_{1,-\mathbf{k}'}\rangle_{AP} \to \langle 1100\rangle_{AP} + \langle 1010\rangle_{AP} + \langle 1001\rangle_{AP} + \langle 0110\rangle_{AP} + \langle 0101\rangle_{AP} + \langle 0011\rangle_{AP} + \langle 2000\rangle_{AP} + \langle 0200\rangle_{AP} + \langle 0020\rangle_{AP} + \langle 0002\rangle_{AP} \quad \text{(F.8)}$$

where the "1" and the "2" stand for

$$\begin{aligned} &\text{"1"} \to \varphi^{(1)}_{a,\mathbf{k}} = e^{\eta} g^{(1)}_{ab} I_{\mathbf{k},\mathbf{q}_1,\mathbf{q}_2} \gamma_{bcd}(\mathbf{q}_1,\mathbf{q}_2) u_c u_d \varphi^{(0)}_{\mathbf{q}_1} \varphi^{(0)}_{\mathbf{q}_2}\,, \\ &\text{"2"} \to \varphi^{(2)}_{a,\mathbf{k}} = 2e^{2\eta} g^{(2)}_{ab} I_{\mathbf{k},\mathbf{q}_1,\mathbf{q}_2} \gamma_{bcd}(\mathbf{q}_1,\mathbf{q}_2) u_d \varphi^{(1)}_{c,\mathbf{q}_1} \varphi^{(0)}_{\mathbf{q}_2}\,, \end{aligned} \quad \text{(F.9)}$$

respectively, where we have set the linear field in the linear growing mode, $\varphi^{(0)}_{a,\mathbf{k}} = \varphi^{(0)}_{\mathbf{k}} u_a$ (with $u_1 = u_2 = 1$), and

$$g^{(n)}_{ab} = \frac{1}{n}\begin{pmatrix} 3/5 & 2/5 \\ 3/5 & 2/5 \end{pmatrix} + \frac{2}{5+2n}\begin{pmatrix} 2/5 & -2/5 \\ -3/5 & 3/5 \end{pmatrix}. \quad \text{(F.10)}$$

The subtracted part contributes with

$$\langle\varphi_{1,\mathbf{k}}\varphi_{1,-\mathbf{k}}\rangle_{AP}\langle\varphi_{1,\mathbf{k}'}\varphi_{1,-\mathbf{k}'}\rangle_{AP} \to \langle 11\rangle_{AP}\langle 00\rangle_{AP} + \langle 00\rangle_{AP}\langle 11\rangle_{AP} + 2\langle 20\rangle_{AP}\langle 00\rangle_{AP} + 2\langle 00\rangle_{AP}\langle 20\rangle_{AP}\,. \quad \text{(F.11)}$$

Now, taking into account that for "AP'' expectation values (differently from gaussian ones) the following relations hold

$$\begin{aligned} &\langle 1100\rangle_{AP} = \langle 11\rangle_{AP}\langle 00\rangle_{AP}\,, \qquad \langle 0011\rangle_{AP} = \langle 00\rangle_{AP}\langle 11\rangle_{AP} \\ &\langle 2000\rangle_{AP} = \langle 0200\rangle_{AP} = \langle 20\rangle_{AP}\langle 00\rangle_{AP}\,, \end{aligned} \quad \text{(F.12)}$$

whe have that the surviving contributions are

$$\begin{aligned} &\Big(\langle\varphi_{1,\mathbf{k}}\varphi_{1,-\mathbf{k}}\varphi_{1,\mathbf{k}'}\varphi_{1,-\mathbf{k}'}\rangle_{AP} - \langle\varphi_{1,\mathbf{k}}\varphi_{1,-\mathbf{k}}\rangle_{AP}\langle\varphi_{1,\mathbf{k}'}\varphi_{1,-\mathbf{k}'}\rangle_{AP}\Big) = \\ &\langle 1010\rangle_{AP} + \langle 1001\rangle_{AP} + \langle 0110\rangle_{AP} + \langle 0101\rangle_{AP} + O((P^0)^4) \\ &= \langle\varphi^{(1)}_{1,\mathbf{k}}\varphi^{(0)}_{1,-\mathbf{k}}\varphi^{(1)}_{1,\mathbf{k}'}\varphi^{(0)}_{1,-\mathbf{k}'}\rangle_{AP} + \langle\varphi^{(1)}_{1,\mathbf{k}}\varphi^{(0)}_{1,-\mathbf{k}}\varphi^{(0)}_{1,\mathbf{k}'}\varphi^{(1)}_{1,-\mathbf{k}'}\rangle_{AP} \\ &+ \langle\varphi^{(0)}_{1,\mathbf{k}}\varphi^{(1)}_{1,-\mathbf{k}}\varphi^{(1)}_{1,\mathbf{k}'}\varphi^{(0)}_{1,-\mathbf{k}'}\rangle_{AP} + \langle\varphi^{(0)}_{1,\mathbf{k}}\varphi^{(1)}_{1,-\mathbf{k}}\varphi^{(0)}_{1,\mathbf{k}'}\varphi^{(1)}_{1,-\mathbf{k}'}\rangle_{AP} + O((P^0)^4)\,. \end{aligned} \quad \text{(F.13)}$$

The non-vanishing contributions to the first term are given explicitly by

$$
\begin{aligned}
&\langle\varphi^{(1)}_{1,\mathbf{k}}\varphi^{(0)}_{1,-\mathbf{k}}\varphi^{(1)}_{1,\mathbf{k}'}\varphi^{(0)}_{1,-\mathbf{k}'}\rangle_{AP} = e^{2\eta}g^{(1)}_{1a}g^{(1)}_{1b}I_{\mathbf{k},\mathbf{q}_1,\mathbf{q}_2}I_{\mathbf{k}',\mathbf{p}_1,\mathbf{p}_2}\tilde{\gamma}_a(\mathbf{q}_1,\mathbf{q}_2)\tilde{\gamma}_b(\mathbf{p}_1,\mathbf{p}_2)\\
&\qquad\qquad\times\langle\varphi^{(0)}_{\mathbf{q}_1}\varphi^{(0)}_{\mathbf{q}_2}\varphi^{(0)}_{-\mathbf{k}}\varphi^{(0)}_{\mathbf{p}_1}\varphi^{(0)}_{\mathbf{p}_2}\varphi^{(0)}_{-\mathbf{k}'}\rangle_{AP}\,,\\
&= e^{2\eta}(2\pi)^3 g^{(1)}_{1a}g^{(1)}_{1b}\int d^3q_1 d^3q_2 d^3p_1 d^3p_2\;\tilde{\gamma}_a(\mathbf{q}_1,\mathbf{q}_2)\tilde{\gamma}_b(\mathbf{p}_1,\mathbf{p}_2)P^0(k)P^0(q_1)P^0(q_2)\\
&\qquad\qquad\times\delta_D(\mathbf{k}-\mathbf{q}_1-\mathbf{q}_2)\,\delta_D(\mathbf{k}'-\mathbf{p}_1-\mathbf{p}_2)\\
&\times\Bigg\{\delta_D(\mathbf{k}+\mathbf{k}')\Big[\delta_D(\mathbf{q}_1+\mathbf{p}_1)\delta_D(\mathbf{q}_2+\mathbf{p}_2)+\delta_D(\mathbf{q}_1+\mathbf{p}_2)\delta_D(\mathbf{q}_2+\mathbf{p}_1)\\
&-\frac{(2\pi)^3}{V}\delta_D(\mathbf{q}_1+\mathbf{p}_1)\delta_D(\mathbf{q}_2+\mathbf{p}_2)\delta_D(\mathbf{q}_1-\mathbf{q}_2)\Big]\\
&+\delta_D(\mathbf{q}_1-\mathbf{k}')\Big[\delta_D(\mathbf{q}_2+\mathbf{p}_1)\delta_D(-\mathbf{k}+\mathbf{p}_2)+\delta_D(\mathbf{q}_2+\mathbf{p}_2)\delta_D(-\mathbf{k}+\mathbf{p}_1)\Big]\\
&+\delta_D(\mathbf{q}_2-\mathbf{k}')\Big[\delta_D(\mathbf{q}_1+\mathbf{p}_1)\delta_D(-\mathbf{k}+\mathbf{p}_2)+\delta_D(\mathbf{q}_1+\mathbf{p}_2)\delta_D(-\mathbf{k}+\mathbf{p}_1)\Big]\Bigg\}\,,
\end{aligned}
\tag{F.14}
$$

where the subtracted term at the second line of the last equation comes from the difference between the "AP" averaging and the gaussian one, see eq. (F.5), and we have defined $\tilde{\gamma}_a(\mathbf{q}_1,\mathbf{q}_2)\equiv\gamma_{abc}(\mathbf{q}_1,\mathbf{q}_2)u_a u_b$. Working out the delta functions and using $(2\pi)^3\delta_D(0)=V$ we get

$$
\begin{aligned}
&\langle\varphi^{(1)}_{\mathbf{k}}\varphi^{(0)}_{-\mathbf{k}}\varphi^{(1)}_{\mathbf{k}'}\varphi^{(0)}_{-\mathbf{k}'}\rangle_{AP} =\\
&\quad(2\pi)^3 e^{-4\eta}\delta_D(\mathbf{k}+\mathbf{k}')\left[VP^0(k)\Delta P_{22}(k)-4P^0(k)(P^0(k/2))^2\right]\\
&\quad+4e^{-4\eta}VF_2(\mathbf{k}',\mathbf{k}-\mathbf{k}')F_2(\mathbf{k},\mathbf{k}'-\mathbf{k})P^0(k)P^0(k')P^0(|\mathbf{k}-\mathbf{k}'|)\,,
\end{aligned}
\tag{F.15}
$$

where we have used $F_2(\mathbf{k}',\mathbf{k}-\mathbf{k}')=g^{(1)}_{1a}\tilde{\gamma}_a(\mathbf{k}',\mathbf{k}-\mathbf{k}')$, and $\Delta P_{22}(k)$ is the "22" contribution to the 1-loop PS [55].
Summing up the four contributions we finally have

$$
\begin{aligned}
&\mathrm{cov}^P_{AP,mn} =\\
&\quad\frac{(2\pi)^3}{V}\left[\left(4\frac{P^0(k)\Delta P_{22}(k)}{V_s(k_m)}-16\frac{P^0(k)(P^0(k/2))^2}{V\,V_s(k_m)}\right)\delta_{mn}+\frac{1}{(2\pi)^3}T^{AP}_{mn}\right],
\end{aligned}
\tag{F.16}
$$

where

$$T^{AP}_{mn} \equiv 8 \int_{k_m} \frac{d^3k}{V_s(k_m)} \int_{k_n} \frac{d^3k'}{V_s(k_n)} \Bigg(F_2(\mathbf{k}', \mathbf{k}-\mathbf{k}') F_2(\mathbf{k}, \mathbf{k}'-\mathbf{k}) \times P^0(k) P^0(k') P^0(|\mathbf{k}-\mathbf{k}'|) + (\mathbf{k}' \to -\mathbf{k}') \Bigg) . \tag{F.17}$$

As we see, the diagonal contribution to the covariance matrix is only $O((P^0)^3)$ and is therefore suppressed with respect to that obtained in the standard method with gaussian initial conditions.

This is shown explicitely in Fig. F.1, where we see that our analytic computation reproduces, at small $k's$, the result of the measurement of the covariance matrix from the scattering of $|\delta_{\vec{k}}|^2$ for $\vec{k}$'s in each of the k bins.

We also plot the results obtained via N-body simulations by performing 100 AP pairs (i.e., 200 simulations) with the same simulation parameters except a much smaller number of particles 256^3. We analyse the simulated data only at $z = 0$ for the matter field. These simulations allow us to estimate the covariance matrix including the non-diagonal entries both for the paired and unpaired cases. While the resolution is much poorer and the number of realizations might be small for the estimation of the covariance matrix, this new set of simulations would be helpful to check the expectations from the analytical argument at least qualitatively. In Fig. F.1 we confirm the suppression of the variance for the AP simulations on large scales compared with that from Gaussian initial conditions. The fixed-and-paired method is especially efficient to reduce the variance on scales $k \lesssim 0.1\, h\mathrm{Mpc}^{-1}$. On smaller scales, this approaches to the half of the fixed case. This shows that the cancellation is no longer effective, and the variance is reduced simply because we have doubled the number of Fourier mode by using two simulations. The covariance eventually exceeds the Gaussian value on smaller scales, where we see that the paring no longer helps. We also see that the analytic result compares rather well with the numerical one for the fixed method for $k \lesssim 0.1\ \mathrm{h\,Mpc}^{-1}$.

In Fig. F.2 we show the full covariance matrix as measured in simulations, the non-diagonal entries $\mathrm{cov}(k, k')$ for some fixed value of one of the two momenta, and the cross-correlation coefficient, $\mathrm{cov}(k, k')/\sqrt{\mathrm{cov}(k, k)\,\mathrm{cov}(k', k')}$, to see the relative importance of the off-diagonal entries. The general trend

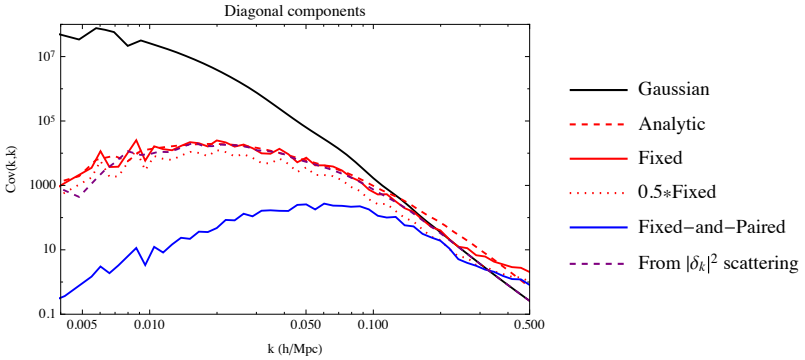

Figure F.1: The diagonal entries of the PS covariance matrix as obtained in the standard method with gaussian initial conditions (black solid) and in the AP method, as measured from N-body simulations in the "Fixed" approach (red-solid) and in the "Fixed-and-Paired" one (blue solid). We also show the estimate from the scattering of $|\delta_{\vec{k}}|^2$ for $\vec{k}$'s in each of the k bins (purple-dashed) and from the analytic result of eq. (F.16) (red-dashed).

looks very similar in the two cases, and we confirm that the numerical and the analytical results agree at large scales.

Finally, we added the non-diagonal entries of the PS covariance matrix in the covariance matrix for the extractor, eq. (4.7), to see their impact on our χ^2 analyses. This is shown in Fig. F.3, where we show, by comparison, the effect of including these terms when fitting the TRG PS to the one extracted from the simulations for DM at $z = 0$. As anticipated, the effect of the non-diagonal terms is to all extents negligible, and therefore we only considered the diagonal covariance matrix for the PS in the paper. Notice that, coherently with what we have done in the rest of the paper, we have used the non-diagonal entries of the PS covariance matrix for the "fixed" method (both in the analytical and in the numerical determinations), which as seen in Figs. F.1, F.2, gives a conservative estimate of the covariance of our AP simulations obtained with the fixed-and-paired method.

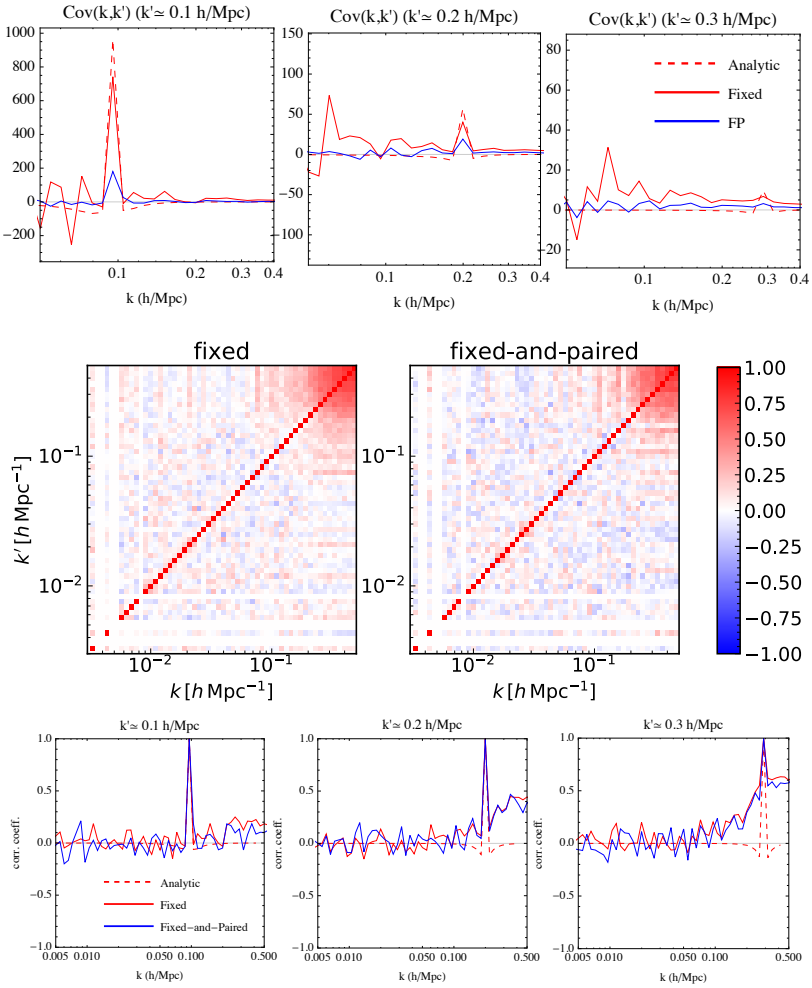

Figure F.2: Estimated covariance matrix $\mathrm{cov}^P_{AP}(k,k')$ for some fixed values of k' (upper panel), the matrix of correlation coefficients, $R(k,k') = \mathrm{cov}^P_{AP}(k,k')/\sqrt{\mathrm{cov}^P_{AP}(k,k)\mathrm{cov}^P_{AP}(k',k')}$ (central panel) and the same quantity as a function of k for some fixed values of k' (lower panel).

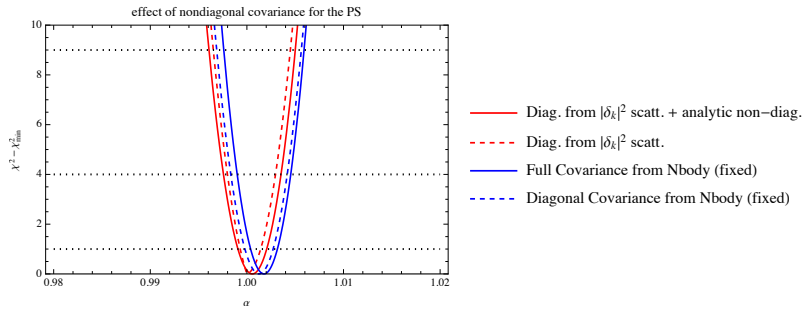

Figure F.3: The effect of the non-diagonal entries of the covariance matrix for the PS on the fitting procedures discussed in the paper. We compare the extractors from N-Body simulations and from the TRG for DM at $z = 0$. To compute the red lines we estimated, as in the rest of the paper, the diagonal entries of the PS covariance matrix from the scattering of $|\delta_{\vec{k}}|^2$ inside each momentum bin. In the continuous red line we added the effect of non-diagonal entries computed analytically using eq. (F.16). The blue lines are derived using the PS covariance measured from simulations.

Bibliography

[1] **Planck** Collaboration, Y. Akrami et. al., *Planck 2018 results. I. Overview and the cosmological legacy of Planck*, 1807.06205.

[2] **EUCLID** Collaboration, R. Laureijs et. al., *Euclid Definition Study Report*, 1110.3193.

[3] **Planck** Collaboration, N. Aghanim et. al., *Planck 2018 results. VI. Cosmological parameters*, 1807.06209.

[4] **Particle Data Group** Collaboration, M. Tanabashi et. al., *Review of Particle Physics*, Phys. Rev. **D98** (2018), no. 3 030001.

[5] M. Chevallier and D. Polarski, *Accelerating universes with scaling dark matter*, Int. J. Mod. Phys. **D10** (2001) 213–224 [gr-qc/0009008].

[6] E. V. Linder, *Exploring the expansion history of the universe*, Phys. Rev. Lett. **90** (2003) 091301 [astro-ph/0208512].

[7] M. Park, K. M. Zurek and S. Watson, *A Unified Approach to Cosmic Acceleration*, Phys. Rev. **D81** (2010) 124008 [1003.1722].

[8] G. Gubitosi, F. Piazza and F. Vernizzi, *The Effective Field Theory of Dark Energy*, JCAP **1302** (2013) 032 [1210.0201]. [JCAP1302,032(2013)].

[9] J. K. Bloomfield, . . Flanagan, M. Park and S. Watson, *Dark energy or modified gravity? An effective field theory approach*, JCAP **1308** (2013) 010 [1211.7054].

[10] P. Creminelli, G. D'Amico, J. Norena and F. Vernizzi, *The Effective Theory of Quintessence: the w¡-1 Side Unveiled*, JCAP **0902** (2009) 018 [0811.0827].

[11] **Supernova Cosmology Project** Collaboration, S. Perlmutter et. al., *Measurements of the cosmological parameters Omega and Lambda from the first 7 supernovae at z¿=0.35*, Astrophys. J. **483** (1997) 565 [astro-ph/9608192].

[12] **Supernova Search Team** Collaboration, B. P. Schmidt et. al., *The High Z supernova search: Measuring cosmic deceleration and global curvature of the universe using type Ia supernovae*, Astrophys. J. **507** (1998) 46–63 [astro-ph/9805200].

[13] **Supernova Cosmology Project** Collaboration, S. Perlmutter et. al., *Discovery of a supernova explosion at half the age of the Universe and its cosmological implications*, Nature **391** (1998) 51–54 [astro-ph/9712212].

[14] **Supernova Search Team** Collaboration, A. G. Riess et. al., *Observational evidence from supernovae for an accelerating universe and a cosmological constant*, Astron. J. **116** (1998) 1009–1038 [astro-ph/9805201].

[15] **Supernova Cosmology Project** Collaboration, S. Perlmutter et. al., *Measurements of Omega and Lambda from 42 high redshift supernovae*, Astrophys. J. **517** (1999) 565–586 [astro-ph/9812133].

[16] D. J. Eisenstein, W. Hu and M. Tegmark, *Cosmic complementarity: H(0) and Omega(m) from combining CMB experiments and redshift surveys*, Astrophys. J. **504** (1998) L57–L61 [astro-ph/9805239].

[17] C. Blake and K. Glazebrook, *Probing dark energy using baryonic oscillations in the galaxy power spectrum as a cosmological ruler*, Astrophys. J. **594** (2003) 665–673 [astro-ph/0301632].

[18] H.-J. Seo and D. J. Eisenstein, *Probing dark energy with baryonic acoustic oscillations from future large galaxy redshift surveys*, Astrophys. J. **598** (2003) 720–740 [astro-ph/0307460].

[19] H.-J. Seo and D. J. Eisenstein, *Improved forecasts for the baryon acoustic oscillations and cosmological distance scale*, astro-ph/0701079.

[20] **BOSS** Collaboration, S. Alam et. al., *The clustering of galaxies in the completed SDSS-III Baryon Oscillation Spectroscopic Survey: cosmological analysis of the DR12 galaxy sample*, Mon. Not. Roy. Astron. Soc. **470** (2017), no. 3 2617–2652 [1607.03155].

[21] F. Bernardeau, S. Colombi, E. Gaztanaga and R. Scoccimarro, *Large scale structure of the universe and cosmological perturbation theory*, Phys. Rept. **367** (2002) 1–248 [astro-ph/0112551].

[22] D. Blas, M. Garny and T. Konstandin, *Cosmological perturbation theory at three-loop order*, JCAP **1401** (2014), no. 01 010 [1309.3308].

[23] T. Nishimichi, F. Bernardeau and A. Taruya, *Response function of the large-scale structure of the universe to the small scale inhomogeneities*, Phys. Lett. **B762** (2016) 247–252 [1411.2970].

[24] D. J. Eisenstein, H.-j. Seo, E. Sirko and D. Spergel, *Improving Cosmological Distance Measurements by Reconstruction of the Baryon Acoustic Peak*, Astrophys.J. **664** (2007) 675–679 [astro-ph/0604362].

[25] D. J. Eisenstein, H.-j. Seo and . White, Martin J., *On the Robustness of the Acoustic Scale in the Low-Redshift Clustering of Matter*, Astrophys.J. **664** (2007) 660–674 [astro-ph/0604361].

[26] M. Crocce and R. Scoccimarro, *Renormalized cosmological perturbation theory*, Phys. Rev. **D73** (2006) 063519 [astro-ph/0509418].

[27] M. Crocce and R. Scoccimarro, *Memory of initial conditions in gravitational clustering*, Phys. Rev. **D73** (2006) 063520 [astro-ph/0509419].

[28] R. Scoccimarro and J. Frieman, *Loop corrections in nonlinear cosmological perturbation theory*, Astrophys.J.Suppl. **105** (1996) 37 [astro-ph/9509047].

[29] B. Jain and E. Bertschinger, *Selfsimilar evolution of cosmological density fluctuations*, Astrophys.J. **456** (1996) 43 [astro-ph/9503025].

[30] M. Peloso and M. Pietroni, *Galilean invariant resummation schemes of cosmological perturbations*, JCAP **1701** (2017), no. 01 056 [1609.06624].

[31] L. Senatore and M. Zaldarriaga, *The IR-resummed Effective Field Theory of Large Scale Structures*, JCAP **1502** (2015), no. 02 013 [1404.5954].

[32] T. Baldauf, M. Mirbabayi, M. Simonović and M. Zaldarriaga, *Equivalence Principle and the Baryon Acoustic Peak*, Phys. Rev. **D92** (2015), no. 4 043514 [1504.04366].

[33] D. Blas, M. Garny, M. M. Ivanov and S. Sibiryakov, *Time-Sliced Perturbation Theory II: Baryon Acoustic Oscillations and Infrared Resummation*, JCAP **1607** (2016), no. 07 028 [1605.02149].

[34] A. Kehagias and A. Riotto, *Symmetries and Consistency Relations in the Large Scale Structure of the Universe*, Nucl.Phys. **B873** (2013) 514–529 [1302.0130].

[35] M. Peloso and M. Pietroni, *Galilean invariance and the consistency relation for the nonlinear squeezed bispectrum of large scale structure*, JCAP **1305** (2013) 031 [1302.0223].

[36] D. Baumann, A. Nicolis, L. Senatore and M. Zaldarriaga, *Cosmological Non-Linearities as an Effective Fluid*, JCAP **1207** (2012) 051 [1004.2488].

[37] J. J. M. Carrasco, M. P. Hertzberg and L. Senatore, *The Effective Field Theory of Cosmological Large Scale Structures*, JHEP **1209** (2012) 082 [1206.2926].

[38] S. Floerchinger, M. Garny, N. Tetradis and U. A. Wiedemann, *Renormalization-group flow of the effective action of cosmological large-scale structures*, JCAP **1701** (2017), no. 01 048 [1607.03453].

[39] M. Pietroni, G. Mangano, N. Saviano and M. Viel, *Coarse-Grained Cosmological Perturbation Theory*, JCAP **1201** (2012) 019 [1108.5203].

[40] A. Manzotti, M. Peloso, M. Pietroni, M. Viel and F. Villaescusa-Navarro, *A coarse grained perturbation theory for the Large Scale Structure, with cosmology and time independence in the UV*, JCAP **1409** (2014), no. 09 047 [1407.1342].

[41] M. Pietroni, *Flowing with Time: a New Approach to Nonlinear Cosmological Perturbations*, JCAP **0810** (2008) 036 [0806.0971].

[42] M. Peloso and M. Pietroni, *Ward identities and consistency relations for the large scale structure with multiple species*, JCAP **1404** (2014) 011 [1310.7915].

[43] S. Pueblas and R. Scoccimarro, *Generation of Vorticity and Velocity Dispersion by Orbit Crossing*, Phys. Rev. **D80** (2009) 043504 [0809.4606].

[44] V. Springel, *The Cosmological simulation code GADGET-2*, Mon.Not.Roy.Astron.Soc. **364** (2005) 1105–1134 [astro-ph/0505010].

[45] K. Heitmann, E. Lawrence, J. Kwan, S. Habib and D. Higdon, *The Coyote Universe Extended: Precision Emulation of the Matter Power Spectrum*, Astrophys.J. **780** (2014) 111 [1304.7849].

[46] M. Peloso, M. Pietroni, M. Viel and F. Villaescusa-Navarro, *The effect of massive neutrinos on the BAO peak*, JCAP **1507** (2015), no. 07 001 [1505.07477].

[47] **WMAP** Collaboration, E. Komatsu et. al., *Five-Year Wilkinson Microwave Anisotropy Probe (WMAP) Observations: Cosmological Interpretation*, Astrophys. J. Suppl. **180** (2009) 330–376 [0803.0547].

[48] M. Sato and T. Matsubara, *Nonlinear Biasing and Redshift-Space Distortions in Lagrangian Resummation Theory and N-body Simulations*, Phys.Rev. **D84** (2011) 043501 [1105.5007].

[49] **BOSS** Collaboration, L. Anderson et. al., *The clustering of galaxies in the SDSS-III Baryon Oscillation Spectroscopic Survey: baryon acoustic oscillations in the Data Releases 10 and 11 Galaxy samples*, Mon.Not.Roy.Astron.Soc. **441** (2014), no. 1 24–62 [1312.4877].

[50] Y. Noh, M. White and N. Padmanabhan, *Reconstructing baryon oscillations*, Phys.Rev. **D80** (2009) 123501 [0909.1802].

[51] S. Tassev and M. Zaldarriaga, *Towards an Optimal Reconstruction of Baryon Oscillations*, JCAP **1210** (2012) 006 [1203.6066].

[52] M. White, *Reconstruction within the Zeldovich approximation*, Mon. Not. Roy. Astron. Soc. **450** (2015), no. 4 3822–3828 [1504.03677].

[53] E. Noda, M. Peloso and M. Pietroni, *A Robust BAO Extractor*, JCAP **1708** (2017), no. 08 007 [1705.01475].

[54] B. D. Sherwin and M. Zaldarriaga, *The Shift of the Baryon Acoustic Oscillation Scale: A Simple Physical Picture*, Phys.Rev. **D85** (2012) 103523 [1202.3998].

[55] F. Bernardeau, S. Colombi, E. Gaztanaga and R. Scoccimarro, *Large-scale structure of the universe and cosmological perturbation theory*, Phys. Rept. **367** (2002) 1–248 [astro-ph/0112551].

[56] V. Desjacques, *Baryon acoustic signature in the clustering of density maxima*, Phys.Rev. **D78** (2008) 103503 [0806.0007].

[57] V. Desjacques and R. K. Sheth, *Redshift space correlations and scale-dependent stochastic biasing of density peaks*, Phys.Rev. **D81** (2010) 023526 [0909.4544].

[58] T. Baldauf, V. Desjacques and U. Seljak, *Velocity bias in the distribution of dark matter halos*, 1405.5885.

[59] R. Scoccimarro, *Redshift-space distortions, pairwise velocities and nonlinearities*, Phys.Rev. **D70** (2004) 083007 [astro-ph/0407214].

[60] D. J. Eisenstein and W. Hu, *Baryonic Features in the Matter Transfer Function*, Astrophys. J. **496** (1998) 605 [astro-ph/9709112].

[61] N. Padmanabhan, M. White and J. Cohn, *Reconstructing Baryon Oscillations: A Lagrangian Theory Perspective*, Phys.Rev. **D79** (2009) 063523 [0812.2905].

[62] T. Nishimichi, H. Ohmuro, M. Nakamichi, A. Taruya, K. Yahata, A. Shirata, S. Saito, H. Nomura, K. Yamamoto and Y. Suto, *Characteristic Scales of Baryon Acoustic Oscillations from Perturbation Theory: Non-linearity and Redshift-Space Distortion Effects*, Publ. Astron. Soc. Jap. **59** (2007) 1049 [0705.1589].

[63] J. Lesgourgues, S. Matarrese, M. Pietroni and A. Riotto, *Non-linear Power Spectrum including Massive Neutrinos: the Time-RG Flow Approach*, JCAP **0906** (2009) 017 [0901.4550].

[64] L. Senatore and M. Zaldarriaga, *The Effective Field Theory of Large-Scale Structure in the presence of Massive Neutrinos*, 1707.04698.

[65] A. Upadhye, *Neutrino mass and dark energy constraints from redshift-space distortions*, 1707.09354.

[66] "SDSS-III BOSS webpage." http://www.sdss3.org/index.php.

[67] F.-S. Kitaura, G. Yepes and F. Prada, *Modelling Baryon Acoustic Oscillations with Perturbation Theory and Stochastic Halo Biasing*, Mon. Not. Roy. Astron. Soc. **439** (2014) 21 [1307.3285].

[68] F.-S. Kitaura et. al., *The clustering of galaxies in the SDSS-III Baryon Oscillation Spectroscopic Survey: mock galaxy catalogues for the BOSS Final Data Release*, Mon. Not. Roy. Astron. Soc. **456** (2016), no. 4 4156–4173 [1509.06400].

[69] T. Nishimichi, E. Noda, M. Peloso and M. Pietroni, *BAO Extractor: bias and redshift space effects*, JCAP **1801** (2018), no. 01 035 [1708.00375].

[70] A. Nusser and M. Davis, *On the prediction of velocity fields from redshift space galaxy samples*, Astrophys. J. **421** (1994) L1–L4 [astro-ph/9309009].

[71] **BOSS** Collaboration, F. Beutler et. al., *The clustering of galaxies in the completed SDSS-III Baryon Oscillation Spectroscopic Survey: baryon acoustic oscillations in the Fourier space*, Mon. Not. Roy. Astron. Soc. **464** (2017), no. 3 3409–3430 [1607.03149].

[72] H.-J. Seo, F. Beutler, A. J. Ross and S. Saito, *Modeling the reconstructed BAO in Fourier space*, Mon. Not. Roy. Astron. Soc. **460** (2016), no. 3 2453–2471 [1511.00663].

[73] V. Springel, *The Cosmological simulation code GADGET-2*, Mon.Not.Roy.Astron.Soc. **364** (2005) 1105–1134 [astro-ph/0505010].

[74] **Planck** Collaboration, P. A. R. Ade et. al., *Planck 2015 results. XIII. Cosmological parameters*, Astron. Astrophys. **594** (2016) A13 [1502.01589].

[75] T. Nishimichi et. al., *Modeling Nonlinear Evolution of Baryon Acoustic Oscillations: Convergence Regime of N-body Simulations and Analytic Models*, Publ. Astron. Soc. Jap. **61** (2009) 321 [0810.0813].

[76] P. Valageas and T. Nishimichi, *Combining perturbation theories with halo models*, 1009.0597.

[77] R. Scoccimarro, *Transients from initial conditions: a perturbative analysis*, Mon. Not. Roy. Astron. Soc. **299** (1998) 1097 [astro-ph/9711187].

[78] M. Crocce, S. Pueblas and R. Scoccimarro, *Transients from Initial Conditions in Cosmological Simulations*, Mon. Not. Roy. Astron. Soc. **373** (2006) 369–381 [astro-ph/0606505].

[79] A. Taruya, F. Bernardeau, T. Nishimichi and S. Codis, *RegPT: Direct and fast calculation of regularized cosmological power spectrum at two-loop order*, Phys.Rev. **D86** (2012) 103528 [1208.1191].

[80] R. E. Angulo and A. Pontzen, *Cosmological N-body simulations with suppressed variance*, Mon. Not. Roy. Astron. Soc. **462** (2016), no. 1 L1–L5 [1603.05253].

[81] P. S. Behroozi, R. H. Wechsler and H.-Y. Wu, *The Rockstar Phase-Space Temporal Halo Finder and the Velocity Offsets of Cluster Cores*, Astrophys. J. **762** (2013) 109 [1110.4372].

[82] R. Scoccimarro, M. Zaldarriaga and L. Hui, *Power spectrum correlations induced by nonlinear clustering*, Astrophys. J. **527** (1999) 1 [astro-ph/9901099].